RICE UNIVERSITY

Millimeter Wave Transmission Spectroscopy of 2D Electron and Hole Systems

by

Kristjan Jakob Stone

A Thesis Submitted
in Partial Fulfillment of the
Requirements for the Degree

Doctor of Philosophy

Approved, Thesis Committee:

Rui-Rui Du, Chair
Professor of Physics and Astronomy

Emilia Morosan
Assistant Professor of Physics and Astronomy

Junichiro Kono
Professor of Electrical and Computer Engineering

Houston, Texas

April, 2010

To my Mother, who put up with me while I was writing this thesis.

The Appendix to Dr. Douglas Natelson, who valiantly lost his while reading the first draft.

Abstract

Millimeter Wave Transmission Spectroscopy of 2D Electron and Hole Systems

by

Kristjan Jakob Stone

In order to explore how electrons and holes in 2D semiconductors behave at ^3He temperatures under millimeter wave irradiation, we developed a new probe and measurement technique. Our samples are specially grown high-mobility $GaAs/AlGaAs$ 2D electron or hole systems that have been modulation doped with Si or C respectively and etched into Hall bars. We also use microwave irradiation waveguide techniques to probe edge magnetoplasmons in 2D electron systems and find that the periodic resistance oscillations in the magnetic field are independent of the length between the leads measured. This demonstrates that the propagation of edge states is a non-local effect, contrary to previously established research. We confirm microwave induced resistance oscillations using a newly developed probe that delivers microwaves from a frequency generator down to the sample via a coax line and coplanar waveguides. Due to the low frequency range ($2-40\,\mathrm{GHz}$) and high irradiation powers available, we are able to observe microwave induced resistance oscillations and newly revealed fractional microwave induced resistance oscillations. The probe that

we develop for this new measurement makes previously unattainable non-Faraday as well as Faraday irradiation geometries accessible. In addition to measuring quantum transport, it also allows us to measure the transmission of microwaves across the sample. We establish a differential measurement technique that instantaneously removes the background signal leaving only the transmission from the 2D system, also reducing the preparation time required. This is accomplished with a gated high-mobility sample prepared to allow for microwaves to be irradiated from the back. The advantage of this new technique is that it accommodates any gated/polished sample which can be mounted on the specially designed sample holder. From this arrangement we are able to measure the cyclotron resonance transmission minima of both the 2D electron and hole systems. We can then use the known values for the effective mass and cyclotron time constant as a confirmation that our new probe can successfully make the expected measurements.

Acknowledgments

I was accepted to Rice's Physics and Astronomy Department two weeks before classes started and arrived one week later with two bags and no place to live. Since then, I have had the wonderful fortune to establish myself at Rice University with friends and mentors who have been invaluable resources. They have made this thesis, my degree, and the wonderful years I have spent here possible.

I would very much like to thank my advisor Dr. Rui-Rui Du for his insight into what direction my projects should take and his immense patience when the results were slow in coming. His support guided my understanding and interest in low temperature condensed matter physics.

In addition to my advisor, I would like to thank my other committee members for their guidance and pushing me to strive for what initially felt unattainable. Dr. Junichiro Kono was not only on my PhD committee but also gave me the opportunity to teach in Japan for the NanoJapan program and facilitated the contacts to do research there. Dr. Emilia Morosan agreed to be on my committee at the last moment, accepting with a good grace and enthusiasm despite her busy schedule for which I will always be grateful. She has been very helpful in giving my PhD and thesis greater meaning by raising the bar to meet her standards. Dr. Douglas Natelson was initially on my committee but had to bow out due to an unexpected appendectomy. I'm pretty sure his surgery and the subsequent recovery was more painful than my defense but he still made himself available to discuss the draft of my thesis the following week.

I would like to acknowledge Dr. Chang-Li Yang, Dr. Zhuoquan Yuan, and Dr. Tauno Knuuttila whose welcome advice and patience guided me in my lab work and helped to avoid any catastrophic equipment failures. In addition, to this I would like to thank my current labmates, Yanhua Dai, Chi Zhang, Dr. Guangton Liu and especially Ivan Knez for his characterization of the Si_3N_4 processing technique.

The breakthrough that finally made this thesis possible was the result of talks with Dr. Ted Corcovilos and Tobias Paprotta (who suggested and provided the electronic relay). Without their input, this project would have never have reached a successful resolution. I would like to also like to thank Ted for his mentorship which started back when I worked with him at Caltech in the summer of 2003, in Dr. Nai-Chang Yeh's group, and Dr. Yeh herself for the opportunity to work with her then and for her support which was instrumental in my going to graduate school in this field.

The fabrication of the samples would not have been possible without the Rice Shared Equipment Authority, and specifically Patrick Johnson. The support for this thesis and research was made possible by the National Science Foundation. This research would have not been possible without the samples from Loren Pfeiffer and Ken West at Princeton University and Michael Manfra at Purdue.

The balance between research and social activities came in the form of my involvement with the Physics & Astronomy Graduate Student Association and the Rice Graduate Student Association. To all I met and worked with during my tenure with these organizations, I am hugely thankful for the opportunity you provided to

become involved with the wider community of Rice University and the time and effort you put into making these organizations the wonderful resources they are for our campus.

Dan Stark provided his assistance and the patience of a saint with the formatting of this thesis. I would like to thank my friends, specifically Katie Mayer, James Hitchcock, and the everyone at Potluck, and the many others at Rice who have made my experience in Houston one of the best times of my life. And finally, I would not be here if it was not for the support of my parents, brother, Uncle Bill, Ai Yokoyama and the many people who are my family, even if we're not related. Thank you all.

Contents

Tables

Illustrations

Chapter 1

Introduction

Microwaves have been used in low temperature systems as a way to interact with the charged carriers in two dimensional systems of electrons or holes. This has not only been confined to fundamental research interests but is a large and growing area of applied industry, especially as operating frequencies in electronic devices increase to incorporate more information. One such system of interest is the high mobility $GaAs/AlGaAs$ heterostructure, or quantum well, where microwaves are irradiated at just the right frequency to resonate with the carriers. From this interaction, transitions can be made in the energy level of electron-electron interactions, cyclotron resonance, and plasma resonance.

The goal of this thesis is to delve into these microwave interactions with ultra clean high mobility 2D electron and hole gasses, culminating in development a new way to use microwave transmission across these samples to measure cyclotron resonance. One of the many challenges was to build a quantum transport-based cryogenic probe that would be able to take these measurements, reproducibly and with little change in the sample fabrication. To accomplish this, we went through many iterations of geometries until finally finding one that accomplished our goals. We also needed to show that the new coax-based probe could irradiate a sample with microwaves and see the same microwave-induced oscillations/effects as previous waveguide based

microwave probes. From this standard we were able to move on to more complex and inovative geometries involving transmission lines which allowed us to explore cyclotron resonance absorption (a geometry based on Engel et al. [1] for use with microwave interactions and the quantum Hall effect). One of the primary complications we found related to the large transmission background signal of microwave resonances originating from microwaves coupling and resonating with any number of metallic objects in the sample space, in addition to the signal from the 2D electron or hole gas (2DEG or 2DHG). To overcome the background we developed a new gate modulation measurement technique (unknown to us at the time, a similar technique had been developed for far infrared measurements [2]). Using this technique we could effectively see the sample's cyclotron resonance. We used the cyclotron resonance peaks to determine the values for the effective masses of the system, which we were able to confirm with previous known values for 2DEG and 2DHG in $GaAs/AlGaAs$ using different techniques [3, 4, 5, 6, 7]. Along with the effective mass, we also found a proportionality for the cyclotron time constant for these systems with respect to frequency, input power, temperature, and density.

This experiment proved that this coax-based geometry was a viable way to study the microwave transmission of $GaAs/AlGaAs$ heterostructures and quantum wells, which we can apply to a variety of new samples and new geometries. It effectively moved the experiment from the optical/analog systems of the previous measurements [2, 5, 6, 8, 9, 10, 11] into a scalable digital circuit-based system with picowatt resolu-

tion and a high turnaround time. This means that we could apply this technique to new samples ranging from nanotubes and graphene to high mobility 2DEG, where we could compare the cyclotron resonance signal to the microwave induced resistance oscillations. We have created a multiuse tool for measuring the cyclotron time constant with the potential for many other applications.

In the background chapter of the thesis we will provide an overview of the two-dimensional systems that make up the electron and hole heterostructures. These systems are created from the junction between two crystal structures of $GaAs$ and $AlGaAs$ that have been grown very slowly on top of each other using molecular beam epitaxy. This process produces exceptionally clean samples that have very high carrier densities and mobilities at low temperatures when the carriers drop to the lowest z-subband. The advantage to having high mobilities is that the electrons can travel much greater distances without scattering off impurities. By placing the samples in a magnetic field, the density of states quantizes into energy levels (Landau levels) whose separation can be controlled by the magnetic field. The high quality of the 2D carriers lead to very sharp Landau levels and create the possibility of introducing outside energy to resonate with the transition from one Landau level to another. Millimeter wavelengths, depending on the frequency, correspond with the transition energy between Landau levels and can resonate with them. These microwave-induced resonance features, MIRO, were discovered in 1999 by Zudov et al. [12]. They matched the fundamental cyclotron resonance and integer ratios between the frequency of

irradiation and the cyclotron frequency. These resonances formed peaks in the longitudinal resistance and were periodic in the inverse of the magnetic field. At higher sample purities, zero resistance states develop between the MIRO peaks [13]. At higher magnetic fields then the fundamental cyclotron resonance, fractional MIRO (FMIRO) develop, provided the signal is strong enough to overcome any background Shubnikov de Haas (SdH) signal, in the longitudinal resistance. Other features that were explored using a waveguide probe to supply microwaves were the edge magnetoplasmon oscillations (EMPO). These oscillations propagate due to induced charge oscillations in the leads of the sample [14].

The next chapter explains in more detail the experimental apparatus that was created to accomplish our transmission measurements. The cryogenic ^3He system and high mobility samples that were used will also be discussed.

Following the description of the apparatus, we will explain the previously-established and new measurement techniques that were developed to use the new coaxial probe. The new technique was based on the ΔR differential technique established by M. A. Zudov [12] and adjusted to incorporate a differential measurement based on transmitted microwave power, ΔP. This new technique successfully subtracted the large background signal leaving the minute transmission signal from the 2D system. The result of which is the differential measurement correctly used to identify the cyclotron resonance peaks.

A detailed explanation of our results for each of the experiments is described in the

experimental results chapter. Our results are can be broken up into two experiments, microwave induced resistance oscillations and microwave transmission. By irradiating a sample with microwaves, we are able to explore microwave induce resistance oscillations, integer and fractional to high orders. We also observe the properties of microwave induced edge magnetoplasma oscillations (EMPO) in a 2DEG. For the second experiment, we were the first to simultaneously measure magnetotransport and microwave transmission across both 2DEG and 2DHG systems. The transmission results are able to reveal the cylotron resonant peak and from that, measure the effective mass multiplier and the cyclotron time constant.

In the conclusion, we summarize the results along with the possible directions this research can take in the future.

This research expands the possibilities for microwave irradiation of 2D systems, and confirms the results with known values derived from the cyclotron resonance. To accomplish this, a new probe and technique were developed to incorporate measuring not only the longitudinal resistance but also the microwave transmission of a 2D electron or hole sample, since previous research did not address all of these aspects simultaneously. This should provide opportunities for new research to be developed beyond these preliminary results.

Chapter 2

Background

2.1 Band Structure of GaAs

The differences between the band structures of $GaAs$ and $Al_xGa_{1-x}As$ form the basis for the 2D systems that are used for semiconductor research. The conduction and valence bands of these two crystal structures are slightly mismatched, which creates a heterojunction when they are grown on top of one another. At the heterojunction the conduction bands form a triangular well. This well provides confinement along one direction (the z-axis) and effectively creates a 2D system in the other two dimensions (x and y). Using the solution of an electron in triangular well from the Airy function for a triangular well [15] of slope F, we find

$$\varepsilon_n = \left[\frac{3\pi}{2}(n - \frac{1}{4})\right]^{\frac{2}{3}} \left[\frac{\hbar^2}{2m}(e \cdot F)^2\right]^{\frac{1}{3}} \tag{2.1}$$

where F is the electric field and n is the energy level), yielding

$$\varepsilon_1 = \left[\frac{9\pi}{8}\right]^{\frac{2}{3}} \left[\frac{\hbar^2}{2m}(e \cdot F)^2\right]^{\frac{1}{3}} \tag{2.2}$$

for the lowest energy level. To provide these wells with carriers, the $Al_xGa_{1-x}As$ structure is modulation doped with Si in the case of the 2D electron gas (2DEG).

Examples of the ratio between Al and Ga, or x is 0.3 for the HJ 2DEG (described in Section 3.2).

The length scale we are dealing with in these system without a magnetic field is based on the effective Bohr radius

$$a_o^* \equiv \frac{4\pi\kappa\epsilon_o\hbar^2}{m^* e^2} = 9.9\,\mathrm{nm} \tag{2.3}$$

where κ is the relative dielectric constant for $GaAs$, ϵ_o is the permittivity of free space, $\hbar$ is Planck's constant divided by 2π, m^* is the effective mass of $GaAs$, and e is the charge of an electron [16]. Since we need to work with a magnetic field we will be using the magnetic length

$$l_b = \sqrt{\frac{\hbar}{m\omega_c}} = \sqrt{\frac{\hbar}{eB}} \tag{2.4}$$

as the length scale [3, 17], where

$$\omega_c = \frac{eB}{m} \tag{2.5}$$

is the cyclotron frequency and B is the magnetic field. The magnetic length is the radius of the first energy quantization of the lowest Landau level. Our measurements are primarily at low fields ($\lesssim 1\,\mathrm{T}$) so the magnetic length is around $25-800\,\mathrm{nm}$, which is two to three orders of magnitude larger than the Bohr radius. The heterostructure or quantum well is located fairly deep below the surface of the sample around 300 nm, and is only around 10 nm thick [15]. This thickness, which is much smaller then the

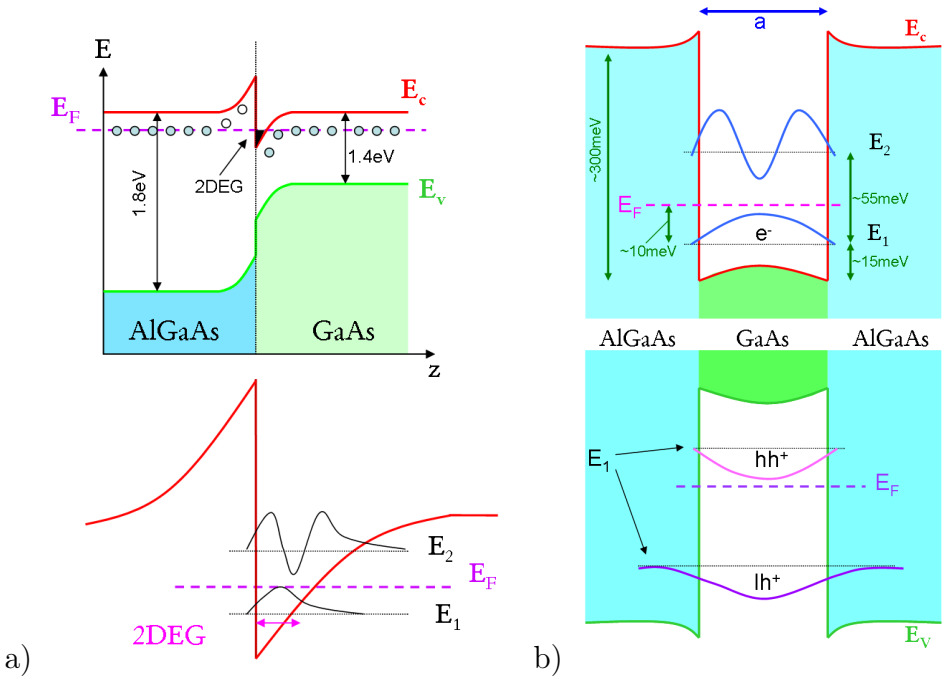

Figure 2.1: a) When the different energy levels of the conduction bands of *GaAs* and *AlGaAs*, modulation doped with *Si*, meet they form a heterojunction, a triangular energy well [18]. At low temperatures the electrons fall into the triangular well which increases the electron density. b) A quantum well is formed when two heterostructures are grown close together. The top is an example of a 2DEG quantum well in the conduction band, and the bottom is an example of a 2DHG in the valence band.

length and width of the sample, makes up the 2D system we measure.

Using the Bohr radius as a length scale, the doping atoms are located far away $(70-80\,\text{nm})$ from the heterojunction but, under low temperature situations, electrons tunnel through the barrier to drop into the energy states set up in the well where they become trapped. At higher temperatures thermal fluctuations lead to the population of high energy z-levels but, as the temperature drops, only the lowest energy z-level becomes filled. By removing a dimension from the bulk 3D crystal, we are able to create a simplified system that is easier to understand and interesting effects arise.

When two of these heterojunctions are grown close together we refer to this as a quantum well. The spacing of these wells can be anywhere from $\sim 15\,\text{nm}$ to $150\,\text{nm}$, and this affects the separation of the spacing between the energy levels in the quantum well. As with the heterojunction the electron based samples are modulation doped with Si which ionizes and provides increased electron densities which get trapped within the conduction band well at low temperature. Conversely, having a quantum well structure also allows for the creation of 2D hole gas (2DHG) systems which occur in the valence band. Instead of modulation doping with Si the 2DHG systems are doped with C. As opposed to the 2DEG case with matching parabolic conduction and valence energy levels and an effective mass of $m^* \sim 0.067m_e$ [3, 8, 19], in momentum space the 2DHG system has degenerate heavy and light hole energy bands. The heavy and light holes differ in their effective mass from $m^* \sim 0.41m_e$ to $m^* \sim 0.08m_e$ [5, 6, 9, 20, 21]. Due to this difference the light holes occur at might higher energies beyond the Fermi energy for our system (which will be explained in the next section). The wells in both the 2DEG and 2DHG samples are $\sim 300\,\text{meV}$ deep and and can be approximated as infinitely high for our purposes. The energy levels from the bottom of the well can then be approximated by

$$\varepsilon_n = \frac{\hbar^2}{2m}\left(\frac{n\pi}{a}\right)^2 \tag{2.6}$$

where n is the integer number of quantized energy and a is the width of the well. For the widths of the wells used in this thesis $(15 - 25\,\text{nm})$ the lowest energy level, $n = 1$,

is approximately 20 meV. The associated wave function is

$$\psi_n(z) = \sqrt{\frac{2}{a}} cos \frac{n\pi z}{a} \tag{2.7}$$

where z is along the crystal growth direction [15]. In the real case the quantum wells have a finite depth, which means there is a small probability that the electron(hole) will tunnel outside the well. To accommodate for this a much more extensive calculation is needed. For our purposes we will use the infinitely deep approximation to present the basic understanding of how energy levels form in 2D systems.

2.2 Landau Levels and Shubnikov-de Haas Oscillations

Landau Levels (LL) are the quantization of energy in the 2D systems that were referred to in the previous section. In the hypothetical situation where the temperature is equal to zero, we assume that the all of the density of states,

$$g(E) = \frac{m}{\pi\hbar^2} \sum_i H(E_i - E) \tag{2.8}$$

where H is the Heaviside step function between Energy level E and E_i, are filled up to the Fermi energy

$$E_F = \frac{\hbar^2 k_F^2}{2m} \tag{2.9}$$

where k_F is the Fermi wave number and m is the mass with no applied magnetic field, which can be seen in Figure 2.2a. When this same system is then placed in a

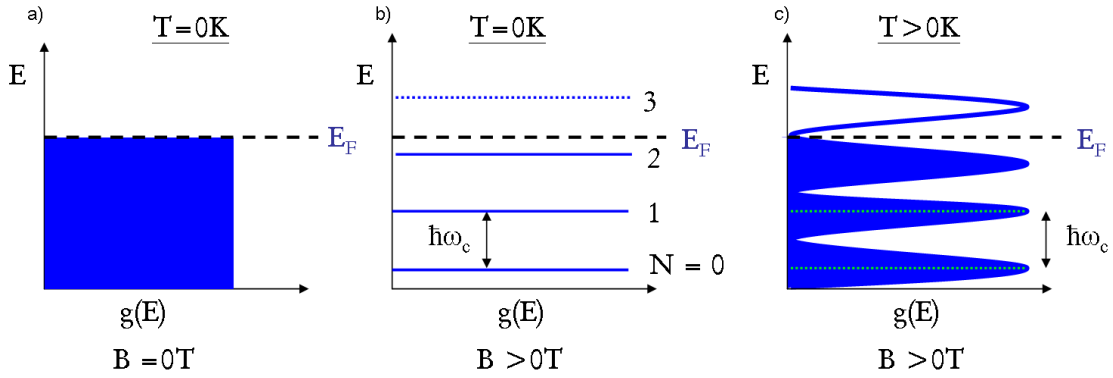

Figure 2.2: a) Density of states, $g(E)$, filled up to Fermi energy at $T = 0\,\mathrm{K}$, and no magnetic field; b) Density of states quantize with applied magnetic field in steps of $\hbar\omega_c$; c) Quantized states blurred with non-zero temperature.

magnetic field the density of states quantize into Landau Levels that separate by $\hbar\omega_c$, where $\hbar$ is Planck's constant and ω_c is the cyclotron frequency (Equation 2.5). This separation is directly proportional to the magnetic field applied (Figure 2.2b). In a more real world situation the temperature of the system is not zero and, due to this and electronic distribution, the Landau levels are smeared out slightly (Figure 2.2c). The result of which is observed in the Shubnikov de Haas oscillations (SdH) which arise in the resistance measurement when sweeping the magnetic field. By changing the magnetic field, the Landau levels separate and pass through the Fermi energy. When this occurs it creates a change in the measurable resistance of the system. By plotting resistance vs. the magnetic field, SdH oscillations develop where the width of the 1/B dependent oscillations is proportional to the full width half max (FWHM) of the Landau levels.

At a higher magnetic field, spin splitting interactions come into play, referred to as

the Zeeman effect. This effect is due to the electric field $E_z = g^* \cdot \mu_b \cdot B \approx 0.3 \frac{\mathrm{K}}{\mathrm{T}}$, where g^* is the g-factor for an electron in the crystal lattice, and $\mu_b \approx 0.671 \frac{\mathrm{K}}{\mathrm{T}}$ is the Bohr magnaton. For a free electron system, the g-factor is defined as -2.002; however, when constrained to the crystalline structure of GaAs, it drops to $g^* \approx -0.44$. As the magnetic field is increased, E_z separates the paired electron spins (up and down) in the density of states which results in a visible effect in the resistance measurement as a function of the magnetic field. As the magnetic field increases so does the Zeeman splitting separation, eventually crossing with adjacent Landau levels. From the SdH oscillations the carrier density, mobility and scattering time can be calculated. The carrier density, n_s, can be calculated by comparing the product of the filling factor and the magnetic field at which they occur with another filling factor and its magnetic field. A simple method for doing this can be found in appendix C. Another method for calculating the carrier density involves taking the inverse of the product of the slope of the Hall resistance and the charge of an electron or

$$n_s = \left(\frac{dR_{xy}}{dB} \cdot e \right)^{-1}. \tag{2.10}$$

The mobility of the 2D system is related to the mean free path between electron-impurity scattering events and can be described using the equation

$$\mu = (\rho_{xx} \cdot e \cdot n_s)^{-1} \tag{2.11}$$

where the resistivity

$$\rho_{xx} = \frac{R_o}{\square} \tag{2.12}$$

or the R_{xx} resistance at zero field divided by the number of squares, $\square$ (or the length between the leads divided by the width of the Hall bar), of the portion of the Hall bar being measured.

Another quantity that can be lifted from the SdH signal is the time between scattering events, τ_{tr}, and the cyclotron scattering time, τ_S. The time between scattering events is calculated by

$$\tau_{tr} = \frac{\mu \cdot m^*}{e} \tag{2.13}$$

where m^* is the effective mass which is equal to $m \cdot m_e$ or a multiplier times the mass of an electron. The cyclotron scattering time is found at the onset of the SdH oscillations in B where

$$\omega_c \cdot \tau_S \approx 1 \tag{2.14}$$

or τ_S is the inverse of the cyclotron frequency (visible in figure 5.5). This also yields the crossover range between the classical Drude regime, $\omega_c \cdot \tau_S \leq 1$, and the quantum regime, $\omega_c \cdot \tau_S > 1$. In the Drude regime we make the assumption that the interaction between the carriers can be described by purely classical inelastic collisions while at higher magnetic fields the description is described by quantum mechanical means with the necessary inclusion of Planck's constant $\hbar$, as described in the previous section.

2.3 Magnetotransport in a 2D system

Our basis for collecting data from a 2D system is magnetotransport. As stated above, increasing the magnetic field applied to the sample changes the separation of the LL through the cyclotron frequency. For each LL that passes through the Fermi energy, E_F, a corresponding SdH oscillation occurs. By sweeping the magnetic field into both positive and negative fields we can also establish the homogeneity of the 2D system by comparing the symmetry of the features of each side. In addition to this, we can identify if there is mixing from the R_{xy} signal by the slope of the SdH features. Ideally a homogeneous carrier density would have a baseline of $0\,\Omega$ and be completely symmetric. If the signal does not have these qualities it could mean that the carrier density is not uniform or the contacts to the 2D system are poor.

A way to modify the magnetotransport signal is through use of a gate to change the carrier density, similar to that found in a field effect transistors. In our case however, it is a 4-terminal measurement where the current is passed through the source and the drain that is made up of leads and the voltage is measured from two additional leads between the two (see Section 4.1). The gate covers the measured portion of the 2D system separated by a dielectric and can provide a positive/negative electric field similar to a parallel plate capacitor. Applying a negative voltage to a gate on a 2D electron system pushes the electrons out and thus decreases the electron density. This is visible in the SdH oscillations when sweeping the magnetic field and ideally, if enough voltage is applied, then all the carriers can be removed from the system (see

Figure 5.20). Conversely, when a positive voltage is applied to a 2D electron system, we expect that this would increase the carrier density. Of course the opposite is true for the application of a positive and negative bias on a 2D hole system. When an electric field becomes too high for the dielectric, a breakdown can be reached which has an adverse effect on the 2D system in the form of leakage current and making an electrical connection from the gate to the 2D system. This could also be caused by impurities or holes in the dielectric. If breakdown of the dielectric occurs then the sample needs to be thermal cycled to room temperature. Since the currents used in the system are on the order of $0.1 - 1\,\mu$A, even a very small leakage current above 10 nA can skew results.

2.4 Irradiation effects on 2D systems

The two sources of irradiation used in conjunction with the samples are through LED and microwave irradiation. LED irradiation is used to achieve the full potential of the carrier density and mobility from the samples. This is achieved by irradiating the sample directly below 10 K. Since the energy of the red or infrared light is around the same energy as the band gap in the $GaAs$ at 1.52 eV (See Figure 2.1), a photoconductivity process occurs which provides the right amount of energy for the carriers to transition to the higher energy state which allows them to tunnel into the energy well [15].

Microwave irradiation over a high mobility 2DEG sample yields microwave induced

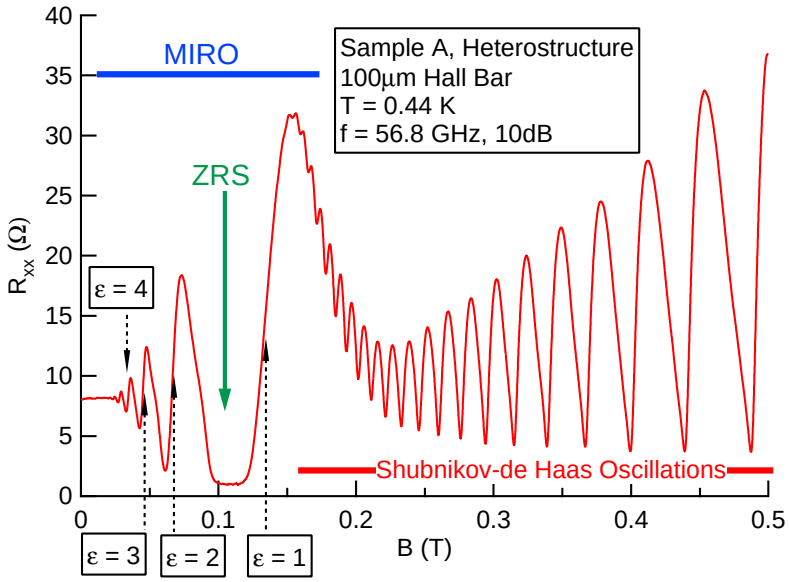

Figure 2.3: Microwave induced resistance oscillation (MIRO) for 56.8 GHz and Shubnikov-de Haas oscillations (SdH). Each MIRO peak is designated by ϵ, with a zero resistance state (ZRS) developed between $\epsilon = 1$ and $\epsilon = 2$ (R_{xx} does not quite reach zero in this example, potentially due to contact resistance).[22]

resistance oscillations (MIRO) which have been studied for some time[13, 23, 24, 25, 26] where $1/B$ periodic oscillations at low magnetic fields ($< 0.5\,\mathrm{T}$) occur at

$$\epsilon = \frac{\omega_{MW}}{\omega_c} \tag{2.15}$$

the integer ratio between the microwave frequency of irradiation

$$\omega_{MW} = 2\pi f_{MW} \tag{2.16}$$

and the cyclotron frequency

$$\omega_c = \frac{e \cdot B}{m^*} \tag{2.17}$$

where m^* is the electron effective mass. These features, where ϵ is an integer number, are visible as sharp oscillations in the longitudinal resistance at low magnetic fields of high mobility samples. Each of these resonant peaks are associated with transitions between the lowest Landau level, N, and the next Landau level, N+ϵ. MIRO does have a temperature dependence and is much stronger at lower temperatures, but can be seen as high as 20 K. This is especially important when trying to minimize the overlap with the SdH signal which has a much higher temperature dependence and gets pushed out to higher magnetic fields at higher temperatures. This will come into play in section 5.2 on edge magnetoplasmon oscillations (EMPO). Of course, when irradiating a sample at low temperatures with microwaves we are also introducing heat into the system which in turn affects the ^3He bath temperature. To minimize this we can decrease the amplitude of input power. However, since MIRO is a non-linear effect, the R_{xx} signal increases in amplitude until it saturates due to the heating effects of the microwaves, at which point it decreases linearly.

In certain situations, the resistance minima can reach a zero-resistance state (ZRS) between the peaks [13, 27]. This feature is dependent on high mobility and could also potentially be a result of negative resistance. An example of this would be in Figure 5.2 and 5.8a. In these examples the ZRS does not occur exactly when $R_{xx} = 0\,\Omega$ due to inhomogeneities in the density of the samples.

What has been hinted at in previous data [27] and finally observed in greater detail with the new probe in Section 3.4 has been fractional MIRO (FMIRO). These

oscillations are more visible with lower MW frequencies; occur in higher magnetic fields than MIRO; are commonly dominated by Shubnikov-de Haas (SdH) oscillations; and are periodic in the magnetic field due to their inverse integer relationship to Equation 5.1, where $\epsilon = \frac{1}{2}, \frac{1}{3}, \frac{1}{4}, \frac{1}{5}, \ldots$.

While the DC transport phenomena in MIRO and ZRS have been studied extensively, the corresponding high frequency conductivity has only been studied to a limited extent. Dmitriev et al. [28] calculated the frequency-dependent conductivity $\sigma_{xx}(\omega)$ of 2D electrons subjected to a transverse magnetic field and smooth disorder. The interplay of Landau quantization and disorder scattering gives rise to an oscillatory $\sigma_{xx}(\omega)$ at integer values of $\epsilon = 1, 2, 3, 4, 5, \ldots$ (the Cyclotron Resonance (CR) harmonics). They found that the effect is suppressed both in the classical limit, $\omega_C \cdot \tau_S \to 0$, and the clean limit, $\omega_C \cdot \tau_S \to \infty$, and can be best observed in the semi-classical crossover range, $\omega_C \cdot \tau_S \sim 1$, where τ_S refers to the quantum scattering time, or as stated above, the cyclotron scattering time. The crossover range is identified by the location in the magnetic field that R_{xx} starts showing SdH oscillations or where the Landau Levels (LL) start to quantize.

Studenikin et al. reported experimental results for MW absorption/reflection in the MIRO regime [29] with frequencies from $30 - 50\,\mathrm{GHz}$ using a cylindrical cavity and bolometer. They were able to make a detailed study of the MIRO line shape and temperature dependence. The MW absorption signal was identified by subtracting the background dependence from the total absorption signal. For their sample they

were not able to detect any resonant absorption at any of the CR harmonics. At this frequency range, the magnetic field below the SdH signal can be taken up with the fundamental CR and higher orders of MIRO. This also means that the LLs have separated and the classical Drude model approximation no longer applies. In a much higher MW frequency range, $230 - 2500\,\mathrm{GHz}$, Tung et al. [30] measured the sub-THz transmission in MIRO. In these experiments only a single peak, corresponding to the fundamental cyclotron resonance, $\omega_{MW} = \omega_C$, in the AC conductivity, was observed. This regime satisfied the clean limit, or $\omega_C \cdot \tau_S \gg 1$, meaning that the signal input frequency was so high that the respective signal was well into the SdH, or quantized LL, region.

Zudov et al. reported FMIRO in the frequency range from 27 to 47 GHz and suggested that FMIRO could be understood if the multi-photon mechanism is relevant [31]. Dorozhkin et al. measured the magnetoresistance oscillations under similar MW irradiation in the MIRO and FMIRO regime, as well as suggesting that these MW LL transitions can occur even when the irradiation energy is well below that of the transition, thus potentially ruling out the necessity for simultaneous multiphoton transitions. Their research also suggested that lower MW frequencies improve the chances of revealing the FMIRO signal due to LL overlap [32]. It remains an open question as to the relevance of CR harmonics in AC conductivity to the DC resistance oscillations commonly observed in high-mobility GaAa/AlGaAs 2DES. Moreover, a related question can be asked if we are in the regime where FMIRO is relevant.

2.5 Cyclotron Resonance

From the previous section we were introduced to the cyclotron resonance equation 2.17. A simple way to look at cyclotron resonance in real space is that it is the resonance when a charged particle circulates in a 2D plane perpendicular to an applied magnetic field due to a force applied from the simple equation of

$$F = q(v \times B) \tag{2.18}$$

where q is the charge of a carrier, v is the velocity of the carrier, and B is the applied magnetic field. It takes a certain amount of energy to cycle the charged particle. If an outside applied frequency, of the matching energy, is applied to this system then a resonance occurs and energy is absorbed by the system.

Another way to look at this is through probability space where the cyclotron resonance is achieved when the cyclotron frequency (Equation 2.17) equals the frequency of irradiation, ω_{MW}. This occurs due to the transition energy $\hbar\omega_c$ between LLs N and $N+1$ matches up with the energy of ω_{MW} to make the transition to the next LL, $N+1$ [33]. This means that there is an absorption of energy at a given magnetic field, B, for a given frequency, ω_{MW}. The bandwidth resonant frequency for the high mobility 2D samples ranges from far infrared [19], through microwaves [8, 10, 11] and as high as terahertz [30, 34]. Depending on the frequency of irradiation of 2DEG ($m^* \approx 0.067 \cdot m_e$), the magnetic field where the resonance occurs can shift from sub-

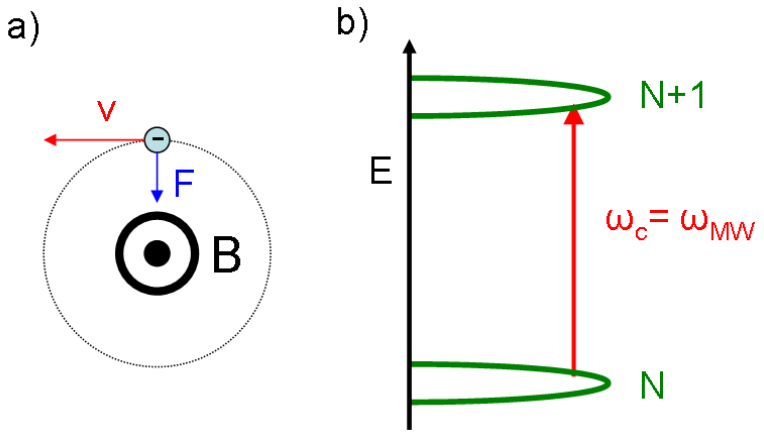

Figure 2.4: a) Cyclotron resonance of a charged particle in a magnetic field with a velocity in real space; b) Cyclotron resonance by matching the irradiation frequency with the Landau Level separation in probability space.

Testla values in the case of terahertz to multiple Tesla for far infrared. In the case of 2DHG samples, the effective mass of heavy holes is about an order of magnitude higher ($m^* \approx 0.41 \cdot m_e$) and we expect this to directly increase the cyclotron resonance peak location of the magnetic field by a respective order of magnitude.

At higher mobilities, or equivalently less impurities, there is a higher absorption of microwaves since the charged particles can travel longer distances without scattering. Unlike MIRO and FMIRO that relate to the resulting resistance oscillations at transition energies, the cyclotron resonance can be measured directly using a transmission or absorption setup and can yield the effective mass and the cyclotron time constant [7]. These values can be deduced from the peak location B, and the inverse of the full width half max of the transmission peak, respectively.

Other methods for measuring the cyclotron resonance, other than optically, can be done by measuring the amplitude of the SdH oscillations [35], or through doing

a calorimeter measurement utilizing the physical mechanism of a samples increase in temperature when at the resonant magnetic field while being exposed to a continuous wave microwave. This measurement was done by Yuan, Z. Q. [6] using the 15nmQW 2DHG sample and a specialized sample holder designed to accurately measure the sample's temperature. The effective mass of $0.41m_e$ found from this technique matched with other measurements on 2DHG samples [10]. One drawback of this technique was that the sample could only be measured at a base temperature of 4.2 K due to the sample holder design. The effective mass multiplier can also be calculated using the SdH amplitude temperature dependence from Tan et al. [4].

2.6 Magnetoplasmons

A plasmon in a 2DEG can be thought of as a coherent oscillation of the electrons (or holes) constrained by geometric effects such as length and width of the 2DEG Hall bar, or the separation between leads. For various dimensions there are similarly various plasmon frequency resonance [33]. Similar to the cyclotron resonance excited by microwaves, plasmon resonances can be excited by microwaves when they match the plasmon frequency,

$$\omega_{MW}^2 = \omega_p^2 + \omega_c^2 \tag{2.19}$$

for a 2DEG, with the plasma frequency

$$\omega_p = \frac{n_e e^2 k}{2\epsilon\epsilon_o m^*} \tag{2.20}$$

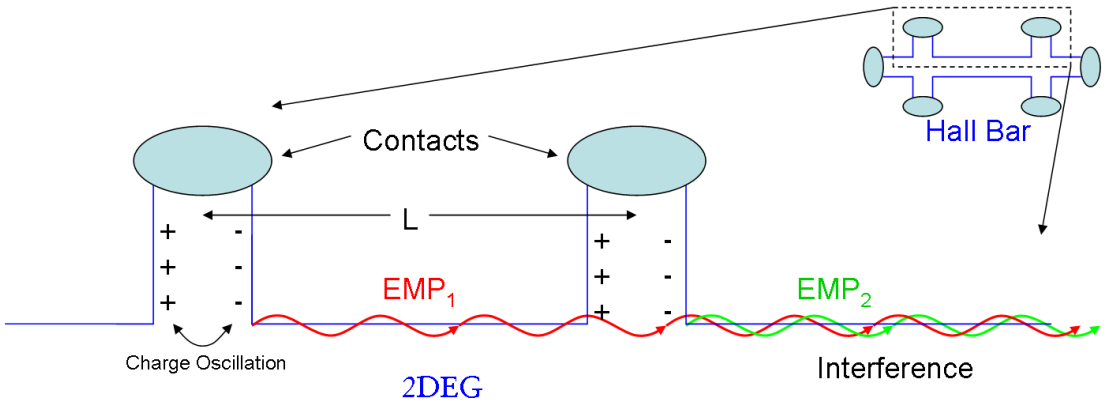

Figure 2.5: Edge magneto plasma model from Kukushkin et. al, which does not quite explain the system. In the real system the edge magnetoplasmons are non-local and travel around the entire sample to constructively/destructively interfere.

where $k = \frac{\pi}{w}$, where w is the width, and $\epsilon\epsilon_o$ is the dielectric constant. From this equation we see that resonance within the bulk 2DEG requires low frequencies compared to microwaves. Conveniently for the frequency range we have access to $(26 - 150\,\mathrm{GHz})$, we can expect edge resonance modes.

These edge plasma modes are different from the bulk modes due to their affinity for the edges of the Hall bar. These edge modes are visible as very small periodic oscillations in the magnetic field, ΔB. Previous research on magnetoplasmons [14, 36] speculated that the edge magnetoplasmons are excited by charge oscillations in the edges of the leads of the Hall bar that are separated by a length and that

$$\Delta B \propto \frac{n_s}{\omega_{MW} L} \tag{2.21}$$

where n_s is the electron density, the microwave frequency 2.16, and L the distance

between the contacts. In this model the leads act as small antenna with charge oscillations that edge magnetoplasmons peel off of and travel down the edge of the Hall bar (see figure 2.5). The propagating edge magnetoplasmons then interfere with one another leading to oscillations in the photovoltage measurement between two leads, something similar to an interferometer, where instead of changing the distance L, the wavelength λ of irradiation, changes due to sweeping the magnetic field. The issue with this model is that, due to the magnetic field, there is a chirality in regards to which way the edge magnetoplasmon will travel from the leads. Meaning that, depending on the direction of the magnetic field, all edge magnetoplasmons will propagate in the same direction around the Hall bar, leaving the interference to occur past both leads that are measuring the photovoltage.

Chapter 3

Experimental Apparatus

3.1 Cryogenic system

For all of the experiments we used a top loading Oxford Helium 3 cryogenic system to reach temperatures of 0.3 K. The probes that were used with this system were mounted on top of the sample space and separated by a gate valve. This allowed us to pump out the probe to a sufficiently low pressure (5.5×10^{-5} torr) and close it off so the gate valve would be opened allowing the probe to be lowered to its final resting place in the center of the 12 T superconducting magnet. To prevent any air from the outside leaking in, we continued to pump on a small chamber that separated the inside of the probe from atmosphere, each with an associated O-ring seal. While the rod of the probe slid through the two O-rings, a turbo pump caught any air that would escape from atmosphere into the system. When the probe was fully loaded into the system, a flange at the 1 K stage of the probe would meet with the 1 K pot ensuring a good thermal connection. The sample space itself used a closed system to condense and pump, using an absorption pump, on ^3He to reach its base temperature.

3.2 Samples

The samples used for these experiments were of $GaAs/AlGaAs$ heterostructures or quantum wells of various widths and supported high mobilities in 2D electron or hole gases. All of these samples were patterned with photolithography and etched into Hall bars of various dimensions (see Table 3.1). Each sample had 8 to 10 contacts and the latter samples were fabricated with gates. The edge magnetoplasmon experiment samples and the 20nmQW 2DEG sample were pre-existing high mobility samples with straight leads perpendicular to the length of the Hall bar. The other samples that were fabricated had wedge shaped leads to prevent any one edge magnetoplasmon resonance frequency. For the gated samples, the dielectric used were either 500 Å of Al_2O_3 or in the case of the straight CPW $500 - 1000$ Å of Si_3N_4.

3.3 Waveguide Geometry

Initially the measurement probe used was designed to have a Ka band waveguide (WG-22) along the center length of the probe. This provided the sample mounted directly at the bottom of the waveguide with irradiation from a Gunn diode at the top of the probe. In this arrangement, the sample could be irradiated from 26.7 GHz to 150 GHz. Since these frequencies were mostly well beyond the bandwidth of the waveguide ($26.5 - 40$ GHz), we could assume that the propagation through the waveguide was through higher order transmission modes. At the opening of the waveguide near the sample, we expected an electric field distribution solution that was maximum

Name	Wafer	Size (mm)	$n_s\,(\mathrm{cm}^{-2})$	$\mu\,(\mathrm{cm}^2/\mathrm{Vs})$
Sample A	HS97.1	0.1×2	2.27×10^{11}	8.3×10^6
Sample B	HS97.1	0.2×2	2.45×10^{11}	11×10^6

Table 3.1: Samples used for the Edge Magnetoplasmon experiment (Section 5.2).

Name	Wafer	Size (mm)	$n_s\,(\mathrm{cm}^{-2})$	$\mu\,(\mathrm{cm}^2/\mathrm{Vs})$
Straight CPW	25nm QW HS98	0.1×2	4.55×10^{11}	11.8×10^6

Table 3.2: Samples used for simultaneous magnetoresistance and transmission measurements (Section 5.3.1).

Name	Wafer	Size (mm)	$n_s\,(\mathrm{cm}^{-2})$	$\mu\,(\mathrm{cm}^2/\mathrm{Vs})$
15nmQW 2DHG	asymmetric	1×3	2×10^{11}	8×10^5
20nmQW 2DHG	symmetric	1×3	2.03×10^{11}	0.9×10^5
25nmQW 2DEG		1×3	2.69×10^{11}	1.50×10^6
HS 2DEG		1×3	2.00×10^{11}	4.11×10^5
HJ 2DEG		1×3	1.9×10^{11}	1.07×10^6

Table 3.3: Samples used for meander line transmission measurements (Sections 5.4.1 and 5.4.2) .

at the center of the waveguide and disappeared at the edges (see Figure 3.1).

The sample was much closer to the opening of the waveguide than the wavelength of the microwaves being sent in, which meant we did not need to worry about standing waves and only needed to consider near field effects. The benefit of using a waveguide based probe was that it allowed for high power microwave transmission. However, it was very difficult to achieve the same frequency and power using the Gunn diodes due to being controlled by micrometers, and the power output varied dramatically depending on their setting. Granted, whatever Gunn diode power output was achieved, it would mostly end up at the sample. The irradiation from the waveguide suggested a Faraday distribution of electric and magnetic microwave fields (E^ω and H^ω, respec-

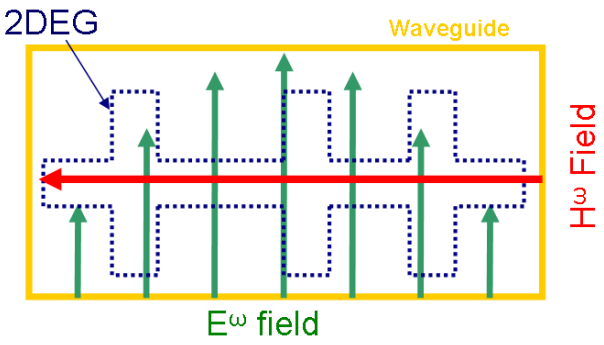

Figure 3.1: Field coruscation in the microwave waveguide at lowest transmission mode with respect to a mounted 2DEG sample. In this geometry both the electric and magnetic microwave fields are in the plane of the sample.

tively) both in the plane of the sample. For the bandwidth of the waveguide, we would expect the field distribution to be similar to Figure 3.1. However, higher frequencies would have more complex transmission modes. One way to create directed E^{ω} and H^{ω} fields would be to design a cavity resonator [21, 29, 37, 38], which would have a fairly small bandwidth, or design a new probe with a different microwave delivery setup, such as coax-based transmission line.

3.4 Transmission Line Geometry – New Probe Design

This new system would be the digital circuit-based analogy to that of the analog waveguide. Instead of using a waveguide, we would incorporate coax lines into the probe using an Anritsu MG3694B microwave frequency generator. This would provide the sample with $2 - 40\,\text{GHz}$ and a tunable power output of $-100 \rightarrow +20\,\text{dBm}$ ($1 \times 10^{-10} \rightarrow 100\,\text{mW}$). To incorporate a coax line into the probe, we had to take certain precautions with the new design. To avoid large microwave power losses for the

length of the probe from 300 K to the 4 K stage, we used 3 mm diameter copper low-loss coax. While this provided low microwave power loss, it brought in a very large amount of heat down to the 4 K stage of the probe. To isolate this heat from the lower portions of the probe, a large copper heat sink was used. Below this stage a higher loss/lower thermal transmission coax line of inner conductor beryllium copper with a outer conductor of stainless steel was used to transmit microwaves down to sample holder. This line was again heat sunk at the 1 K stage which directly connected to the 1 K pot via a copper braid. At the sample holder, the coax line had a connector where shorter delivery lines could be connected. Initially these shorter delivery lines were designed to distribute microwaves right on top of the sample with a linear or dipole antenna geometry (Figure 3.3). This blanketed the sample with microwaves similar to the waveguide arrangement, with less control over the orientation of the fields.

The sample holder in this arrangement was made out of Stycast 1266 with added graphite (see Appendix B) to help absorb any stray microwaves. Once it was established that we could see microwave response from the 2D system in the form of MIRO, the next step in the probe design was to incorporate a second coax line that would take the power out to a power sensor on top of the probe at room temperature.

To interface with the $GaAs/Al_xGa_{1-x}As$ sample, we mount the sample in line with a co-planar waveguide [39] (CPW) made of top/bottom copper clad Rodgers TMM10i, which is specifically designed for high frequency/low temperature applications. It

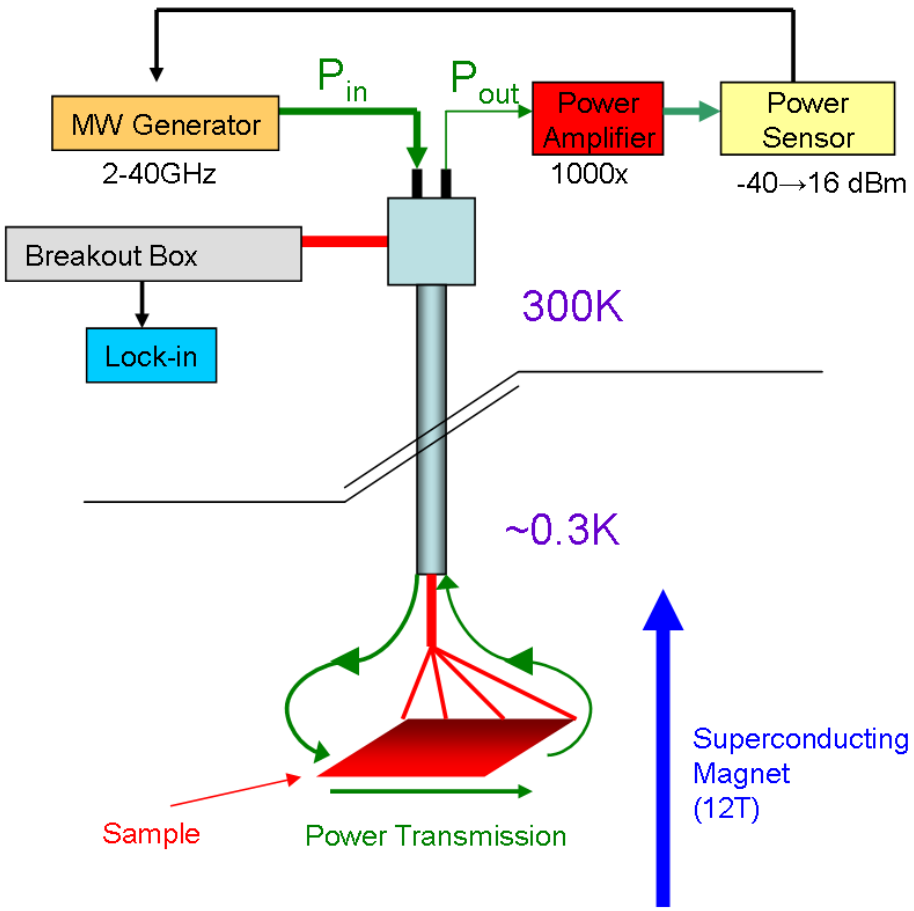

Figure 3.2: New transmission probe diagram.

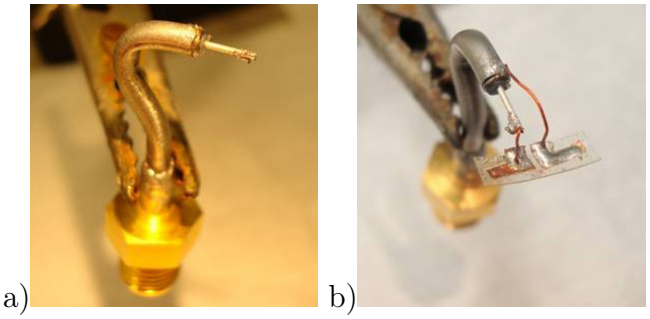

Figure 3.3: a) Dipole antenna; b) The linear antenna was designed to create an analogous field distribution to the waveguide. Each antenna would be mounted directly on top of the sample, $\sim 1\,\mathrm{mm}$ away.

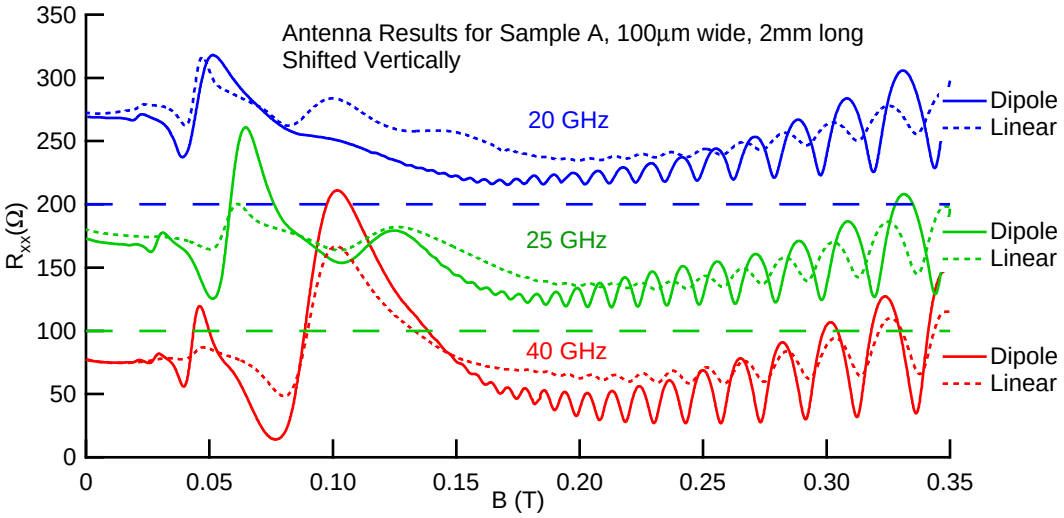

Figure 3.4: Example of results from irradiating the 2DEG sample with microwaves using the dipole and linear antenna.

was made by using an 0.26 mil carbide end mill that removed the copper cladding on either side of a predetermined 1 mm copper strip, which was designed to be impedance matched to 50 Ω [40]. The co-planar waveguide provides a way to take the microwave signal from the coax and flatten it into a geometry that could interface with a sample that had been photolithographically defined and e-beam evaporated CPW.

In Figure 3.5 we can see a cross-section of the CPW used in this experiment. In this form we can see that the 2DEG fits in the region where E^{ω} and H^{ω} propagate in the plane perpendicular to the 2DEG respectively, which we will consider to be a non-Faraday geometry. This effectively isolates the components of the MW and focuses the MW power across the Hall bar without substantial losses and with minimized uncontrolled effects. All of the components of the CPW, on and off the sample, have been designed to be impedance matched to 50 Ω; however, there is a high probability

that the transitions between each CPW and the coax line could result in a mismatch.

These mismatches could result in frequency-dependent reflection or absorption from standing waves. If we had access to a network analyzer for the frequency range of $2 - 40\,\mathrm{GHz}$, we would be able to measure the frequency dependent reflection. However, to insure that we used a microwave frequency that would be transmitted adequately, we took a power profile of the frequency range. This was done by stepping the microwave frequency in small steps ($0.01\,\mathrm{GHz}$) and measuring the microwave power output and frequency with a fixed power input (See Figure 3.6).

In one geometry, each CPW was wrapped around three sides of a brass block, at the center of which was a groove fitted for the $GaAs/AlGaAs$ sample. The geometry was inspired by the Engle Group [41] where the CPW on the sample was connected to the copper CPW by silver paint. Contacts to the 2DEG Hall bar were made perpendicular to the CPW on either side of the brass block sample holder. This geometry allowed us to measure the magnetoresistance and microwave power absorption simultaneously in a superconducting magnetic field. In most cases, due to the large distance through the coax lines, there would be a large amount of microwave power loss ($\sim -15\,\mathrm{dBm}$ for each coax line). To compensate for this and the limitations of our power sensor ($-40\,\mathrm{dBm}$), a microwave power amplifier (BZ0840LD1 from B&Z Technologies) was connected to the power output coax line at the top of the probe. This was able to boost the signal ~ 1000 times (or $\sim +30\,\mathrm{dBm}$) to insure it would not fall below the detector's range. Using the power amplifier, the signal

(a)

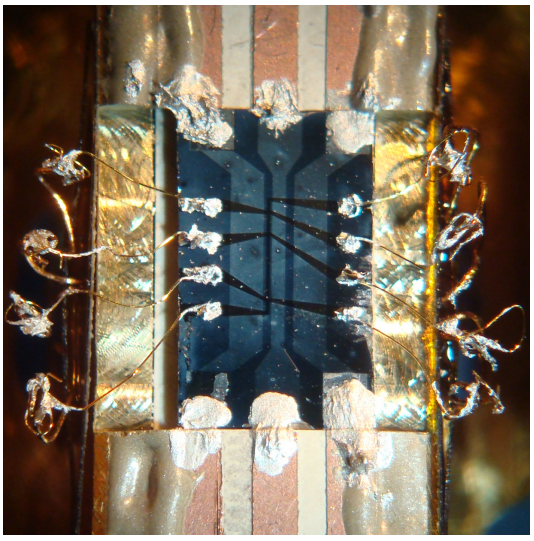

(b)

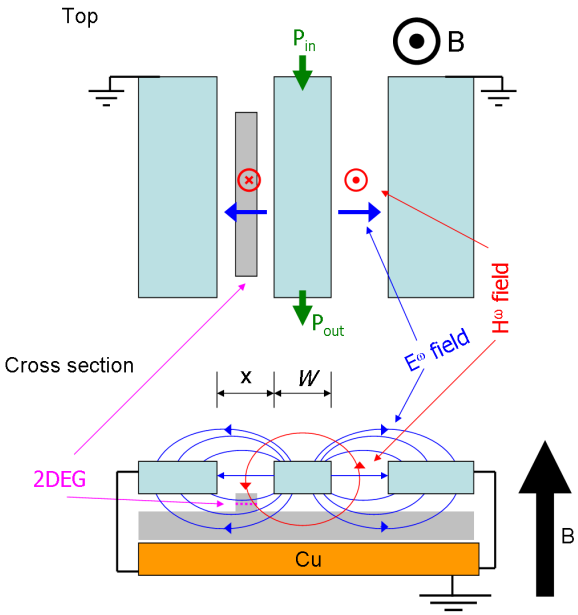

(c)

Figure 3.5: a)Brass block with CPW, the center conductor and ground plans connect to that of the microwave coax lines on either side; b)Mounted straight CPW sample onto brass block; c) Top view and cross section view of the straight CPW geometry in relation to the 2DEG sample.

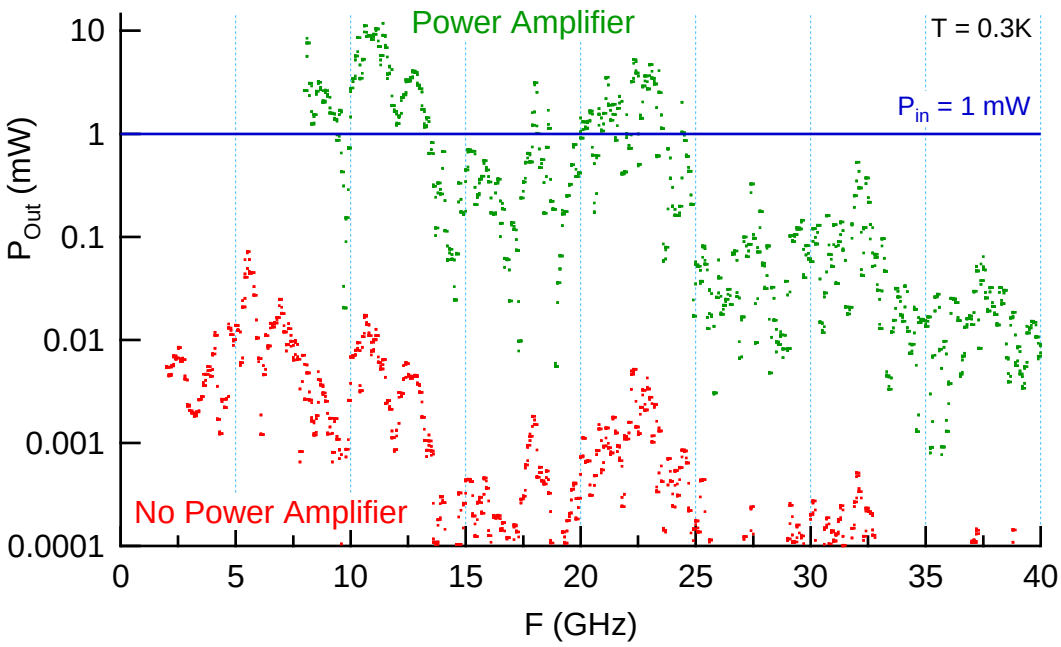

Figure 3.6: Power profile with and without power amplifier.

only changed slightly and preserved the features. Each time the sample and brass block are mounted into the probe, the overall frequency dependence changes slightly, similar to a fingerprint for each sample holder. Small changes to the input frequency can result in large changes in the output power. To select what frequencies we would focus on, we created a power transmission profile for the entire $2-40\,\mathrm{GHz}$ spectrum, which allowed us to then choose the stronger signal (See Figure 3.6).

The rest of the probe was designed using resistive phosphor bronze wiring for greater thermal isolation. This wiring was also thermally connected to the heat sinks at the $4\,\mathrm{K}$ and $1\,\mathrm{K}$ stages. The lower portion of the probe was designed in three stages so as to be modular, allowing the replacement of stages when necessary (see Appendix D). The final modular piece to be designed was the sample holder itself,

which is made of Stycast 2850FT (Catalyst 24LV), with graphite, which has a thermal expansion coefficient similar to brass, with which it would be directly interfaced. The reason for choosing this material besides the thermal expansion properties, was to absorb microwaves and to avoid creating cavity resonances which we found was the case with a brass version of the sample holder and the meander line CPW geometry. Since creating a customized brass block for each sample was time consuming and each had their own individual power profile, we opted to create one sample holder based on the CPW meander line geometry for situations that did not require directed E^{ω} and H^{ω}. An example of this can be seen in Figure 3.7, where the meanderline would take the place of the mounted samples from the previous straight CPW experiment. This arrangement would give us a standardized way to irradiate the sample from the back by placing the sample on top of the meander line. The meander line was photolithographically designed to have a center conductor width of 100 μm and a gap of 63 μm that was evaporated using a $AuPd$ alloy on a piece of undoped GaAs with the crystal orientation of $< 111 >$. The alloy was chosen for its lack of cyclotron resonance due to its low alloy scattering length while still being electrically conducting. When pure metal was evaporated for the meander line geometry, we noticed a very large background signal that drowned out the signal from the 2D system. For this reason, we minimized the amount of pure metal in the sample holder by using brass and other alloys, including an $AuPd$ gate for the sample.

The meander line was mounted in a similar fashion to the samples on the brass

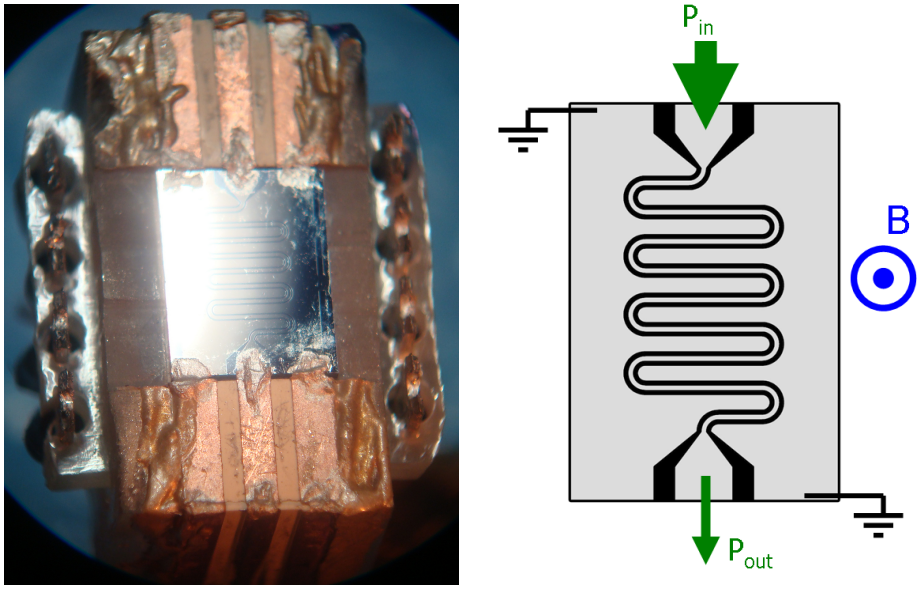

(a) Stycast Block with contacts. (b) Diagram of Meanderline.

Figure 3.7: Meander line antenna geometry where samples are placed on top and irradiated from the back (see figure 4.6).

blocks, but to a Stycast 1266 block to reduce eddy current heating. This geometry allowed for the ability to strap a sample (using a thin strip of Teflon tape) to the meander line block and wire it up similar to a normal chip carrier, the only difference being that microwaves could radiate the sample from the back side, using the meander line as an antenna. This arrangement allowed us to measure the power transmission across the sample, provided the back side of the sample was polished to remove any metallic layer that could reflect the microwaves. In the event that the metallic back side was not removed, we found that the samples with $\lesssim 50\,\mu$m of *Ga* reflected a majority of the microwaves irradiated from the meanderline. In fact, we were able to measure a very weak cyclotron resonance from the *Ga* when the sample was not polished.

Chapter 4

Measurement Technique

4.1 Magnetotransport measurement

The basic form of measurement technique we have at our disposal is the magnetotransport measurement. This is a simple 4-terminal measurement where we pass current through two leads in the 2D gas and measure the voltage of two other leads using a lock-in between the current input and ground leads. This effectively removes the contact resistance since no current is flowing between through the voltage leads. This is important due to the sample resistance being much lower than that from the contacts by a few orders of magnitude. The contacts are made from annealing In, or $Ge/Pd/Au$, on the surface of the sample which from thermal migration make an electrical connection to the 2DEG $\sim 3000\,\text{Å}$ below the surface by annealing (See Appendix A.1). The sample is placed in a superconducting magnet that can be swept from $\pm 12\,\text{T}$. Data is taken using a LabVIEW acquisition program that interfaces with the GPIB ports connected to lock-ins that then plot out the resistance as a function of the magnetic field. This is the basis of our quantum transport measurements where we can adjust the input current and magnetic field sweep rate.

Our samples require the irradiation of an LED at low temperature to increase the electron density. To do this we decrease the temperature of the probe to below $10\,\text{K}$

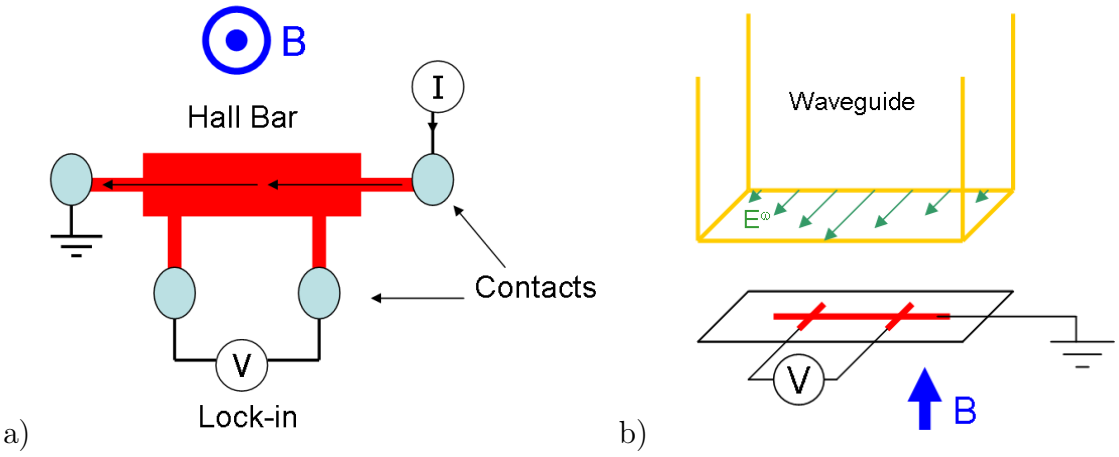

Figure 4.1: a) 4-terminal measurement, used to avoid including the contact resistance. The input resistance of the lock-in is so large (10 MΩ) that there is no current that travels through the voltage leads. This means that all the current goes to ground and the voltage measured by the lock-in is the potential drop between the leads of the Hall bar, insuring an accurate resistance measurement of the 2D system and removing the contact resistance; b) Photovoltage measurement.

and then run constant current of 10 mA through a red or infrared LED pointed at the sample. The reason for using this wavelength is to match or exceed the 1.52 eV band gap of *GaAs* junction. Only short irradiation time, five minutes, is necessary to saturate the uncovered 2DEG. However, in the cases where the samples have a gate, the irradiation needs to be from the side of the sample. This also increases the irradiation time sufficiently, 30 minutes to one hour, to ensure uniformity of the saturation across the sample. If the waveguide probe is used, then white light shined down through the waveguide also works, with the added advantage of not heating up the sample as much as the LED.

4.2 Microwave Irradiation and Photovoltage

In addition to the magnetotransport measurement, we also have the ability to simultaneously irradiate the probe with a continuous wave microwave. Using this arrangement we can observe microwave induced resistance oscillations (MIRO), and other microwave response (Section 5.1). Alternatively by floating all but one grounded contact and irradiating the sample with microwaves (as seen in Figure 4.1), we can measure the photovoltage between two leads of the sample. This enables us to directly measure the voltage that the microwaves are inducing on the leads. In our results we find that sometimes this signal is actually cleaner or equivalent to the more complex methods for taking data, such as the single modulation technique for the edge magneto plasma measurement in Section 5.2.

Using the waveguide probe we are able to irradiate the sample with microwaves ranging from $26.5 - 150\,\mathrm{GHz}$. These frequencies were achieved with custom made Gunn diodes which are adjusted by one to three micrometers depending on their individual bandwidth. The micrometers allowed for variable frequency and associated power output, but lacked reproducibility. To combat this, we used a frequency counter to find the input frequency and observed the temperature change at the sample location to gauge the power. Each Gunn diode received power from a control box which in turn could be amplitude modulated. This option came into relevance with the double modulation technique explained in the next section. To control the power going down to the sample, a digital attenuator was inserted in line with the

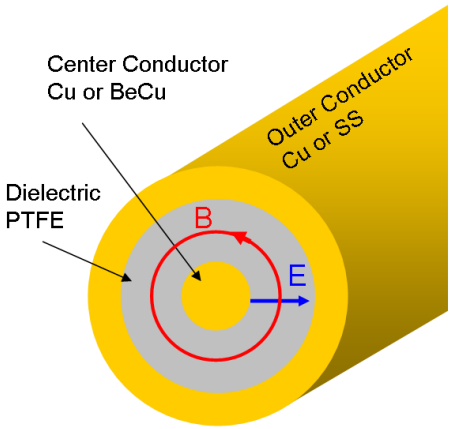

Figure 4.2: Cross-section of coax waveguide.

waveguide.

By incorporating a coax line into the new probe we effectively went from an analog microwave system (waveguide/Gunn diode) to a digital circuited based system. The huge advantage of this is that the output frequency and power from the microwave frequency generator was very stable and reproducible. To interface with the microwave frequency generator, we used a LabVIEW program which could control the frequency, power, sweeping each of these parameters, and amplitude modulation of the output frequency via GPIB. Having this ability dramatically decreased the time it took to take microwave data, and increased the amount of data that could be taken. In addition to providing microwaves down to the sample, we were also able to incorporate a second coax line that went back up to room temperature which could carry a transmission signal to a microwave power sensor. Similar microwave irradiation and photovoltage measurements were done to the waveguide probe.

4.3 Microwave Single Modulation Technique

If the signal is very small compared to noise or the basic magnetotransport signal, we require a more sensitive technique, one of which is a double modulation technique initially presented in the PhD thesis by Michael Zudov [12]. The initial iteration of this technique involved using two frequencies, f_1 and $2f_1$ (both synchronized to a function generator), where $2f_1$ drives the current through the Hall bar and f_1 chops the microwave Gunn diode signal. In this arrangement, the lock-ins measure both the photovoltage and ΔR, which is the resistance with microwaves (R_{MW}) minus the resistance without microwaves (R_o), which are out of phase by 90^o. For our system we utilized a single modulation technique, presented in Zudov's PhD thesis [12], where the current provided to the sample via lock-in 1, f_1, is modulated with a high frequency (909.1 Hz) and the X output from that lock-in is fed into A of lock-in 2. This second lock-in is modulated with f_2, the same frequency as the microwave source (17 Hz) as seen in Figure 4.3. Lock-in 2 needs to be phase adjusted to minimize the imaginary Y component, which is usually around $\phi \approx 180^o$.

This setup creates a high sensitivity differential photoresistance measurement, ΔR, where the signal without the microwaves (R_o) is subtracted instantaneously from the resistance with the microwave signal (R_{MW}). The benefit of this is increased sensitivity by eliminating the background magnetotransport signal, the result of which is the photoresistance signal. However, in this process the R_{xx} signal from lock-in 1 is not usable, other than to provide the X output to the second lock-in. The TTL signal

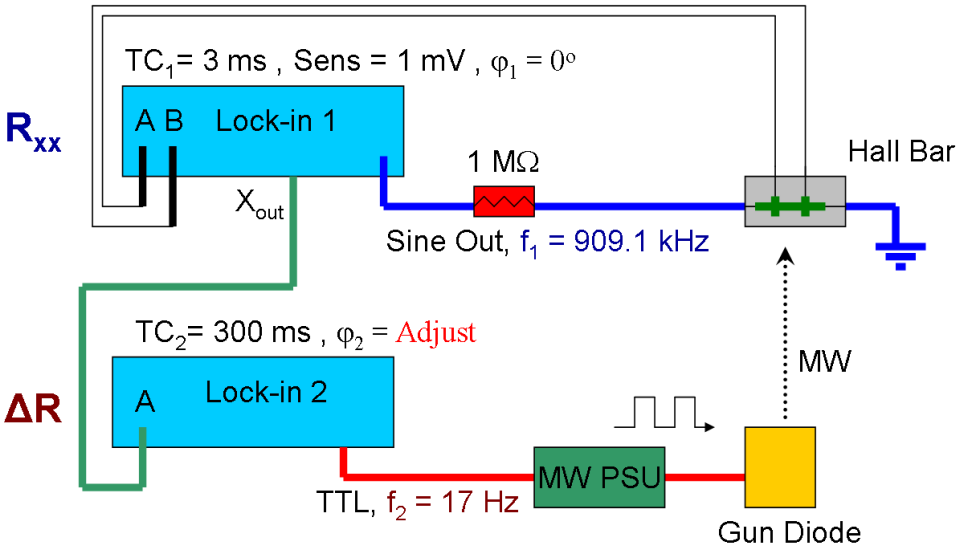

Figure 4.3: Diagram of the single modulation technique to measure ΔR, where $\Delta R = R_{MW} - R_o$.

(square wave) from lock-in 2 is used to modulate the microwave power supply, which translates into a square wave modulated microwave signal. This signal is picked up through the X output from lock-in 1.

From the equation

$$R_{MW} = R + \Delta R \cdot (\frac{1}{2} + \frac{2}{\pi}[sin(x) + \frac{sin(3x)}{3} + \frac{sin(5x)}{5} + \ldots]) \tag{4.1}$$

where the series represents the square wave signal, we can pull out the ΔR [12].

We used this setup for measuring ΔR in the edge magnetoplasmon experiment but quickly found that using a simpler photovoltage technique would yield the same results (see Figure 5.8). However, this technique was the basis for our gate modulation technique for the ΔP measurement, described later in the transmission technique

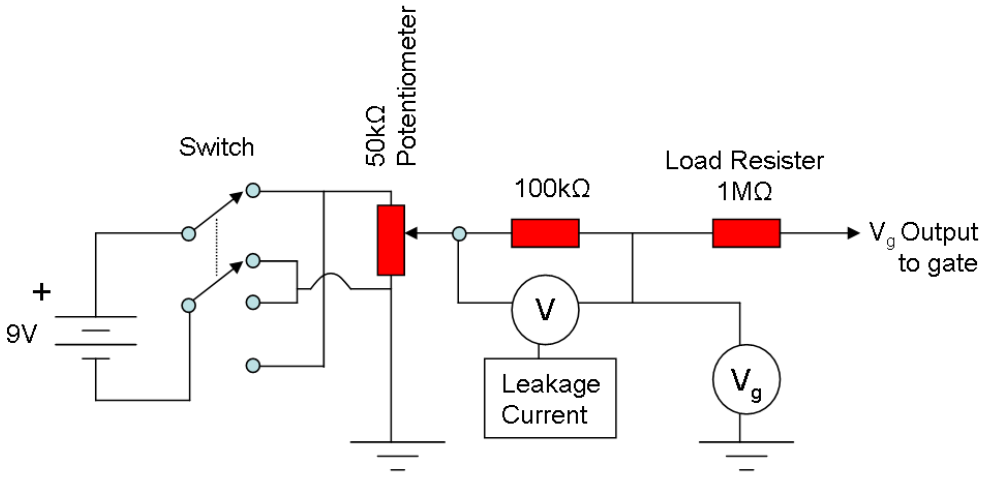

Figure 4.4: Gate box circuit diagram. The leakage current can be calculated from $I = \frac{V}{100\,\mathrm{k}\Omega}$. If there is no leakage current then the voltage measured at V_g is the same as the output voltage to the gate.

section.

4.4 Gate Measurement

Another powerful technique we have is using a gate evaporated on top of the Hall bar to change the carrier density. For our samples we initially evaporated a dielectric of Al_2O_3 or used a PECVD to deposit Si_3N_4 on the surface (Appendix A.1), either 500 Å or 1100 Å thick. On the surface of the dielectric, 50 Å of Ti was evaporated as an adhesion layer, followed by a 1000 Å thick gate of $AuPd$ using an e-beam evaporator. Using the circuit from Figure 4.4, we can apply a gate voltage, V_g, from a battery to gently adjust the gate voltage with a constant voltage which in turn adjusts the carrier density. In gates that use the Si_3N_4 dielectric, we note that there is a slight hysteresis in the I-V plot due to mobile charges in the dielectric from Figure 4.5. We

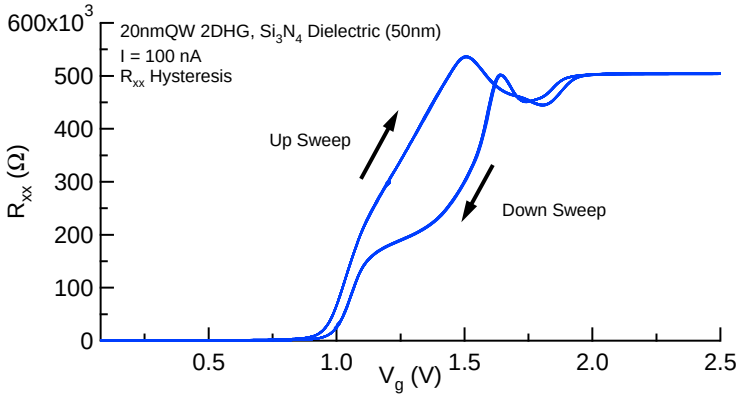

Figure 4.5: Example gate dependence curve for the 20nmQW 2DHG sample with the associated hysteresis.

found that the Si_3N_4 dielectric prevented any breakdown of the gate up to relatively high voltages, depending on the sample. In certain cases we were able to push out the carriers completely or increase the carrier density substantially.

The gate, acting similarly to a parallel plate capacitor, also has a charge and discharge time due to its RC circuit properties and a corresponding response time limit. There is also a respective cutoff frequency, F_c. Approximation for this system can be found using the equation

$$F_c = \frac{1}{2\pi RC} \tag{4.2}$$

where R is the resistance (mostly from the in-line 1 MΩ resistor) and C is the capacitance between the gate and the 2D sheet which can be found from

$$C = \frac{\varepsilon_o k A}{d}$$

where $\varepsilon_o k$ is from the dielectric constant ($k_{Si_3N_4} \approx 7$), A is the area ($1 \times 3\,\text{mm}$ for example), and d is the distance between the "plates" ($500\,\text{Å}$), yields a capacitance around $\sim 3.7 \times 10^{-9}\,\text{F}$ and a cutoff frequency of $\sim 42\,\text{Hz}$, which is well above modulation rate of $17\,\text{Hz}$.

4.5 Transmission measurement

For the microwave transmission measurement, we use the specially-designed probe with the power input and output dual coax lines across the sample (described in Section 3.4). The two arrangements, straight CPW and the meanderline CPW, have similar transmission line techniques that involve the MW power traveling across the 2D electron or hole gas. In the case of the straight CPW, the 2D gas lies between the center conductor and the ground plan of the CPW which provides an electric field from the microwaves in the plane of the 2D system and a magnetic field perpendicular to the 2D system. The meander line CPW is designed to irradiate the sample without a particular orientation for the electric and magnetic fields of the microwaves. The transmission measurement for both of these systems operates the same way, where the exiting power that has passed over the sample is fed up the probe to room temperature where a power sensor is connected to the coax line. The power sensor is connected to the MW frequency generator where the voltage provided by the sensor is then calibrated into a useful absolute power measurement in dBm. This power output (P_{out}) signal is fed into the modified data acquisition program through the GPIB

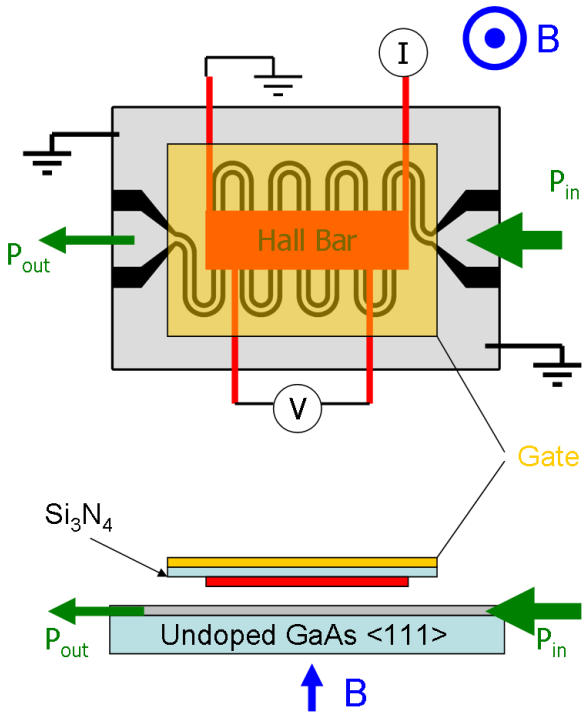

Figure 4.6: Geometry for simultaneous measurement of microwave transmission and gated magnetoresistance. Microwaves are irradiated from the backside of the sample, while the sample's carrier density is controlled by the top gate.

interface and plotted vs. the magnetic field. Using this arrangement, the transmission signal is acquired simultaneously as the magnetotransport data.

In the case of the straight CPW, there is little or no background signal due to the large amount of confinement of the MW between the center conductor of the CPW and the ground planes (see Figure 3.5). This means that the P_{out} transmitted through to the power detector is mostly from the 2D system which can be seen in Figure 5.12.

While the measurement setup is similar for the meanderline CPW, the difference is that it has been designed to irradiate the MW from its surface up through the back of a sample (Figure 4.6). The challenge of this technique is that the microwaves end up

coupling to metallic objects in the sample space which creates a very large background signal in the magnetic field (See Figure 4.7). While in certain cases the resonant signal we are looking for is still visible (around $0.03 \rightarrow 0.05\,\mathrm{dB}$ or $\sim 100\,\mathrm{nW}$), it is difficult to identify with certainty, especially due to the signal amplitude changing in time. This refers to the transmission values not the features. This makes it difficult/impossible to directly subtract a trace with the sample from one without a sample taken at two different times. To make this a valid measurement technique, we needed to develop something new.

To solve this problem, we used an idea similar to the single modulation technique and applied that to a differential power measurement technique, ΔP. To do this ΔP measurement, it requires that the sample has a gate across the 2D system and a way to irradiate the sample with continuous wave microwaves. The gate also needs to be able to push all carriers out of the sample for the background signal, and have them recover when the gate is turned off. Once it is established that gate can accomplish this through a gate dependence of the density (see Figure 5.20), we introduce a relay into the circuit that can switch the gate voltage on and off, thus pushing out the carriers and bringing them back. This acts the same as the modulated microwave power supply in Section 4.3, so

$$P_{out}(V_g1) = P_{out}(V_g2) + \Delta P \cdot (\frac{1}{2} + \frac{2}{\pi}[sin(x) + \frac{sin(3x)}{3} + \frac{sin(5x)}{5} + \ldots]) \qquad (4.3)$$

where V_g1 and V_g2 are the gate voltages that push out and bring back the carriers,

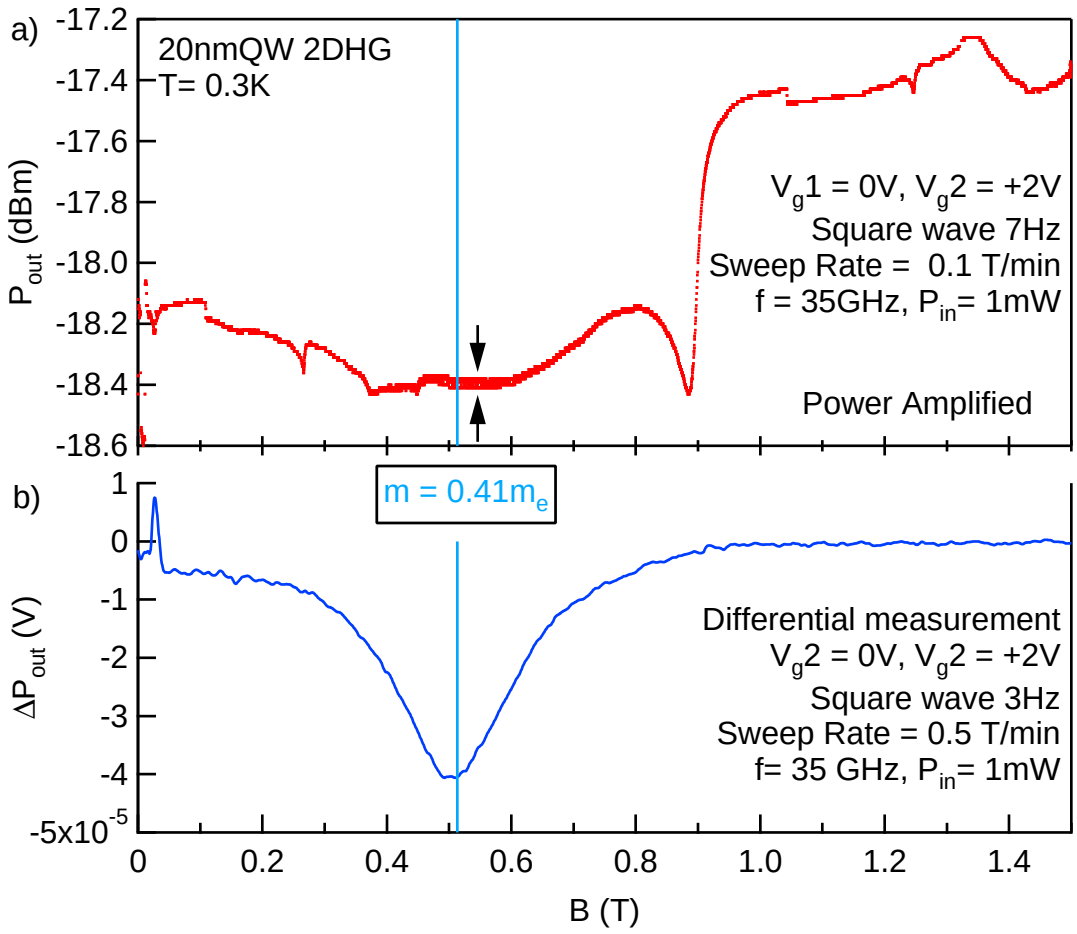

Figure 4.7: First results from the modulating the gate voltage. a) The top graph is the calibrated power output signal with a square wave modulated gate voltage between $0 \rightarrow +2\,\mathrm{V}$, created by irradiating with the meanderline. This signal includes both the background and the signal from the 2DHG that changes with the gate voltage. The separation is around $0.03 \rightarrow 0.05\,\mathrm{dB}$, or in this specific case 100 pW when taking into account the power amplifier. The gate voltages were chosen so as to push out all the carriers $(+2V)$ and bring them back $(0V)$. b) The voltage output from the power sensor fed into a lock-in locked to the same frequency as the gate modulation, which yields a strong peak that matches up closely with the cyclotron resonance associated with a hole effective mass of $\sim 0.41 m_e$.

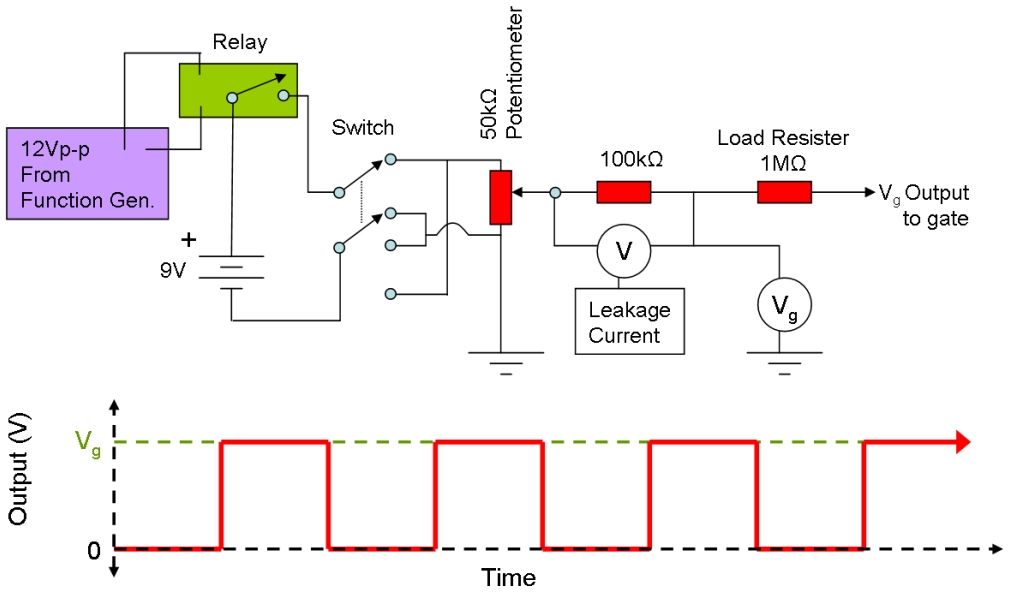

Figure 4.8: Gate box circuit diagram with the addition of a relay that is driven by a function generator, preserving the gate box circuit and the cleanliness of the output signal.

respectively, adapted from Equation 4.1.

The relay is powered by a function generator providing a $12\,V_{p-p}$ signal at 17 Hz. Driving the gate directly with a square wave function generator provided too much noise and voltage spikes to the gate which would cause it to break down. Instead, by using a relay in line with the gate box arrangement, we are able to use the same stable voltage provided from the batteries. In addition to the 17 Hz function generator powering the relay, the TTL output signal triggers a lock-in where the voltage signal from the power detector (Pins 1 and 2) is directly plugged into A of the lock-in. While this arrangement allows for the triggering of the power detector signal, it does not allow for a calibrated dBm measurement. To solve that problem, a separate triggerable power detector is needed, which once integrated into the acquisition software

and tuned to the system, would output a dBm measurement. The triggered voltage output from the power sensor, which is linear with respect to the input power, shows us the differential signal ($\Delta P = P_{out}(V_g1) - P_{out}(V_g2)$). The disadvantage to not having a the dBm absolute power signal is that we cannot convert the transmission signal into an absorption signal and use the Drude conductivity formula (Equation 5.7) to fit the peak to obtain the effective mass multiplier and the cyclotron time constant for the sample. This means we have to calculate these values using the methods in Sections 5.4 and 5.5. When taking the power amplifier into account, this measurement technique's sensitivity is on the order of $100\,\mathrm{pW}(40\,\mu\mathrm{V})$ from the results in Figure 4.7a(b) with a modest input power of $1\,\mathrm{mW}$, which results in a resolution around $0.1\,\mathrm{ppm}$. Much smaller features can still be resolved with input powers lower then $0.01\,\mathrm{mW}$.

If we connect the outputs of two gate boxes, V_g1 (with a relay) and V_g2, we adjust both voltages separately to push out the carriers and maximize the carrier density (see Figure 4.9). To check on the final output voltage, connecting it to an oscilloscope is helpful.

From the HJ data, we realized that there was a phase correction that was needed in order to compensate for the imaginary component of the signal, due to the capacitance between the 2DEG, the gate, and the coax lines. We found this correction was around -50^o, but varied depending on the sample. Once this was corrected for, it minimized the R_y and strengthened the R_x component of the ΔP signal.

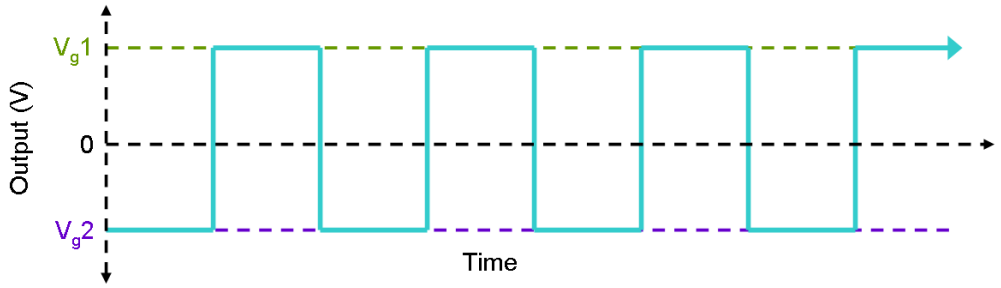

Figure 4.9: Output using two gateboxes (one with a relay) in parallel, allows for free adjustment of both V_g1 and V_g2.

We were also able to measure the gate voltage dependence on the transmission signal with a slight modification to the way we took the ΔP measurement. To do this, we changed the voltage spread ($V_g1 \rightarrow V_g2$) of the square wave voltage we were applying to the gate. Keeping the voltage applied to drive out the carriers constant at V_g2, we could then adjust the carrier density using V_g1. This meant that by keeping the expulsion voltage constant to provide a background transmission signal, we were able to observe the effects of different carrier densities on the transmission peak location and line width (see Figure 4.9). This process requires two gate boxes wired in parallel, where one applies the DC negative voltage while the other supplies the positive voltage square wave. Keeping V_g2 high enough to push out the carriers for an adequate background subtraction, we can set V_g1 at whatever level we like. By changing that second bias we can consider that to be taking a gate dependence, which will be discussed further in Section 5.4.1.

Chapter 5

Experimental Results

5.1 Microwave Irradiation of a 2D system

When irradiating a high mobility 2DEG sample with microwaves, we immediately see a response in R_{xx} at low magnetic fields ($< 0.5\,\mathrm{T}$). These oscillation peaks occur at

$$\epsilon = \frac{\omega_{MW}}{\omega_c} = \frac{2\pi \cdot f \cdot m^*}{e \cdot B} \tag{5.1}$$

and are periodic in $1/B$. From Figure 5.1 we see that these features, depending on the mobility, are very visible and stand out in the region of the magnetic field below the onset of the SdH oscillations. This microwave-induced resistance oscillation (MIRO) and the SdH signals coexist simultaneously and, since the MIRO peaks are microwave frequency dependent, there is a probability that at higher frequency the MIRO signal will overlap with the SdH signal, as in Figure 2.3. The difference of course being the origin of the signals, which also means that they have drastically different amplitude temperature dependences where MIRO as $\frac{1}{T^2}$ while SdH is exponentially damped [11, 26]. By observation, we notice that in the temperature dependence the onset of the SdH migrates further and further into higher magnetic fields. The MIRO amplitude, on the other hand, decreases at $\frac{1}{T^2}$, much slower and is still visible, although faint, up to $\sim 20\,\mathrm{K}$. In the situation of very high microwave irradiation frequency there is

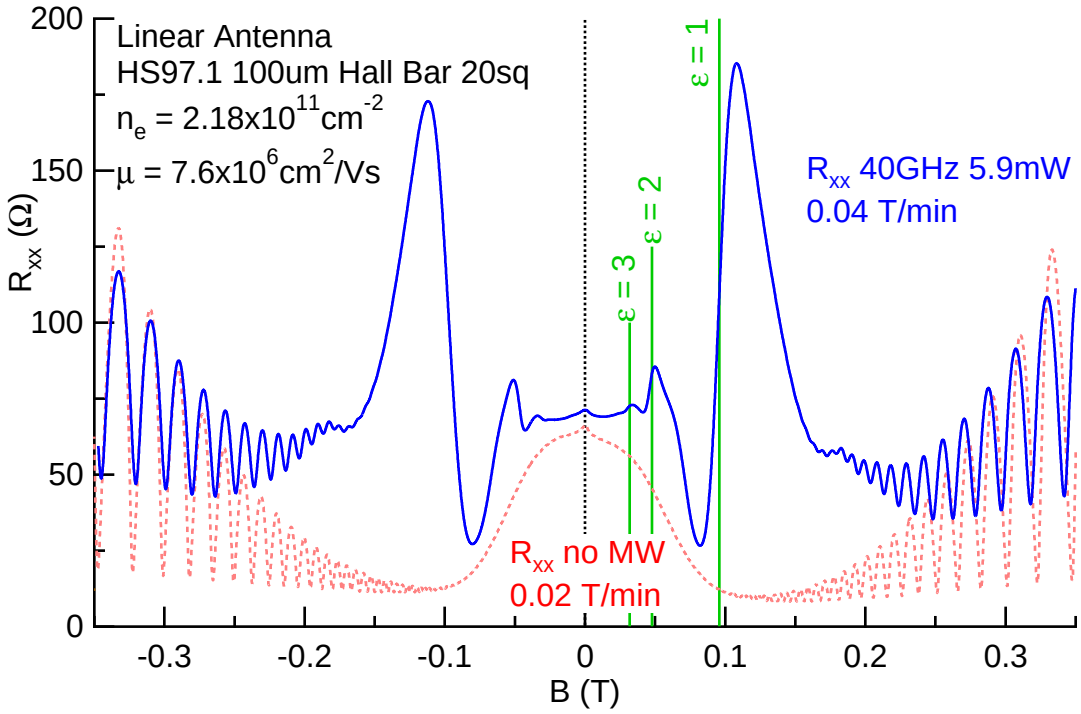

Figure 5.1: Comparison of R_{xx} signal with and without microwave irradiation. The integer ϵ values have been highlighted by the vertical lines.

still a possibility of overlapping with the SdH, but this can be avoided by increasing the temperature of the system slightly.

The results obtained using the waveguide probe and Gunn diodes open up a much greater range of microwave frequencies, $26.5 - 150$ GHz at which we can irradiate the sample. As expected from the Equation 5.1, the frequency dependence of MIRO is very linear, which can be observed by Zudov et al. [23]. We also note that using higher frequencies push the $\epsilon = 1$ peak further out into higher magnetic fields and allows for higher orders of ϵ at lower fields. Depending on the sample mobility and the frequency of irradiation, we can see up to $\epsilon = 7$ (as seen in Figure 5.8a) from this irradiation technique. In previous research, higher orders up to $\epsilon = 20$ have been

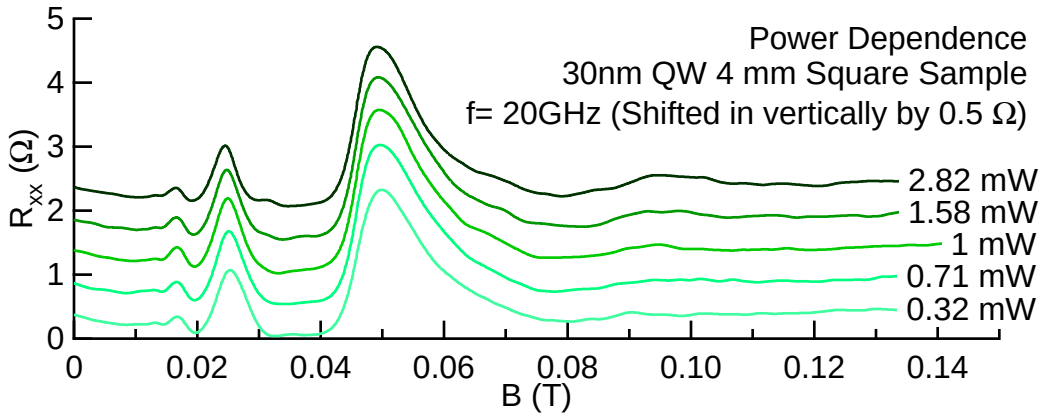

Figure 5.2: Zero resistance states when irradiated by a Dipole antenna.

seen [23]. Using the coax-based probe with a frequency range of $2 - 40\,\text{GHz}$ we also are able to see this same frequency dependence using a linear and dipole antenna (see Figure 3.4). However, due to the lower irradiation frequencies, the only higher order MIRO $\epsilon = 2$ is visible. In both irradiation geometries, zero resistance states (ZRS) are visible depending on the right conditions, high mobility, and high enough power directed microwave irradiation, as seen in figure 5.2.

In addition to this, we also wanted to confirm that we were capable of irradiating the sample with microwaves using the straight CPW. To do this, we took a frequency dependence plot in R_{xx} (see Figure 5.3). From these results we can see the expected direct proportionality of ϵ to the irradiation frequency of the MIRO signal.

Although the coax based probe is only able to observe low order MIRO peaks due to a lower frequency range, it sets up the ability to look into Fractional Microwave Induced Resistance Oscillations (FMIRO). The lowest order of FMIRO, $\epsilon = \frac{1}{2}$, has been observed early on after the discovery of MIRO [31, 42]. Unfortunately, those

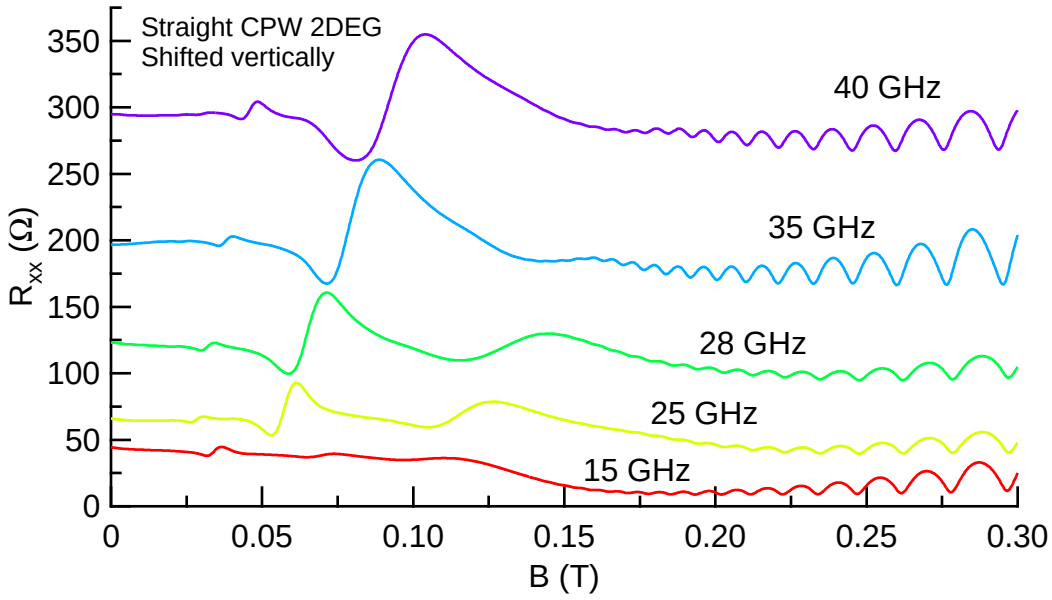

Figure 5.3: Frequency dependence of R_{xx} from the straight CPW 2DEG sample.

early setups were using higher frequencies and, while the FMIRO signal was there, it was much smaller then the SdH signal that occupied the same region of the magnetic field. Our coax based probe was able to take advantage of its lower frequency range and ability to focus the microwaves power directly on the sample in order to be able to observe higher orders of FMIRO, in some cases up to $\epsilon = \frac{1}{5}$.

Our earliest known plot of FMIRO was actually a complete accident and occurred when, for a different reason entirely, the high mobility sample was mounted directly on top of a piece of copper on a chip carrier with a coax line linear antenna positioned $\sim 1\,\text{mm}$ above the sample. This geometry was able to expose the sample to a blanket of microwaves which were then reflected from the electrically floated copper plate. This, potentially through constructive interference, increased the microwave power at

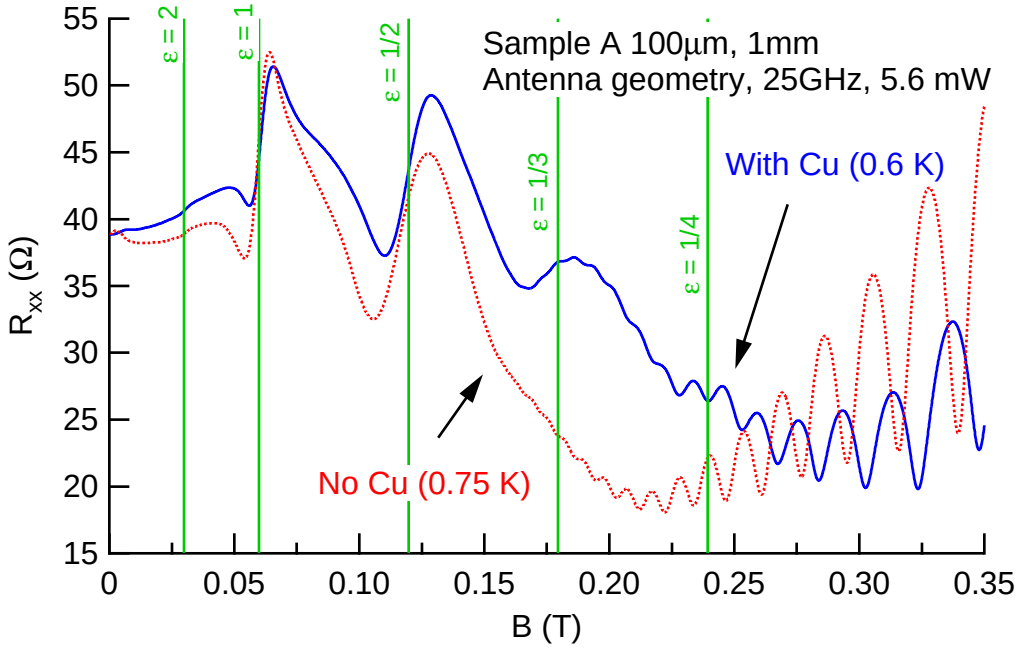

Figure 5.4: First strongly visible FMIRO signal.

the region of the 2DEG, yielding FMIRO (Figure 5.4). From this result, we focused on optimizing a geometry that would focus the microwave power directly across the 2DEG using a CPW (Section 3.4).

These FMIRO peaks behave similarly in their frequency dependence as MIRO. In fact, when plotting the location of the ϵ peaks in the magnetic field, we note how linear they are in Figure 5.6. This confirms that the physics behind FMIRO is indeed the same as MIRO and Equation 5.1 applies, except now there is an inverse integer ratio.

The frequency range focused on with the straight CPW sample was $14.9-40\,\mathrm{GHz}$, closer to the $\omega_C\tau_{S,0} < 1$ classical regime. In the classical regime there is still a lot of LL overlapping which allows us to make the approximation that the classic elastic

electron point particle Drude conductivity model applies. This also allows us to avoid overlapping the MIRO and FMIRO signal with that of the SdH signal which is important due to the respectively small FMIRO amplitudes. The crossover range,

$$\omega_C \tau_S = 1 \tag{5.2}$$

is represented in our R_{xx} vs. B data (Figure 5.5) by the onset of SdH at $0.26\,\mathrm{T}$ without MW. Using this onset magnetic field, the quantum scattering time was calculated to be $\tau_S = 0.95\,\mathrm{ps}$, and the transport relaxation time at $B = 0\,\mathrm{T}$ to be

$$\tau_{tr} = \frac{\mu m^*}{e} = 450\,\mathrm{ps} \tag{5.3}$$

where $m^* = 0.067 \cdot m_e$. We then compare this with the long range disorder limit of $\tau_{tr}/\tau_S \gg 1$ and find that we fulfill that requirement since $\tau_{tr}/\tau_S \approx 473$. From Dmitriev et al we also check the limit of separated LL where $\omega_c \gg 2\Gamma = 2\sqrt{\frac{2\omega_c}{\pi\tau_S}} \rightarrow \omega_c\tau_S \gg 1/\pi$. To do this, we look at the position of the transmission minima in Figure 5.12 ($B = 0.058\,\mathrm{T}$) at $22.1\,\mathrm{GHz}$ and calculate $\omega_c = 1.52 \times 10^{11}\,\mathrm{s}^{-1}$, which yields $\omega_c\tau_S = 0.14$. This places our system near the classical limit ($\omega_C\tau_S \rightarrow 0$) and below the crossover range of $\omega_C\tau_S = 1$ where the LLs are still connected corresponding to the theory presented by Dmitriev et al. [28]

From the straight CPW sample we can pick out both the MIRO and FMIRO ranging from $\epsilon = 2, 1, \frac{1}{2}, \frac{1}{3}, \frac{1}{4}$ and, at certain frequencies $\frac{1}{5}$, confirming previous research

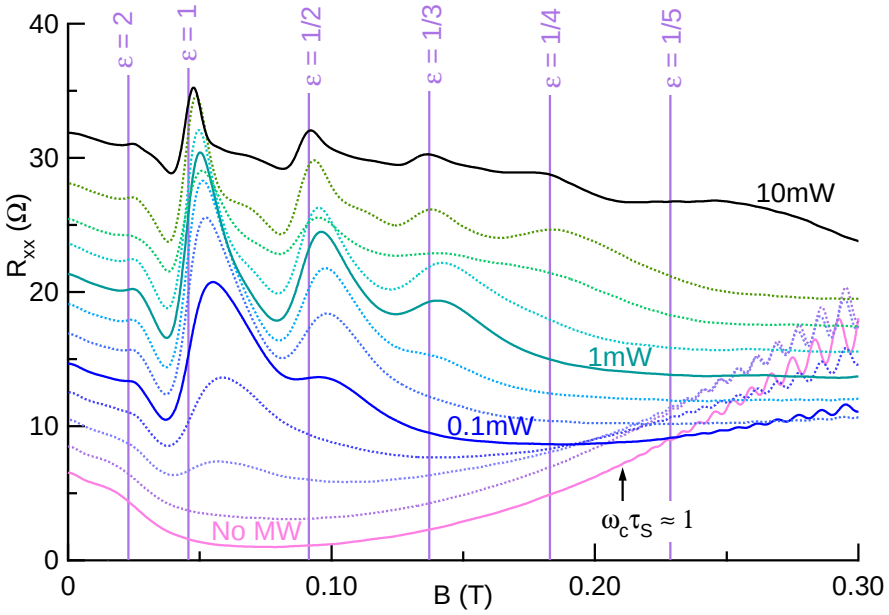

Figure 5.5: Power dependence of R_{xx} for 19.1 GHz from $0 - 10$ mW where 0.1 mW, 1 mW, and 10 mW have been highlighted in increasing order. The saturation of MIRO occurs around 0.56 mW input power. All data was shifted vertically for clarity.

[42, 43], which can be seen in Figure 5.5. The data in the FMIRO sub-harmonic regime mirror that in the harmonics regime (Figure 5.6a) where the DC resistance oscillation does not correspond to an electron transition that requires the absorption of energy carried by MW photons. In Figure 5.6b, we plotted out the slopes of the frequency dependences vs. ϵ and found that both MIRO and FMIRO were linear, confirming that we are observing FMIRO and that it is closely tied to MIRO.

The power dependence in R_{xx} at 19.1 GHz from Figure 5.5 allows us to see the onset of the MIRO and FMIRO. From this data we can identify where the $\epsilon = 1$ peak arises at input powers of ~ 0.003 mW and saturates at ~ 0.562 mW. Then the amplitude linearly decreases, potentially due to MW heating effects. While the amplitudes differ, both MIRO and FMIRO behave similarly.

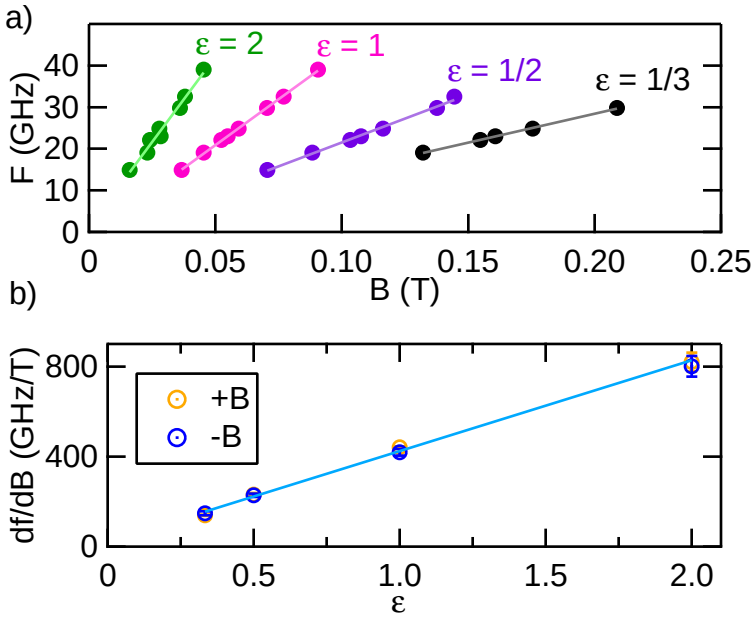

Figure 5.6: a) Plot of the measured ϵ values with fitted lines taken from the $+B$ field in Figure 3; b) Slope of the fitted lines in a) plotted versus their respective ϵ values. The error bars are a single standard deviation.

In Figure 5.7 there are two contrasting theories as to the origin of FMIRO: a multiphoton process [31] and a resonant sideband [44]. Each theory currently can explain parts of the FMIRO signal, but cannot explain higher orders yet. The multiphoton process is able to scale many variations of ratios of photon energy and LL energy, and requires high MW irradiation powers. Comparably, we would also assume that the probability of these multiphoton transmissions would drop exponentially at higher orders, but we are still able to see them up to $\epsilon = 1/5$ and in some cases up to much higher orders [42]. This leads us to believe that there is potentially more to this theory.

The resonant sideband theory proposed by Dmitriev suggests that a single photon

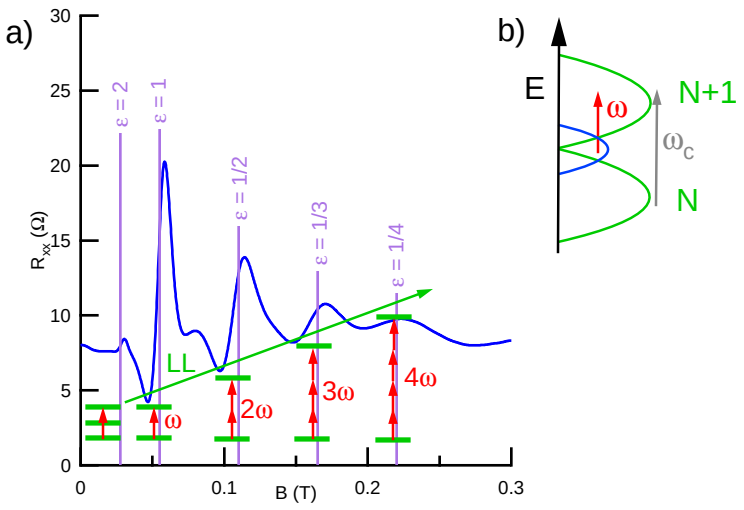

Figure 5.7: a) Multiphoton photon process. b) Resonant sideband process.

transition is occurring. However, instead of it being from one LL to the next, it is from a resonant sideband that arises between closely spaced LLs. The resonant sideband arises due to interference between overlapping LL. The resonant sideband theory allows for two signal photon transitions to the sideband and again to the next LL. While $\epsilon = \frac{1}{2}$ can be understood using this method, it is much more complicated to scale it up to higher orders. A complete discussion of the comparison between these theories can be found in the paper of Hatke et al. [43] which reveals that there is still a probability for transition between the LL at much lower energies than expected. They identified this by applying up to $40\,\mu$A of current through the sample which tilts the LLs enough in momentum space to facilitate the transition.

5.2 Edge Magnetoplasmon

The edge magnetoplasmon oscillations (EMPO) were measured using the waveguide probe at irradiation frequencies of $27 - 130\,\mathrm{GHz}$ over a very high mobility 2DEG (HS97.1). Our specimens for this experiment are Hall bars defined by lithography and wet-etching from a $GaAs/Al_{0.3}Ga_{0.7}As$ heterostructure grown by molecular-beam-epitaxy. Sample A has a Hall bar width (W) of $100\,\mu$m and has two sections of 1 and 2 mm (L) that make up 10 and 20 square sections respectively. The contact leads have the same width of $100\,\mu$m. Sample B has a similar geometry but with a width (both bar and leads) of $200\,\mu$m, giving the 1 and 2 mm sections 5 and 10 squares respectively. High quality ohmic contacts to the 2DEG were made by high temperature diffusion of indium. After a brief illumination with visible light, at $T = 0.3\,\mathrm{K}$ the sample A (B) attained a sheet density $n_s \approx 2.27 \times 10^{11}\,\mathrm{cm}^{-2}$ ($2.45 \times 10^{11}\,\mathrm{cm}^{-2}$) and a mobility $\mu \approx 8.3 \times 10^{6}\,\mathrm{cm}^2/\mathrm{Vs}$ ($11 \times 10^{6}\,\mathrm{cm}^2/\mathrm{Vs}$). The microwaves (MW) were generated by a set of Gunn diodes and sent via a rectangular waveguide (WG-28) to the sample immersed in the ^3He coolant. The mutual orientations of the waveguide, 2DEG plane, and the magnetic field corresponded to the Faraday configuration. For MW frequencies $f < 44\,\mathrm{GHz}$, the waveguide operated in single-mode and the $\vec{E}$ polarization of the MW was perpendicular to the Hall bar direction.

For this experiment we compared both the ΔR single modulation and photovoltage techniques and concluded that they yielded the same results (see Figure 5.8c). Due to the ease of the photovoltage measurement (floating all but one grounded contact,

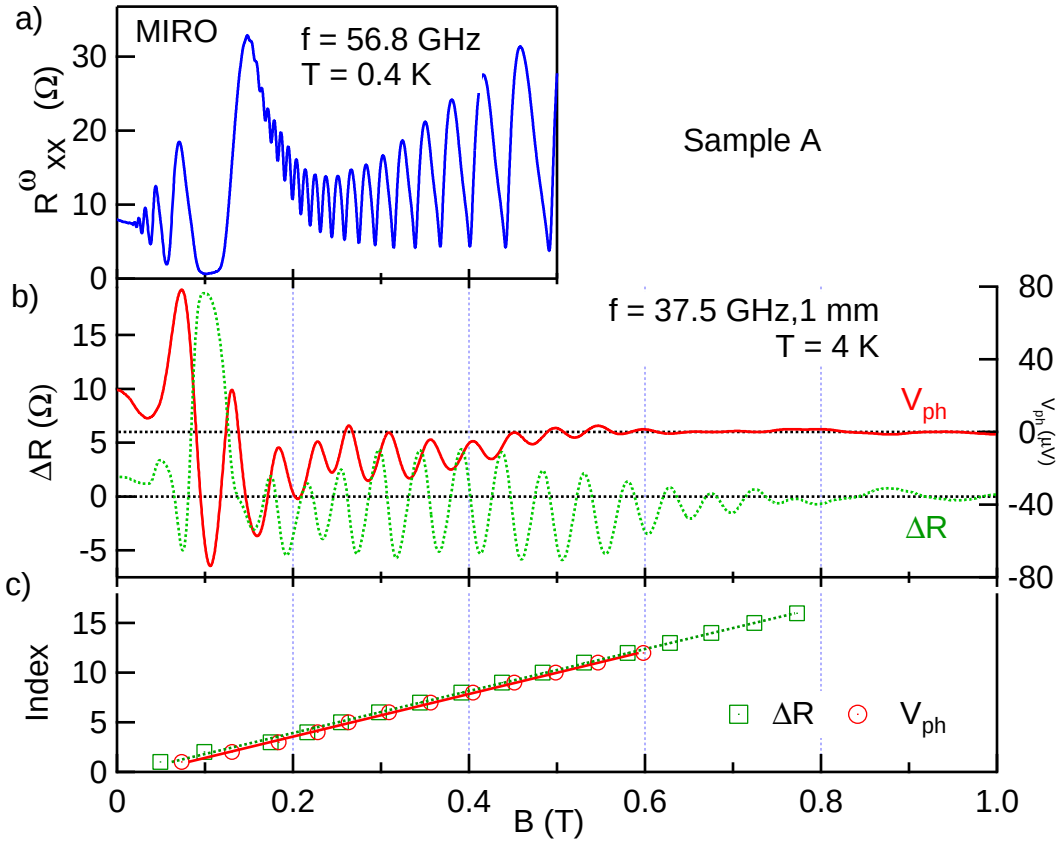

Figure 5.8: a) Typical low temperature ($T = 0.4\,\mathrm{K}$) photoresistance data showing microwave-induced resistance oscillations and the corresponding zero-resistance state; b) Differential photoresistance (ΔR) and photovoltage (V_{ph}) were measured simultaneously at 37.5 GHz irradiation along the 1 mm section of sample A, at $T = 4\,\mathrm{K}$. B-periodic oscillations are clearly observed at $B > 0.2\,\mathrm{T}$; at lower magnetic fields MIRO also contributes to the signal. c) Plot of the field position of oscillation maxima vs. their index. Linear fits give a slope of $21.16\,{}^{1}/_{\mathrm{T}}$ and $21.47\,{}^{1}/_{\mathrm{T}}$ for ΔR and V_{ph}, respectively.

and irradiating the 2DEG with microwaves while measuring the change in R_{xx}), we primarily used it to measure the frequency dependence of each sample. From each frequency we observed a periodic oscillation (ΔB) in the photovoltage which we compared to the proportionality

$$\Delta B \propto \frac{n_s}{\omega_{MW} \cdot L} \tag{5.4}$$

that was proposed in Kukushkin et. al. [14]. To do this, we found that the period of oscillation was inversely proportional to the frequency (see Figure 5.9). From Figure 5.10a, we also were able to find ΔB to be inversely proportional to the frequency. To check the next component of this equation we could qualitatively compare both the electron density for Sample A and B since they had different electron densities. We found that their respective densities qualitatively fit into this equation. However, since there are only two densities, we would need to control the electron density using a gate to have more data points to establish the density dependence (See Figure 5.10b). Lastly, we compared the dependence of L, or the length between the leads, which was previously described by Kukushkin et al. [14] to be how the propagating EMP interferes with next lead. To do this, we compared the photovoltage from the 1 mm and 2 mm sections of our Hall bars. We found that they yielded the same results just 180^o out of phase with each other, which we attribute to the Hall bars location in the gradient of the electric field from the waveguide.

The previous explanation of the EMPO involved interference between the prop-

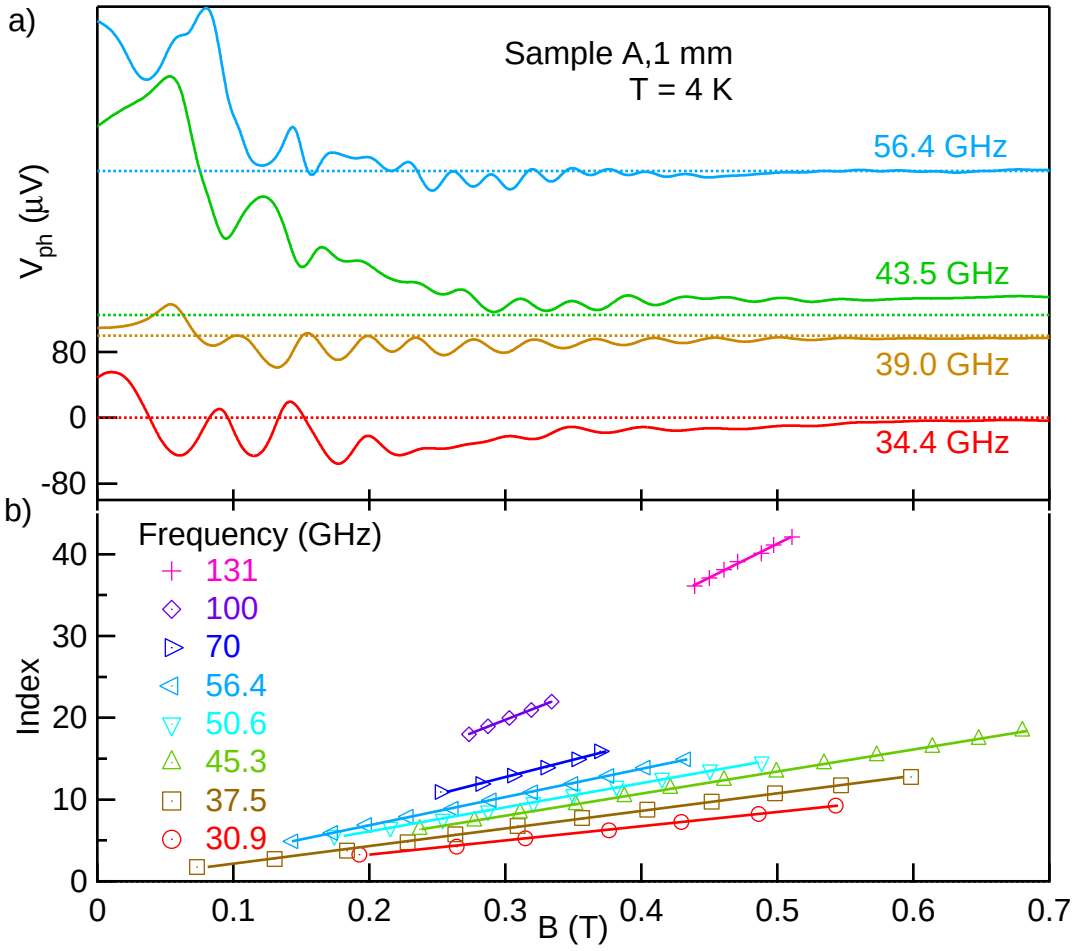

Figure 5.9: a) Examples for photovoltage signal, V_{ph}, as a function of the magnetic field, B, for selected microwave frequencies. b) Linear fits to B positions of the V_{ph} peaks show that the oscillations are periodic in B; from the slope of the fitting line, the oscillation period, ΔB, is determined.

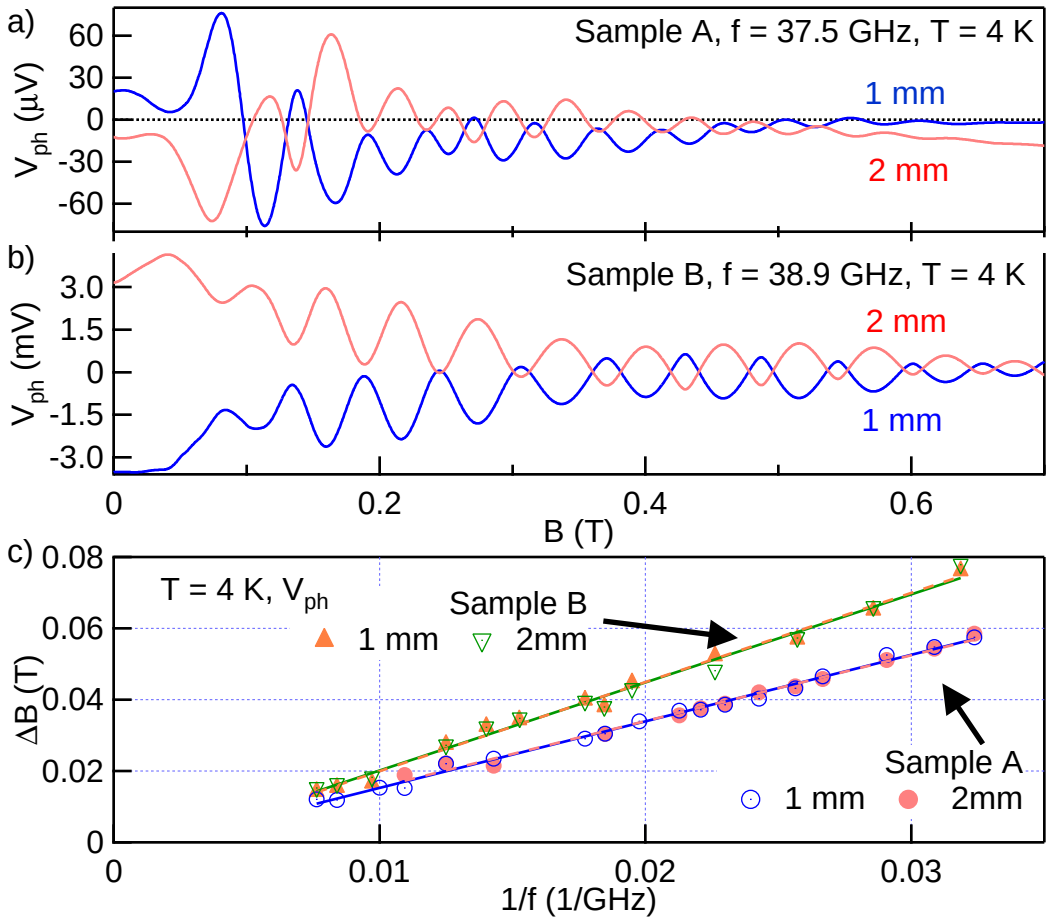

Figure 5.10: a) Example traces of photovoltages $V_{ph}(1,2)$ (measured in the 2 mm section) and $V_{ph}(2,3)$ (1 mm section) in sample A, at a microwave frequency 37.5 GHz. The V_{ph} oscillations from the two sections have approximately the same magnitude but with opposite signs. b) Examples of similar data from sample B at 38.9 GHz. c) The plot of ΔB vs. inverse microwave frequency $1/f$ shows a linear relation; the data from 1 mm and 2 mm sections from the same sample collapse on the same line, indicating that the ΔB is independent of contacts in a wide frequency range. From the plot of ΔB vs $1/f$, slopes of 1.85 $T \cdot GHz$ and 2.50 $T \cdot GHz$ are determined for samples A and B, respectively.

agating edge states that would propagate from charge oscillations excited by microwaves in the leads. However, due to the external magnetic field we assume that there is a chirality of the propagation along the edges of the sample. Taking this into account, there can be no direct way that the edge propagation states would interfere with one another between the leads where the measurement is taking place. Instead this suggests that it is a non-local effect that travels around the edges of the entire sample.

In the temperature dependence from Figure 5.11a, we found that lower temperatures actually made it more difficult to see the EMPO due to the strong SdH and MIRO signals. As the bath temperature increased, the SdH oscillations receded into higher magnetic fields and the MIRO signal amplitude decreased sufficiently to be able to see the EMPO. The inset to Figure 5.11b shows the exponential drop in amplitude of the EMPO features, however there is no temperature dependence on the period of oscillation, ΔB. Conveniently, taking data at 4 K was high enough to drown out the SdH and MIRO in the region where we would expect to see EMPO ($0.2 - 0.8$ T). This meant that we did not need to condense the liquid ^3He and could simply use it as an exchange gas to equilibriate the temperature in the sample space with that of the ^4He main bath. The fact that the temperature dependence is different than both MIRO and SdH leads us to believe that all three of these features are uncorrelated.

This experiment yielded new insight into the propagation of EMPO due to microwave irradiation and shed light on the proportionality of the period of oscillation

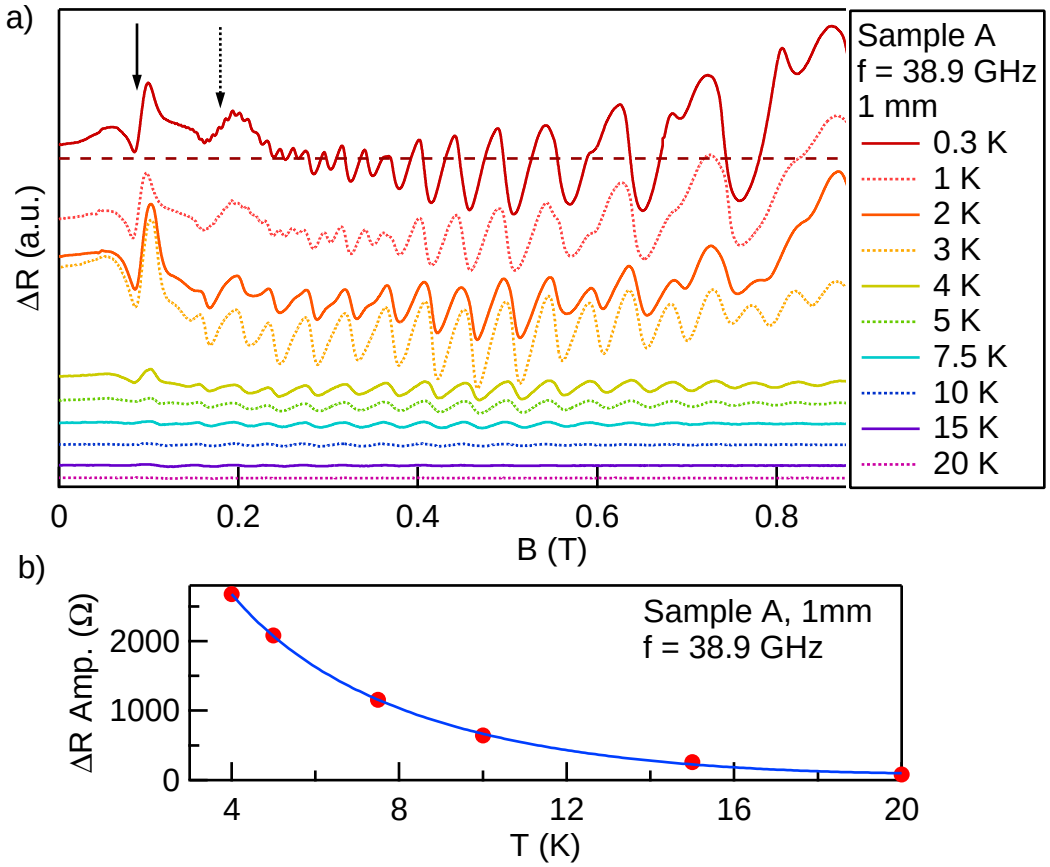

Figure 5.11: Temperature dependence of the photoresistance, ΔR, for sample A at a microwave frequency 38.9 GHz. The arrows mark the microwave-induced resistance oscillations (MIRO), the dotted arrow marks the $\epsilon = \frac{1}{2}$ peak. At low temperature, $T < 2\,\mathrm{K}$, the ΔR is dominated by $1/B$ oscillation (MIRO and SdH) and at higher temperatures, $T < 4\,\mathrm{K}$, by B-periodic oscillations. b) Peak to peak amplitude of an EMPO in temperature, below 4 K the signal was affected by SdH.

of the EMPO.

5.3 Microwave Transmission in a 2D system

The main benefit of the research done with the coax-line based probe is that it allows for measurements that were previously very difficult, such as being able to measure the microwave transmission across a sample. One of the methods for measuring transmission/absorption was previously done using bolometers and microwave resonant cavities [11], where microwaves had to be irradiated through or reflected from the 2DEG or 2DHG. One of the complications with this is that gates could not be introduced to the system to control the carrier density. We introduce two methods utilizing our coax geometry to irradiate a sample by non-Faraday, CPW geometries, and Faraday, meander line geometries. These new methods allow us to also simultaneously measure the gated magnetotransport of the sample.

5.3.1 Straight CPW

Using the straight CPW sample, we were able to constrain the E^{ω} and H^{ω} of the microwaves to minimize stray irradiation. In this case we were able to irradiate the sample in a non-Faraday geometry, where the E^{ω} was in the plane of the 2DEG and the H^{ω} was perpendicular (as seen in Figure 5.12c). Another advantage of this geometry is that the microwave signal can be transmitted across the sample and the power output, P_{out}, could be measured, which would become the basis for the following

experiments. To have this control, the CPW was evaporated using photolithography techniques on top of the 2DEG separated by a dielectric of either Al_2O_3 or Si_3N_4. When both sides of the CPW from the sample were connected to the that of the CPW sample holder, it made a complete circuit (Figure 3.5). From the designs of the probe, the second coax line was then attached to a microwave power detector which is incorporated in the microwave frequency generator. By modifying the data acquisition program, we were able to acquire the output power simultaneously along with the magnetoresistance. The power sensor itself has a range from $-40 \rightarrow +20\,\mathrm{dBm}$ and a sensitivity of $\pm 0.01\,\mathrm{dBm}$. Due to the low waste irradiation of microwaves of this geometry, there was very little background signal other than what was coming from the 2DEG.

From our straight CPW data, see Figure 5.12, we immediately see that there is relationship between the transmission vs. resistance data in the integer MIRO, where there is a clear transmission minimum associated with the fundamental CR ($\epsilon = 1$) and a slight response at $\epsilon = 2$. These transmission features are more apparent in the dP_{out}/dB data of Figure 5.12b. A transition minimum at $\epsilon = 1$ is expected due to the MW irradiation resonating with the CR frequency where the MW energy equals the LL spacing, where the irradiation energy will be absorbed by the electrons. From Figure 5.12 we also note that there are no transmission features associated with FMIRO, even with higher microwave irradiation powers.

To explain the response at $\epsilon = 2$, we propose the signal originates from LL mixing

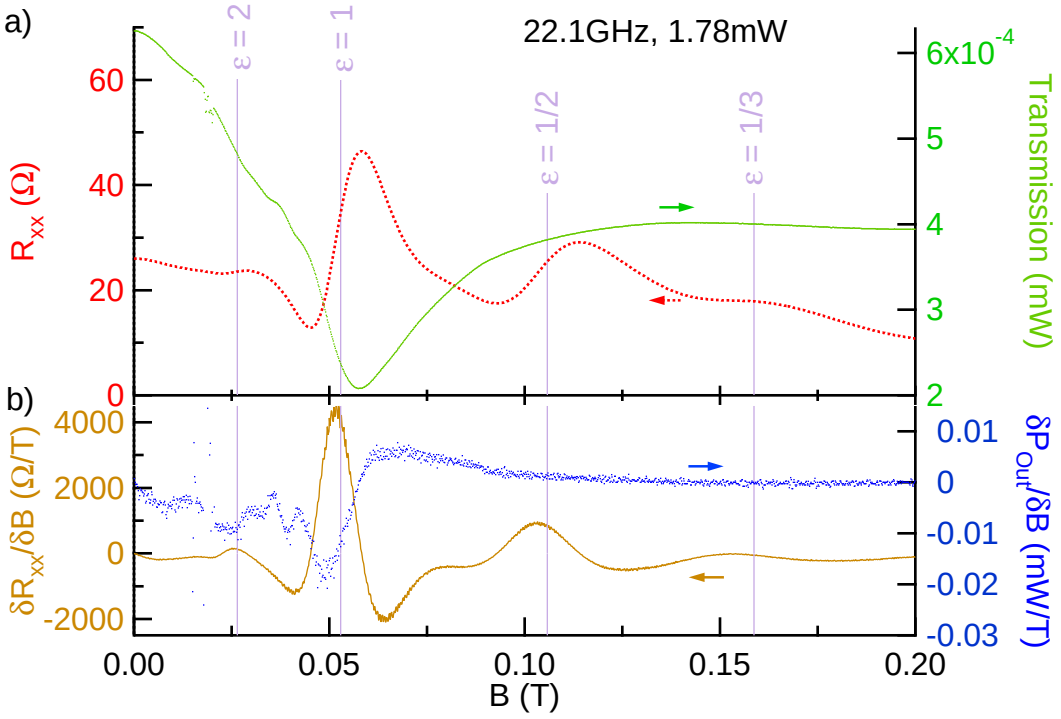

Figure 5.12: a) Plot of R_{xx} magnetotransport, microwave transmission vs. magnetic field at 2.7 K when 22.1 GHz microwaves are applied at 1.78 mW, the transmission signal has been averaged over 10 sweeps. b) Derivative of a) with respect to the magnetic field.

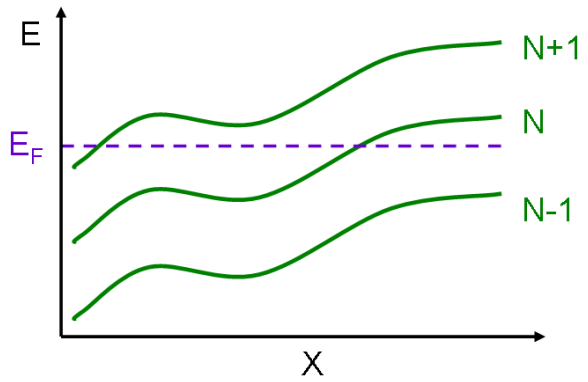

Figure 5.13: Spatially dependent Landau level mixing between adjacent levels.

[21, 45] caused by localized impurities in the 2DEG. Spatially this means that the relationship between the Fermi energy and the LL will vary, which, when averaged over the 2DEG from contact to contact, means there will be a possibility that the LL transition from N to N+1 wavefunction has components of the next LL (N+2). In this way it is possible to have a large fundamental CR transmission signal and observe an effect at $\epsilon = 2$, which can be observed due to the sensitivity of the measurement or the impurity structure of the sample. Theoretically this signal is expected to be 1000 times weaker than the fundamental CR signal [44] at $\epsilon = 1$. Since the $\epsilon = 2$ feature is visible even at lower powers, these preliminary results could lead to a way to measure this transitional mechanism.

5.3.2 Meanderline CPW

In contrast to the straight CPW measurement, we also created a CPW meander line geometry which we assume would have a blanket radiation pattern. This geometry

uses a similar technique for creating the meander line as with the CPW, but instead of it being evaporated on top of the sample directly, it has been evaporated (using photolithography) onto an undoped wafer of $GaAs < 111 >$. Then it was set into a block and connected to the coax/CPW the same way as the straight CPW. However, unlike the straight CPW geometry where each brass block had to be wired up and custom fitted for each sample, this design allows for quick exchange of polished back side samples. The meander line geometry acts as an antenna to propagate microwaves in a Faraday geometry, where the microwave E^{ω} and H^{ω} fields are both in the plane of the 2DEG (see Figure 3.7). Unlike the straight CPW arrangement, there is no copper back side underneath the meander line, so the microwaves are not constrained in the $GaAs$ wafer and can instead propagate away through a sample placed on top.

We estimate that the electric field irradiated from the meander line to be $\sim 20\,{}^{\mathrm{V}}/_{\mathrm{cm}}$, assuming an equal distribution of power in a semisphere of radium 1 mm at the location of the meanderline. Initially we used the same brass sample holder from the previous CPW measurements; however, since this meander line is designed to irradiate microwaves and not keep them confined in the CPW, we found that the microwaves irradiated were resonating with the dimensions (0.5×0.6 in) of the brass sample holder and yielding very large resonance absorption signals around 25 GHz. To avoid this strong background signal, which was much larger than the signal we were trying to measure from the 2DEG, the sample holder needed to be redesigned using Stycast 2850FT with trace amounts of graphite to absorb the microwaves (see Ap-

pendix B). After this modification, the transmitted microwave signal became much clearer. While there were still background features, they were minimized and occurred at higher magnetic fields (which can be seen in Figure 4.7a). In addition to the background signal, we also noticed that the transmission signal would drift over time. This drift would not affect the features but it made it impossible to subtract a separate background signal later during data analysis. To get usable data from the transmission signal, we needed a way to subtract this background signal from the measurement instantaneously. This was accomplished by using a gate over the 2D system that could push out the carriers and bring them back. In this way we set up a differential measurement technique to measure

$$\Delta P = P_{out}(V_g) - P_{out}(V_g = 0) \tag{5.5}$$

(described in Section 4.5), which is similar to the ΔR measurement from Section 4.3. Using this method, we were successful at isolating the 2D system and subtracting the background.

From these results we see a peak associated with the cyclotron resonance of the system (2DEG or 2DHG) whose location we can explain from the equation $\epsilon = 1 = \frac{eB}{2\pi f \cdot m^*}$, where B is the location in the magnetic field of the transmission minima. We were able to measure the frequency dependence of this peak, see Figure 5.19. Due to the probe, the transmission of power is frequency dependent, which is why some frequencies have slightly different features (such as minima, or steep rises/falls) at

$\epsilon = 1$.

5.4 Effective Mass Measurement

One of the results we could gather from the gate modulation technique we developed was the effective mass measurement. Using the location in the magnetic field of the transmission minima (B) and

$$m = eB/2\pi f m_e \tag{5.6}$$

we were able to calculate the effective mass multiplier m (from $m^* = m \cdot m_e$, where m^* is the total effective mass and $m_e = 9.109 \times 10^{-31}$ Kg the mass of an electron). In addition to this method, assuming the transmission data is available to convert to a normalized absorption signal, the Drude conductivity model [46] can be used as the fit:

$$\frac{Re\{\sigma_{xx}\}}{\sigma_0} = \frac{1 + (\omega_C \tau_s)^2 + (\omega \tau_s)^2}{[1 + (\omega_C \tau_s)^2 - (\omega \tau_s)^2]^2 + 4(\omega \tau_s)^2} \tag{5.7}$$

where σ_0 is the conductivity at $B = 0\,\mathrm{T}$ and τ_s is the cyclotron relaxation time.

In the case of the straight CPW 2DEG sample, we had an absolute power transmission to work with. From the power output signal in dBm which we converted to mW and then normalized to the input power, we could then use the approximation of

$$Absorption \approx 1 - Transmission \tag{5.8}$$

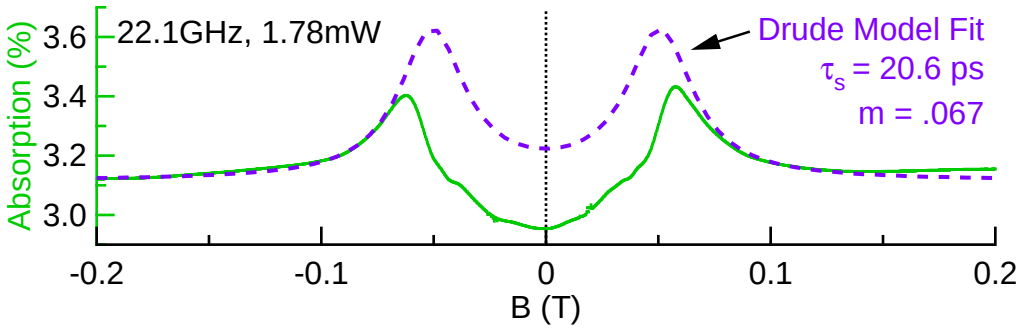

Figure 5.14: Drude conductivity fit for the straight CPW P_{out} signal that has been converted into an approximate normalized absorption. Although the results from this fit are slightly different than expected, it does give us an approximation for the cyclotron time constant.

where the reflection component was assumed to be negligible. With the "absorption" signal we were able to fit to the Drude conductivity model, which resulted in measuring the effective mass multiplier (from the component in Equation 2.17). The values we obtained from this method for the effective mass multiplier were identical to using the location in the magnetic field of the transmission peak with the Equation 5.6. However this method does not yield the cyclotron time constant τ_s. There is more on this in the next section. The straight CPW sample also did not have a gate on it which meant there was no way to control the carrier density.

Unfortunately this option is not available for the other data sets due to the output being a differential voltage, so we opted for the first method of calculation from Equation 5.6. The effective mass is the apparent mass that the electron (hole) actually behaves like when traveling in a quantum well or heterojunction, due to the periodic potential of the crystalline structure. The effective mass multiplier of an electron has

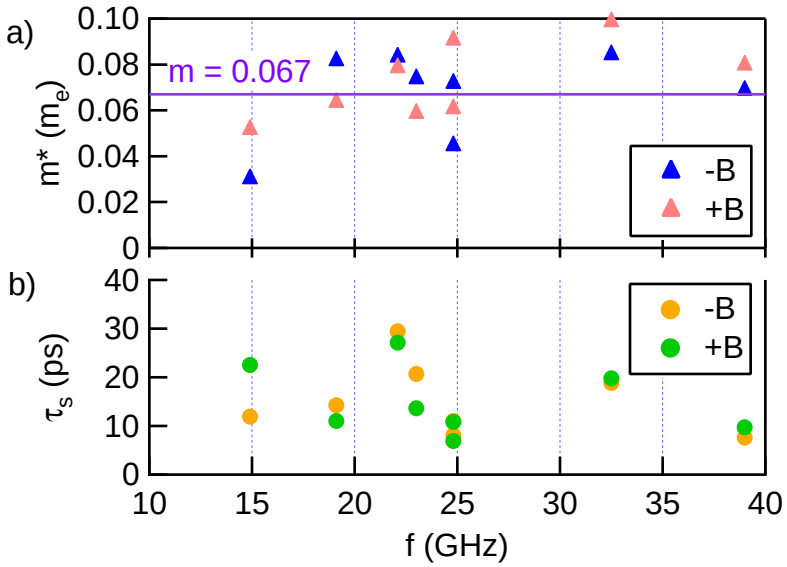

Figure 5.15: a) Effective mass and b) cyclotron time constant from the Drude model fit for the straight CPW.

been very well defined and documented as being $0.067 - 0.068$ [3, 6, 12, 19]. From Figure 5.15 we see that we are generally near the expected value for the effective mass. The discrepancy of the values might originate from the unknown frequency dependence of the reflected microwave power that could potentially change the shape of the cyclotron resonance signal.

5.4.1 2DEG Samples - Transmission

To measure the effective mass for the 2DEG samples, we used the procedure developed from the more complex 2DHG samples. We used these samples as a way to fine tune our technique and move beyond showing that we can see a signal to finding ways to optimize the quality of the signal we were obtaining. The two main reasons for using a 2DEG sample were calibrating the signal by identifying the very well known

effective mass multiplier at 0.067, and hopefully see MIRO in the sample so as to correlate the two (as we saw with the straight CPW sample in Figure 5.12).

We also note that there is a different delay from sweeping the magnetic field in the transmission data, as opposed to the correction needed for the R_{xx} data. We offset the magnetic field of the R_{xx} data slightly due to a hysteresis from the sweep direction and rate of the magnet. To compensate for this shift in the magnetic field, we used the cyclotron resonance's sharp symmetric peaks. This is a different kind of effect than the one presented in Ashkinadze, et al. [10], where a hysteresis was measured depending on sweep direction. After the correction, the straight CPW transmission results irradiated at 23 GHz(39 GHz) yielded the resonance minima at 0.05475 T(0.09415 T) and resulted in an effective mass multiplier of 0.0665(0.0675) which is reasonably close to the expected value of 0.067. Due to these and other effective mass multipliers calculated from a similar technique, we can conclude that we are indeed observing the fundamental cyclotron resonance transmission minima. There are a few outlier results at certain frequencies, but this is most likely due to the frequency variations in power transmission and reflection. In this preliminary result, we observed the fundamental cyclotron resonance and it matched up with our expectations for measuring the effective mass multiplier. From here we decided to use this to measure a wide variety of samples including the 2DHG effective mass.

The 2DEG samples came with their own challenges of trying to gate the high mobility 2DEG with new Si_3N_4 dielectrics. We tried a variety of samples ranging

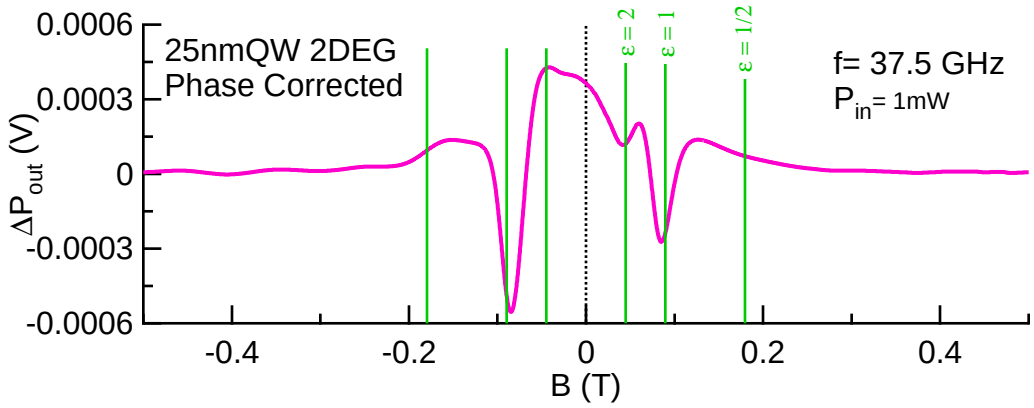

Figure 5.16: Phase corrected ΔP signal from 25nmQW 2DEG irradiated with 37.5 GHz, with $\epsilon = 2, 1, \frac{1}{2}$ highlighted. We can also see the possible resonance at $\epsilon = 2$, but nothing at $\epsilon = \frac{1}{2}$.

from quantum wells (25 nm, 20 nm) to heterostructures (HS, HJ), where we found that, after testing the samples with a magnetic field, their mobility was much lower than expected, potentially from the fabrication process or correctable with biased cooling [2]. In these samples we were unable to see MIRO in the R_{xx} signal, while the samples that had a large enough mobility to see MIRO (20nmQW with a gold gate), were drowned out by other large resonance features in the transmission.

25nmQW and HS Samples

The first 2DEG samples we tried with this gate technique were the 25nmQW and the HS samples with densities (when $V_g = Ground$) of $2.69 \times 10^{11}\,\mathrm{cm}^{-2}$ and $2.00 \times 10^{11}\,\mathrm{cm}^{-2}$ respectively. Each of these samples were gateable: the electrons could be pushed out and brought back by applying a gate voltage (see Figure 5.17) reproducibly.

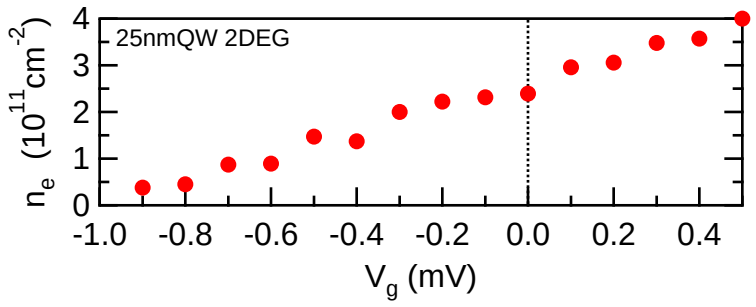

Figure 5.17: Gate dependence of the electron density for the 25nmQW 2DEG sample.

We noted that the mobility for these samples were strangely low: at 1.50×10^6 cm^2/Vs and 4.11×10^5 cm^2/Vs for the 25nmQW and HS samples respectively, much lower than needed to see MIRO ($\lesssim 3 \times 10^6$ cm^2/Vs). We expected that the mobility of these samples would be around 10×10^6 cm/Vs, but it seems that part of the fabrication process or the gate might be to blame for the lower mobility. Conversely, the transmission data we got from the ΔP measurement was exceptionally sharp (see Figure 5.16 and 5.18).

The data from the 25nmQW sample was taken as a quick survey and the results reveal that there were indeed very strong frequency dependent features corresponding to the cyclotron resonance at $\epsilon = 1$. However, due to the speed that the magnetic field was swept (0.2 T/min), most of the peaks did not line up where we expected them to and were slightly washed out.

For the HS data set, we swept the magnetic field much slower and focused on a much lower magnetic field range which yielded much sharper peaks at the fundamental cyclotron resonance locations that are associated with the effective mass of

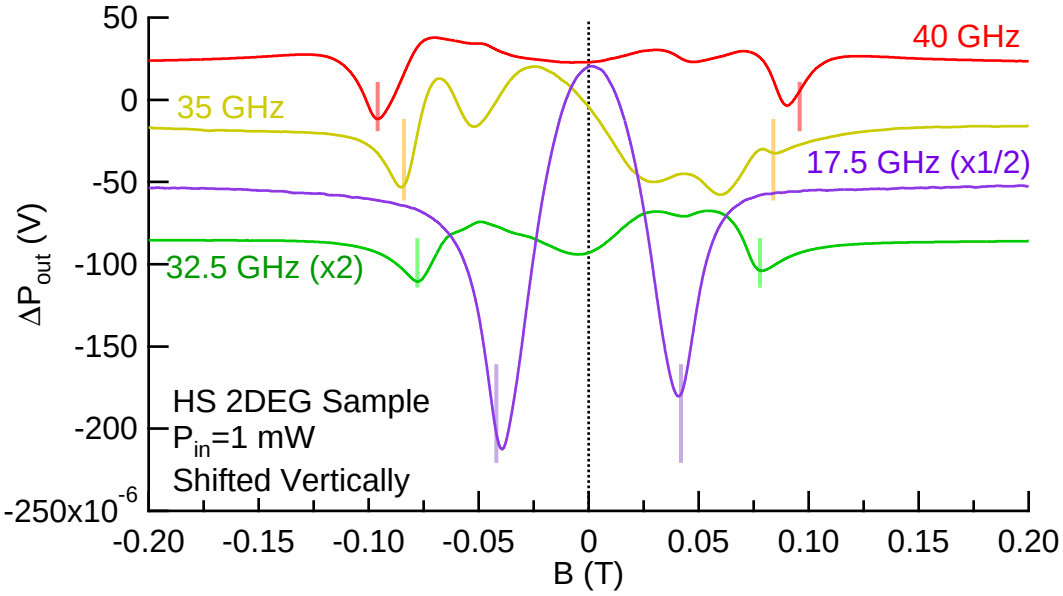

Figure 5.18: Example frequency dependence of the ΔP signal from the HS sample, the signals are shifted negatively along the vertical access. The voltage output from the 17.5 GHz data has been divided by 2 to match the others. The locations of the theoretical cyclotron resonance peaks are represented as the vertical lines.

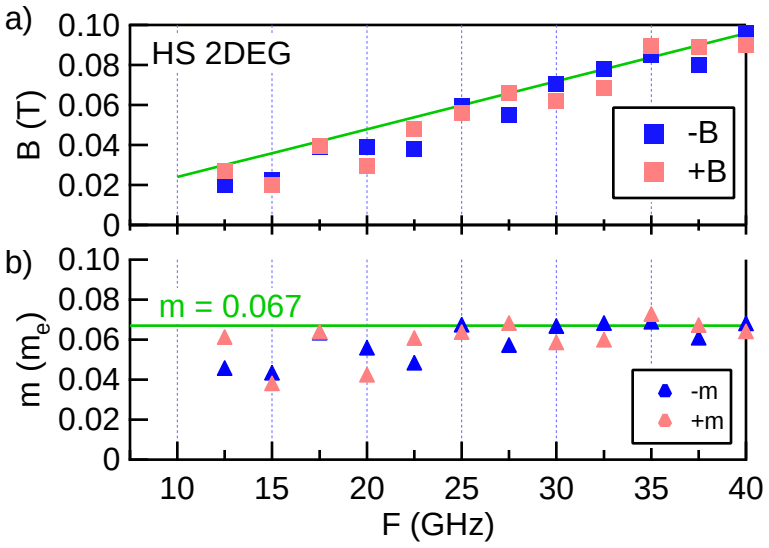

Figure 5.19: a) Frequency dependence of the HS sample's minima location in the magnetic field, $\pm B$. The green line is the expected relationship, assuming an effective mass multiplier of 0.067. b) Frequency dependence of effective mass using the results from figure a) and Equation 5.6.

F (GHz)	B_{min} (T)
40	0.0959
37.5	0.0899
35	0.0839
32.5	0.0779
30	0.0719
27.5	0.0659
25	0.0599
22.5	0.0539
20	0.0479
17.5	0.0419
15	0.0359
12.5	0.0300
10	0.0240

Table 5.1: Location of cyclotron resonance minima in the magnetic field associated with $m^* = 0.067 \cdot m_e$

$0.067m_e$ (see Table 5.1). From the results in Figures 5.18 and 5.19, there is a very definite frequency dependence of the ΔP data, which we can see when the effective mass is plotted in Figure 5.19b. We note that the values for the effective mass multiplier tend to drop off at lower frequencies, which could be due to an unknown reflection component. Another possibility is that at the same input power there is more microwave power reaching the sample at lower frequencies which heats up the ^3He bath more than at higher frequencies.

HJ Sample

From this point we moved to make a sample from a heterojunction wafer, HJ, using the $1 \times 3\,\mathrm{mm}$ mask, which yielded with density and mobility of $1.9 \times 10^{11}\mathrm{cm}^{-2}$ and $1.07 \times 10^{6}\mathrm{cm}^2/\mathrm{Vs}$. The mobility was quite a bit lower than expected by approximately

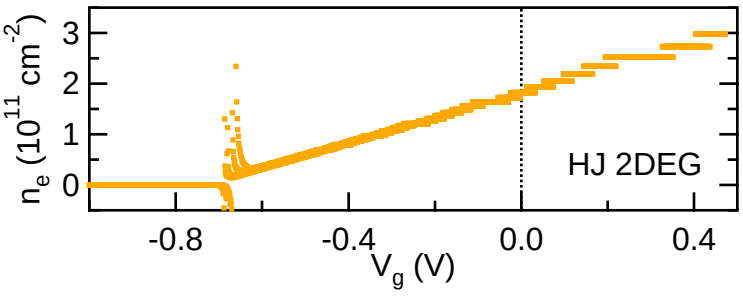

Figure 5.20: Change in electron density vs. the gate voltage for the HJ sample. Below $-0.75\,\mathrm{V}$ all the electrons are pushed out of the system.

an order of magnitude. This sample was fabricated with the slightly modified steps that would minimize any possible decrease in the mobility so that we would be able to see MIRO and a strong transmission signal in the same sample. However, there was a physical complication when fabricating these samples, potentially arising from the $1000\,\text{Å}$ of Si_3N_4 deposited as the dielectric due to mobile charges which affected the mobility. This sample had the same dimensions as the 25nmQW and the HS samples to maximize the surface area and increase the coupling to the microwaves. Even with the application of a gate, the mobility would not go higher than $1.5 \times 10^6\,\mathrm{cm/Vs}$ which is too low to see MIRO, irregardless of the high microwave input powers (up to $15\,\mathrm{dBm}$) and the higher sensitivity ΔR measurement. One possible solution would be to apply a gate bias while cooling the sample from room temperature. Previous studies with SiO_2 dielectric layers by J.-P. Cheng and B. D. McCombe state that this process could increase/decrease the mobility when a positive/negative voltage applied [2]. A similar effect might resolve the lower mobilities in our Si_3N_4 dielectric covered samples.

There was a hysteresis in the density depending on the gate voltage that was applied. This histories is is most likely due to mobile charges in the Si_3N_4 [47]. If we know what gate voltages yield the appropriate densities, we can oscillate the gate voltage with a square wave that will bypass the mobile charge effect and yield the same two densities: high density for the upsweep and less carriers for the downsweep. From Figure 5.20a we were able to find the negative gate bias that we could push out all the carriers ($V_g2 \leq -800\,\mathrm{mV}$) and what would bring them back ($V_g1 = +400\,\mathrm{mV}$) to the highest density at $3.01 \times 10^{11}\,\mathrm{cm}^{-2}$.

To measure a more accurate response, we swept the gate voltage from $-1000\,\mathrm{mV}$ to $+500\,\mathrm{mV}$ (as seen in Figure 5.20). From this data we can see the discontinuity in the density where the carriers are pushed out and the 2DEG moves into an insulating phase. Any voltage below this point can be used as V_g1 to create the background signal. Sweeping the gate continuously does not allow for a complete relaxation of the density which minimizes the hysteresis. The difference between this density and the more time intensive approach is most likely due to a relaxation related to the gate sweep rate [48].

From these limits we were able to see very strong ΔP frequency dependent peaks that we could identify as cyclotron resonance (see Figure 5.21). From these peaks we can calculate the effective mass and compare it to the known value of $0.067m_e$ in Figure 5.22b. We find that, similar to the previous data, the higher frequencies coincide with the expected effective mass multiplier. However, at lower frequencies

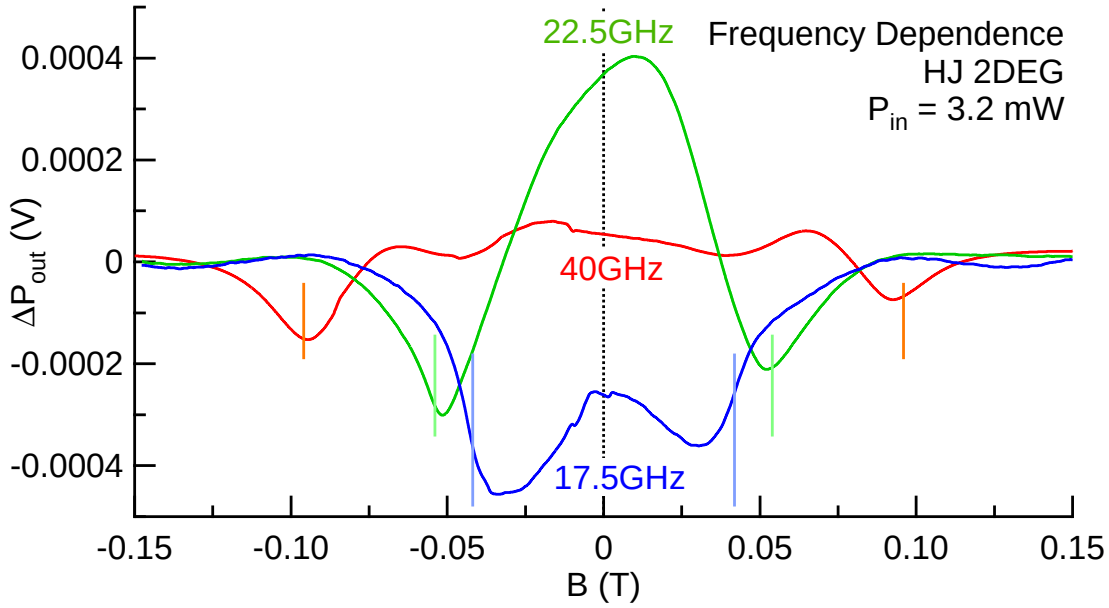

Figure 5.21: HJ frequency dependence with the fundamental cyclotron resonance marked by vertical lines.

there is a much larger deviation.

We also note the power dependence of this peak as seen in Figure 5.23b. The amplitude of the peak increases exponentially with an exponential increase in power as expected. This is slightly different than the power dependence in R_{xx} from the straight CPW sample, where it saturated and decreased.

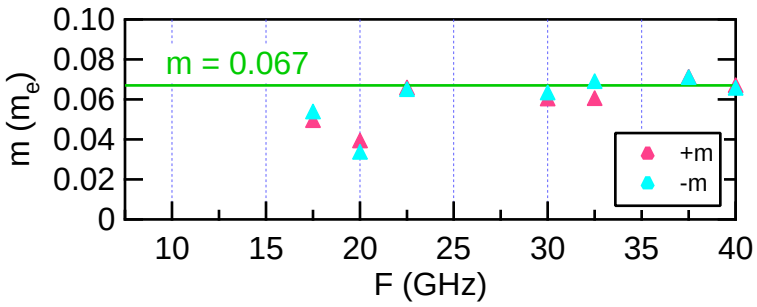

Figure 5.22: HJ frequency dependence of effective mass using the same method as Figure 5.19.

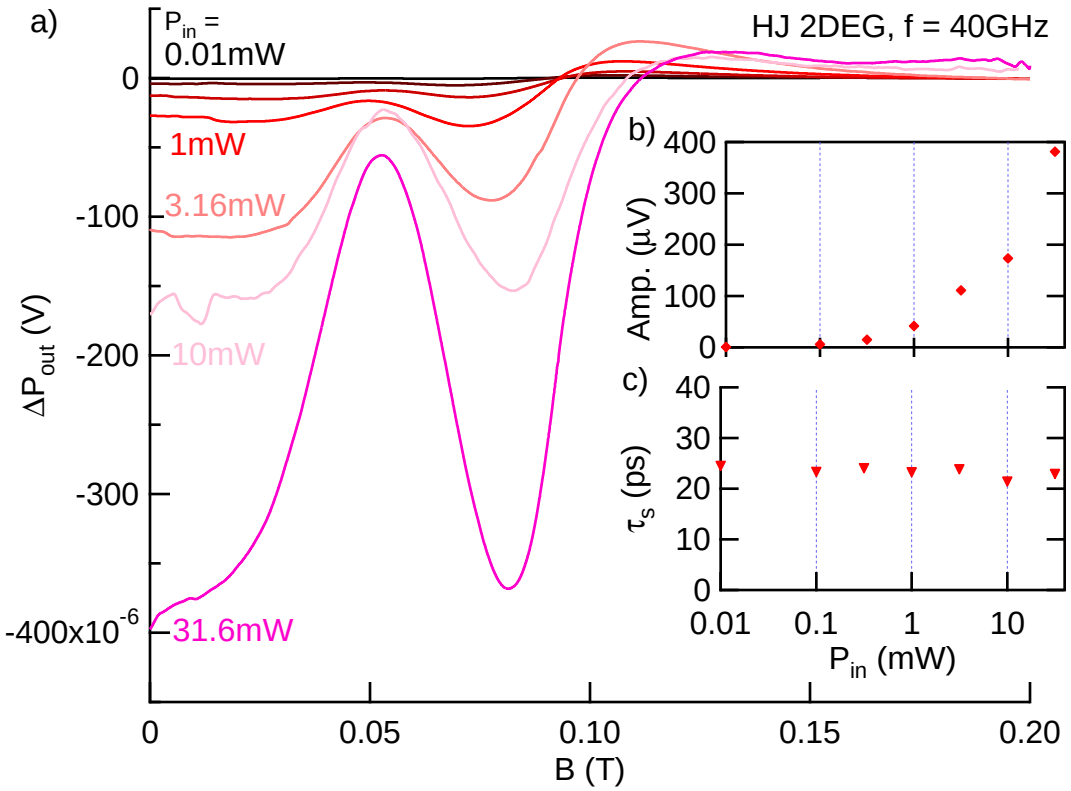

Figure 5.23: a) HJ Power dependence of ΔP at 40GHz. b) Peak amplitude of cyclotron resonance peak vs. input power. c) Cyclotron time constant calculated from the FWHM (using the method in Section 5.5).

We see from figure 5.23b that while the peak amplitude increases with input microwave power, the cyclotron time constant (inversely proportional to the FWHM) of the the peaks only vary slightly. The cyclotron time constant remains consistent, around 25 ps irregardless of power.

5.4.2 2DHG Samples - Transmission

Measuring the effective mass of a 2DHG was done using an asymmetric 15 nm quantum well (15nmQW) wafer to make a calorimetry measurement. This research was done by a previous student in this lab, Zhuoquan Yuan [6]. The results of that work measured the effective mass multiplier to be approximately 0.41 and also showed two carrier densities due to hole spin splitting. Another experiment by Kumar et al. measured the same effective mass multiplier for a lower density/mobility 2DHG system using transport measurements [5]. Since the effective mass of the heavy hole system is so much higher then that of the electron system (0.067), we thought it would be easier to determine the cyclotron resonance transmission signal.

We were able to use the same asymmetric 15nmQW wafer as Yuan [6], and a 20 nm symmetric quantum well wafer (20nmQW), to make 1×3 mm Hall bars with $AuPd$ gates. In both cases the microwave irradiation was irradiated through the polished back side of the wafer using the meander line. The gated 15nmQW and 20nmQW samples had a carrier density of $2 \times 10^{11}\,\mathrm{cm}^{-2}$ and $2.03 \times 10^{11}\,\mathrm{cm}^{-2}$ with a mobility of $8 \times 10^{5}\,\mathrm{cm}^2/\mathrm{Vs}$ and $0.9 \times 10^{5}\,\mathrm{cm}^2/\mathrm{Vs}$. As with the 2DEG samples the large dimensions

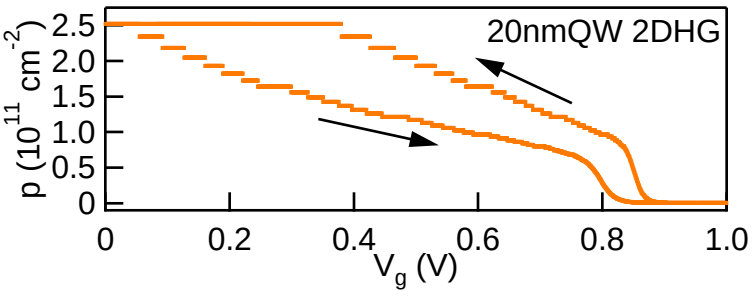

Figure 5.24: 20nmQW 2DHG density vs. gate voltage, used to identify V_g1 and V_g2.

of the Hall bar was to increase the coupling with the the microwaves. We did not expect any microwave response (other than an increase in the temperature) in R_{xx} of the 2DHG samples due to low mobilities for similar reasons to the 2DEG samples. Using these samples provided us with a way to develop the gate modulation technique which we applied to the 2DEG samples.

An important factor in doing the ΔP measurement was to measure the gate dependence of the sample to find when the carriers become totally removed from the system. It is also important to have a gated sample in which the carriers come back when the gate is turned off (initially using the single gatebox technique described in Figure 4.4, so $V_g1 = 0V$). To identify the gate limits for the 20nmQW 2DHG sample's V_g2, we used the data from Figure 5.24. Since the density disappears after 0.9 V we chose $V_g2 = 2\,\mathrm{V}$ to insure that all the carriers were removed from the system.

In our frequency dependence data from the 20nmQW 2DHG sample (Figure 5.25), we note that the transmission minima is directly proportional to the irradiation frequency as we would expect from the cyclotron resonance Equation 2.17 which also

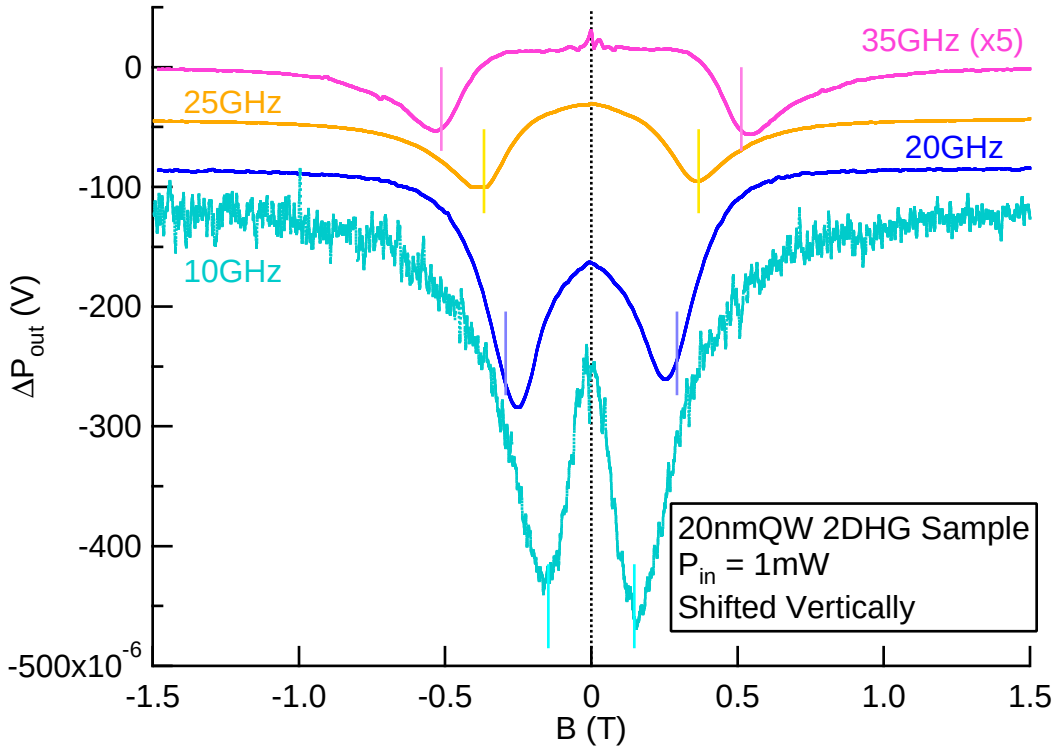

Figure 5.25: 20nmQW 2DHG frequency dependence irradiated with $P_{in} = 0\,\mathrm{dBm}$, where the minima is visibly dependent on the frequency of irradiation (not adjusted for phase correction due to lack of R_y data).

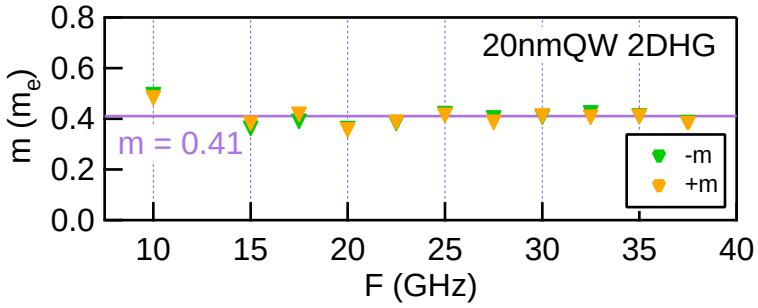

Figure 5.26: 20nmQW 2DHG Frequency dependence of the effective mass. The known effective mass of $m = 0.41m_e$ is highlighted to guide the eye.

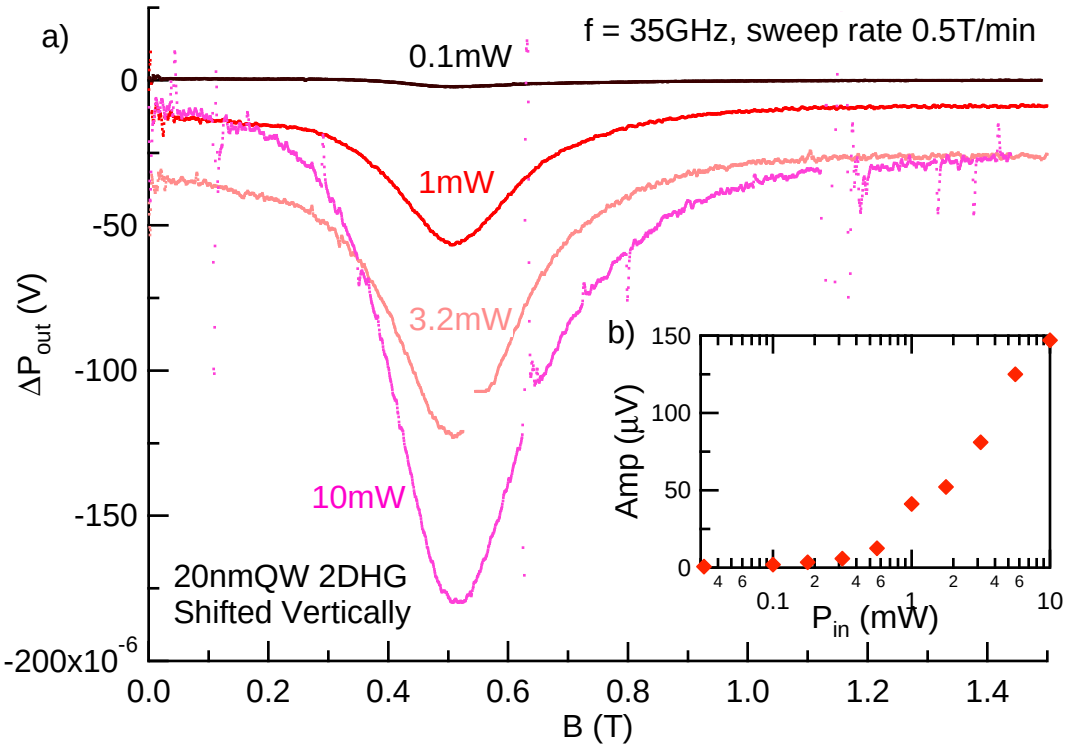

Figure 5.27: 20nmQW 2DHG power dependence from $-0.032 \rightarrow 10$ mW. The insert shows the peak amplitude measurement.

coincides with the higher frequency results from Cole et al. [9]. This data allowed us to calculated the effective mass of the Hole system to be very close to that which was seen by Kumar et al. [5] and Yuan [6], using different techniques.

We also took a power dependence at 35 GHz where the minima's amplitude had a Gaussian dependence on the input power in dBm (see Figure 5.27).

Similarly when taking the temperature dependence from 0.32 K to 12 K (as seen in Figure 5.29 for 22.5 GHz and 0 dBm), we found that amplitude of the cyclotron resonance dropped off exponentially with an increased in temperature and the minima moved to higher magnetic fields, increase in effective mass (Figure 5.30), and broad-

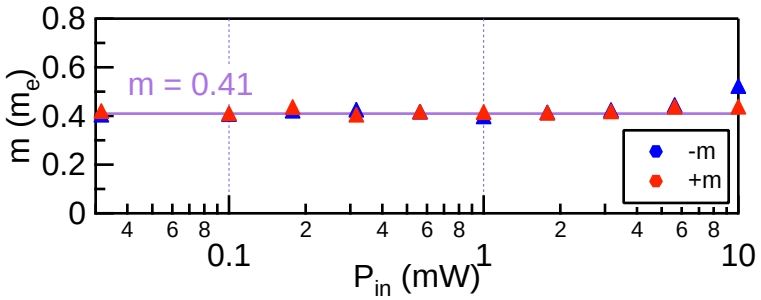

Figure 5.28: 20nmQW 2DHG power dependence on the effective mass, which remains consistently around the expected value of 0.41 regardless of heating effects to the system caused by microwaves.

ened out. From the broadening, we can see the cyclotron resonance minima increases possibly due to an increase of phonons that might be coupling to the electrons. This does bring up a question that would be interesting to develop further. While the signal is still measurable at higher temperatures, we can see that above $\sim 2\,\mathrm{K}$ the effective mass starts increasing dramatically. Another point to note is that by fitting these curves to Gaussian peaks we noticed that, in addition to the two major peaks, there is a third much more shallow centralized peak. As the temperature increases, we see that the cyclotron resonance peaks disappear leaving the centralized depression behind.

For the asymmetric 15nmQW 2DHG sample, fabricated with the same procedure as the 20nmQW sample, we were not able to push out the carriers fully before the leakage current became too large. The R_{xx} increased with applied gate voltage up to $2\,\mathrm{V}$ however there was still a visible SdH signal. This means that all the carriers could not be removed from the 2DHG, so the ΔP measurement could not be done to remove the background. We still tried a frequency dependence of ΔP, and while

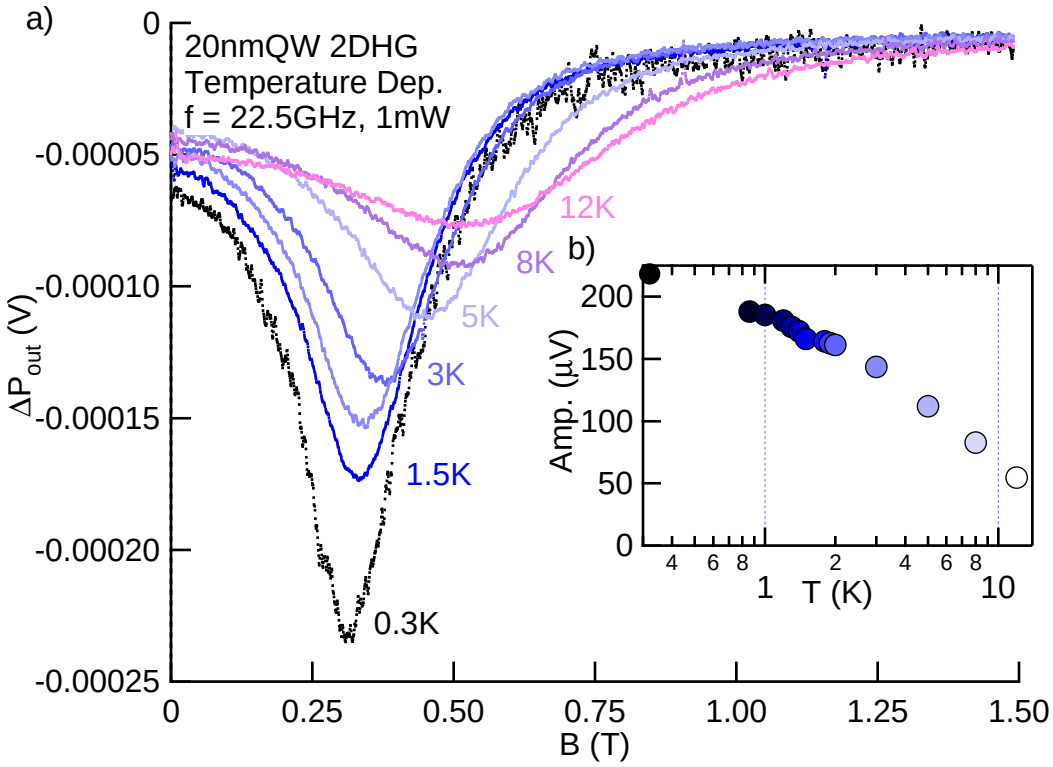

Figure 5.29: a) 20nmQW 2DHG temperature dependence from 0.32 → 12 K. The insert shows the peak amplitude measurement for each peak.

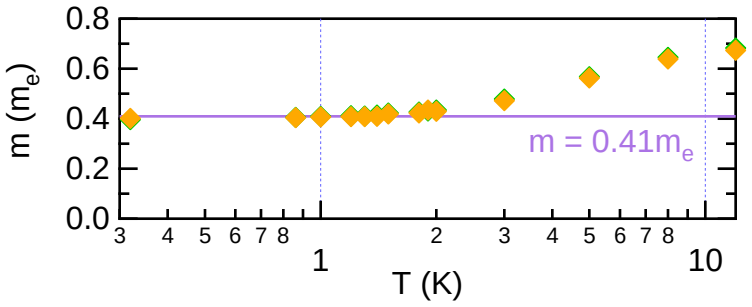

Figure 5.30: Temperature dependence of the 20nmQW 2DHG effective mass.

the transmission signal had some frequency dependence, it was much too complicated with many minima in the ΔP signal.

What we can take from these measurements are that the differential ΔP measurement technique we developed, successfully subtracted the background signal from that of the 2D system leaving only the 2D systems' response to microwave irradiation. From the preliminary data for this new technique, we were able to identify the effective mass for the system and confirm with known values obtained from different techniques. Although we were not able to see spin splitting in the cyclotron resonance peak as we expected when the gate voltage was varied. For the next step in this experiment it would be interesting to place a high mobility 2DHG sample in a two-axis magnet and look for the cyclotron spin splitting. Additionally It would also be interesting to explore the relationship between temperature and the effective mass of the 2DHG.

5.5 Cyclotron Time Constant

As stated from the previous section, in the straight CPW sample we could directly fit the cyclotron resonance peak which yielded the effective mass multiplier (which could be calculated through other means for the other samples) and the cyclotron time constant τ_s. From this fit we found that the cyclotron time constant was approximately 20 ps (see Figure 5.15). The slight variations with respect to the frequency input could have a variety of reasons, first being that for this fit we did not take the

reflection into account. Also the probe itself has a frequency dependent transmission (which is mapped out by taking a frequency power profile, similar to Figure 3.6) and, since each frequency has a different transmission of power, there are different ^3He bath temperatures. This could also affect the full width half max (FWHM or Γ) width of the resonance peak along with the magnetic sweep rate [7].

Since we could not use the Drude conductivity model (Equation 5.7) for the HJ sample, we had to use a simpler Gausian fit to the fundamental cyclotron resonances in differential voltage output. Instead we needed to use

$$\tau_S = \frac{m^*}{e\Gamma} \tag{5.9}$$

where Γ is the full width half max (FWHM).

Keeping both the frequency (20 GHz) and V_g2 constant (enough to push out the carriers) we can adjust V_g1 to observe the density dependence of the broadening of Γ (Figure 5.31).

Fitting a Gaussian to these peaks, we are able to find the peak height and the Γ and plot each against the density by way of the gate voltage (Figure 5.32). We notice that the peak amplitude increases as we increase the density; this includes the point in the gate voltage where increasing the gate voltage decreases the density (around 0.4 V). From the data presented in Figure 5.33 we find that, regardless of frequency or density, the cyclotron time constant remains fairly constant. We can also apply this technique to measure the cyclotron time constant in 2DHG as well as 2DEG

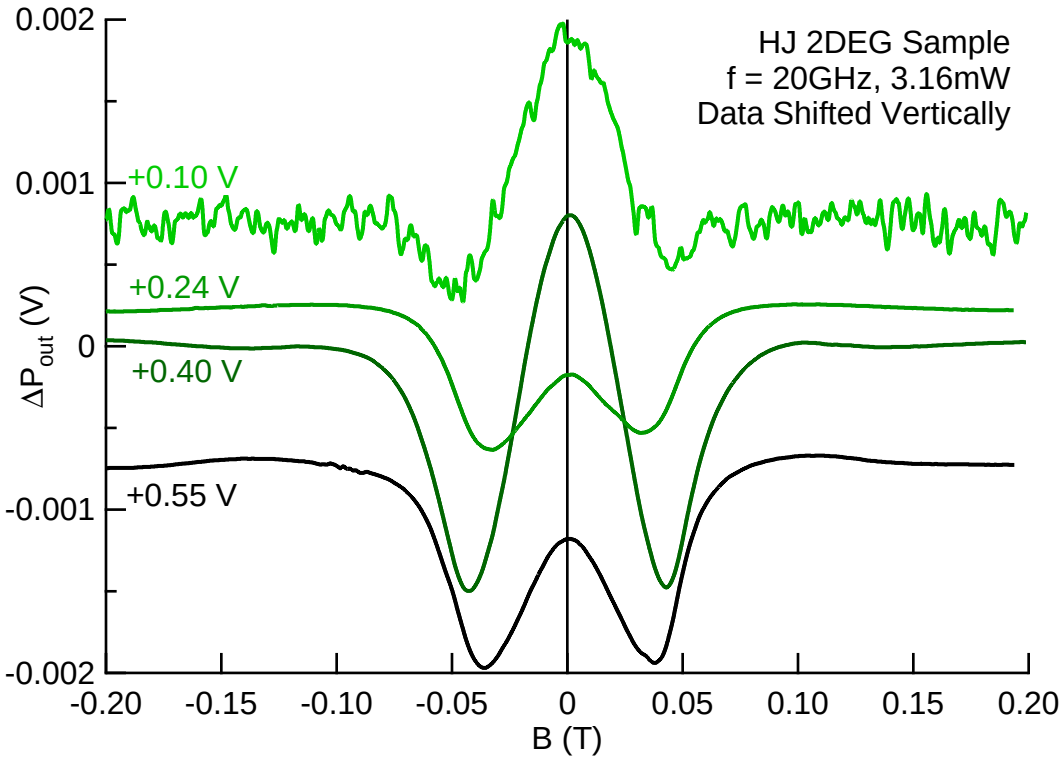

Figure 5.31: Gate voltage dependence (V_g1), holding $V_g2 = -0.8V$.

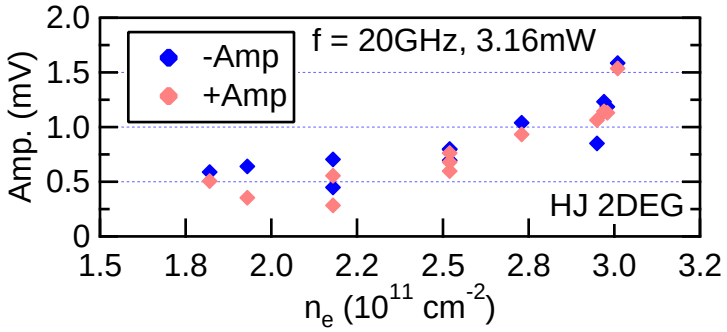

Figure 5.32: Electron density dependence on the peak amplitude from figure 5.31, at 0.4 V we see a saturation of amplitude and density.

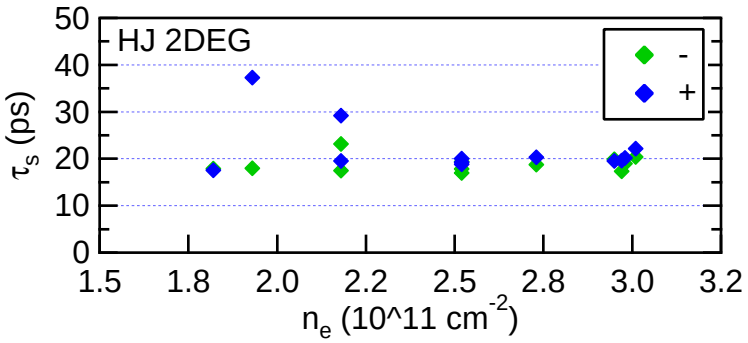

Figure 5.33: The density dependence of the cyclotron time constant.

samples.

Looking at the temperature dependence of the 20nmQW 2DHG sample (Figure 5.34) we start to see that the cyclotron time constant remains fairly consistent until $\sim 1.5\,\mathrm{K}$ whereupon it starts to drop. This is expected due to the increase temperature, and therefore increase in lattice vibration which decreases the time between scattering events. As with the 2DEG system this also justifies a measurement below 1.5 K to freeze out thermal interactions. The results obtained are under the assumption that the effective mass is constant at $0.41m_e$. However, from the same Gaussian fit where we got Γ we also noted that the effective mass has a similar temperature dependence. If we take this value also into account the cyclotron scattering time flattens out around 17 ps and has a much weaker temperature dependence.

Of course there are corrections to the Γ fit, due to broadening and saturation effects that would change our exact calculated value for the cyclotron constant [34]. However, this does not change the observed independence of the cyclotron time constant in regards to the carrier density. This result is also interesting in contrast to the peak

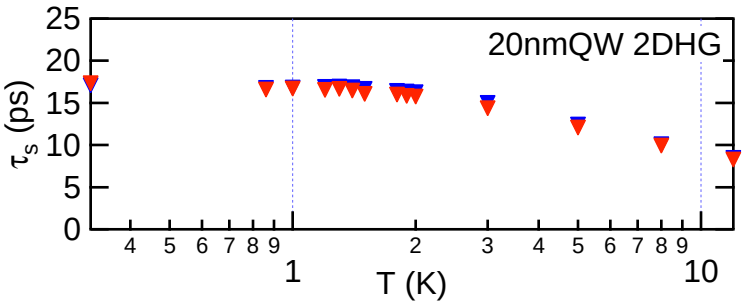

Figure 5.34: Temperature dependence of the cyclotron constant from 20nmQW 2DHG for 22.5 GHz, assuming that the effective mass remains constant at $0.41m_e$.

dependence on density, where the amplitude increases but the Γ remains constant. Since this data was preliminary, it opens up a great deal of possibilities to explore the cyclotron time constant and effective mass in a variety of new systems.

Chapter 6

Conclusions

From our results we find that we were able to develop a new data taking method that yielded very sensitive results that confirmed previous research and opened doors to new and innovative ways to evaluate properties of 2DEG and 2DHG systems. Initially we set out to develop a new way to irradiate a sample using a coaxial arrangement as opposed to a waveguide geometry, in order to utilize its digital circuit-based advantages. Previous waveguide irradiation techniques at our disposal were limiting and did not align with our goal of measuring microwave transmission across a 2D system. From the coax geometry, we could control how the samples were irradiated and to what specific frequency and power, and therefore measure the transmission across the sample.

From previous research [6, 10, 21, 23, 37, 42, 49, 50], complications arose from using a microwave waveguide geometry, especially when control of the electric and magnetic field components of the microwaves was important. While this geometry has been successful in blanketing a sample with high power Faraday irradiation at frequency ranges from $26.5 - 150\,\mathrm{GHz}$, it lacks the ability to control the microwave power, other than through attenuation near the source. Due to the blanketing of microwave irradiation, there was a concern that metallic sample contacts would interfere with the fields. This waveguide geometry also makes it difficult to measure

the microwave transmission through a sample, especially one that is gated, due to the gate reflecting the microwaves.

We were able to use the waveguide geometry to measure the edge magnetoplasmon oscillations (EMPO) (Section 5.2) and compare our results to the previous research by Kukushkin et al. [14]. These results coincided with the proportionality of $\Delta B \propto \frac{n_s}{\omega_{MW}}$, where n_s is the carrier density and ω_{MW} is the microwave frequency of irradiation (from Equation 2.21). Contrary to the results by Kukushkin et al., we did not see any dependence in the period of oscillation, ΔB, on the length between the measurement leads, L. We were able to measure the same EMPO ΔB between lead separations of 1 mm and 2 mm. This led us to the conclusion that the EMPO oscillations are not simply localized between the leads but travel around the edges of the entire sample where they can constructively/destructively interfere. We also discovered that the EMPO signal is separate from that of MIRO and SdH which was especially relevant in the temperature dependence results where the period of oscillation was independent of temperature (Figure 5.11). The results from R_{xx} also hinted at a strong first order FMIRO signal. In addition, this research also provided us with a strong background in the general measurement techniques that would be applied for the following projects.

As stated earlier, the limitations of the waveguide geometry restricted our ability to control how microwaves were delivered to the sample, which led us to an alternative coax base design. Incorporating this idea meant creating a completely new probe and overcoming the specific challenges associated with heat dissipation and irradiation

delivery to the 2D sample. The huge advantage of this new system was that we could dial in the frequency (through $2-40\,\mathrm{GHz}$), the irradiation power ($0 \rightarrow 100\,\mathrm{mW}$), and that we could incorporate the ability to take microwave transmission data (through a second coax line). As with any newly-developed technique, there were a large amount of adjustments to make, primarily with the sample fabrication.

We found that our samples required new fabrication techniques to work with the dual coax line probe, primarily incorporating metallic alloy co-planar waveguides to the samples. This made it possible to control the direction of the microwaves by evaporating the CPW on either side of a $100\,\mu\mathrm{m}$ Hall bar. From this geometry we were the first to simultaneously measure the 2DEG's resistance along with the microwave transmission, which yielded a fundamental cyclotron resonance transmission minima. Another benefit of this geometry and frequency range was that we could focus the microwave power specifically to the 2DEG with little waste radiation, which yielded strong MIRO and FMIRO peaks in R_{xx} from $\epsilon = 2, 1, \frac{1}{2}, \frac{1}{3}, \frac{1}{4}, \frac{1}{5}$ (using Equation 2.15). In addition to visualizing these peaks, we were able to measure their frequency dependence and concluded that they were indeed FMIRO due to having the same frequency dependence as MIRO, sharing the same slope trend. This points to both features having similar physical origins, where those origins are currently under question. We also noticed that, while there was a large response in the transmission due to the fundamental cyclotron resonance (and potentially the second harmonic), there was no transmission response for any of the FMIRO peaks. This

might have been because they were so small as to not be measurable or there was no correlation between FMIRO and cyclotron resonance. This is interesting due to the fundamental cyclotron resonance factoring in to current theoretical explanations of the multiphoton and resonant sidebands for FMIRO.

With the preliminary results completed from the FMIRO experiment, we looked into decreasing the preparation complexity of each individual sample and incorporating a gate over the 2D system, while increasing the probe's versatility. Both of these challenges resulted in the development of an experiment based on an irradiation technique using a meanderline CPW to irradiate the sample from the back, so that it would not interfere with the top gate. To accomplish this, the back side needed to be polished to remove any metallic base components to the wafer. In order to control the carrier density of the 2D system we utilized a Si_3N_4 dielectric and $AuPd$ alloy top gate. From these components we created a new differential measurement technique for the power transmission, ΔP, based on the single modulation ΔR technique. This ΔP technique allowed us to subtract the background microwave resonances from everything except the 2D system under observation using an oscillating gate voltage. While this did not allow for simultaneous resistance measurements, due to the oscillating gate voltage, we could still measure it in the same cool down.

From the results in the transmission data, we found fundamental similarities to the signals we measured, especially with respect to the fundamental cyclotron resonance peak. While the frequency, power, temperature, and gate dependence of the peaks

varied sample to sample, there were certain similarities among all the responses, potentially not in the lineshape but, as we found, in the calculation of the effective mass and cyclotron time constant. We were able to use the same procedure for measuring this feature in both the 2D electron and hole systems, that resulted in confirming the effective mass of each as $0.067m_e$ and $0.41m_e$ respectively. In both systems the frequency dependence of the cyclotron time constant drifted slightly but resulted in a value around 20 ps. What is new from the cyclotron time constant data is that irregardless of the gate voltage (electron density) of the system, the cyclotron time constant remains consistent while at the same time the peak amplitude for each density increases until saturation. This was a surprising result since we would expect, that when changing the carrier density (by a gate), we would also see an increase in interactions among the electrons in the system, resulting in a decrease of the cyclotron time constant. Both of these systems result in a greater fundamental understanding of the 2D electron and hole systems (by way of microwave irradiation at low temperatures) that were previously only measurable through specialized techniques.

Due to the development of the meanderline irradiation system we can measure new samples, provided they are transparent to microwaves and can be gated (the carriers can be completely removed and brought back). This opens the door for a variety of new samples to be measured, including single nanotube or graphene samples, and once the fabrication technique is perfected, high mobility 2DEG samples. Ideally if we had a gated high mobility 2DEG sample, with a polished back side, we could

measure MIRO and cyclotron transmission in the same sample in order to compare the resonance features. Similarly, we could use this probe with a prepared high mobility 2DHG sample in a two-axis magnet and potentially see spin splitting in the cyclotron resonance peak. The measurement technique could also be improved slightly to change from a diode sensor voltage output to a calibrated mW output, which could be done by incorporating a triggerable microwave power detector. One advantage of this would be an ability to convert from mW to a normalized absorption that could be fitted to the Drude conductivity model [46]. Our ΔP technique can also be used to measure the effective mass and cyclotron time constants of new gated materials.

Hopefully the extensive work that was done to develop this microwave transmission line probe and differential power technique will provide the basis for the next series of experiments in microwave irradiated systems.

Bibliography

[1] Engel, L. W., Shahar, D., Tsui, D. C., and Kurdak, C. *Physical review letters* **71**(16), 2638–2641 (1993).

[2] Cheng, J. P. and McCombe, B. D. *Physical Review B* **44**(7), 3070–3082 (1991).

[3] Laughlin, R. B. *Physical Review B* **27**(6), 33833389 (1983).

[4] Tan, Y.-W., Zhu, J., Störmer, H. L., Pfeiffer, L. N., Baldwin, K. W., and West, K. W. *Physical Review Letters* **94**(1), 2–5 (2005).

[5] Kumar, M., Mori, G., Capotondi, F., Biasiol, G., and Sorba, L. *Solid State Communications* **135**(1-2), 57–61 (2005).

[6] Yuan, Z. Q. *Quantum Transport in Spatially Modulated Two- dimensional Electron and Hole Systems*. Phd thesis, Rice University, (2009).

[7] Chou, M. J., Tsui, D. C., and Weimann, G. *Physical Review B* **37**(2), 848–854 (1988).

[8] Guldner, Y., Voos, M., Vieren, J. P., Hirtz, J. P., and Heiblum, M. *Physical Review B* **36**(2), 12661268 (1987).

[9] Cole, B. E., Chamberlain, J. M., Henini, M., Cheng, T., Batty, W., Wittlin, A., Perenboom, J. A. A. J., Ardavan, A., Polisski, A., and Singleton, J. *Physical Review B* **55**(4), 2503–2511 (1997).

[10] Ashkinadze, B. M. and Yudson, V. I. *Physica E* **6**(1-4), 182–186 (2000).

[11] Potemski, M., Studenikin, S. A., Sachrajda, A. S., Hilke, M., Pfeiffer, L. N., and West, K. W. *Physical Review B* **71**(245313), 1–9 (2005).

[12] Zudov, M. A. *Millimeterwave photoconductivity spectroscopy in two-dimensional electron systems*. Phd thesis, University of Utah, (1999).

[13] Zudov, M. A., Du, R. R., Pfeiffer, L. N., and West, K. W. *Physical Review Letters* **90**(4), 2–5 (2003).

[14] Kukushkin, I. V., Akimov, M., Smet, J. H., Mikhailov, S., Klitzing, K. V., Aleiner, I., and Falko, V. *Physical Review Letters* **92**(23), 1–4 (2004).

[15] Davies, J. *The Physics of Low-Dimensional Semiconductors, an Introduction*. Camridge University Press, New York, (1998).

[16] Lane, P. and Greene, R. L. *Physical Review B* **33**(8), 5871–5874 (1986).

[17] Eisenstein, J. P., Boebinger, G. S., Pfeiffer, L. N., West, K. W., and He, S. *Physical Review Letters* **68**(9), 1383–1386 (1992).

[18] Störmer, H. L., Dingle, R., Gossard, A. C., Wiegmann, W., and Sturge, M. D. *Journal of Vacuum Science and Technology* **16**, 1517 (1979).

[19] Maan, J. C., Englert, T., and Tshi, D. C. *Applied Physics Letters* **40**(7), 609–610 (1982).

[20] Greene, R. L., Bajaj, K. K., and Phelps, D. E. *Physical Review B* **29**(4), 1807–1812 (1984).

[21] Cole, B. E., Peeters, F., Ardavan, A., Hill, S., Singleton, J., Batty, W., Chamberlain, J. M., Polisskii, A., Cheng, T., and Henini, M. *J. Phys.: Condens. Matter* **9**, 3163–3179 (1997).

[22] Stone, K., Yang, C. L., Yuan, Z. Q., and Du, R. R. *Physical Review B* **76**(15), 2–5 October (2007).

[23] Zudov, M. A. and Du, R. R. *Physical Review B* **64**(20), 3–6 (2001).

[24] Mani, R. G., Smet, J. H., Klitzing, K. V., Narayanamurti, V., Johnson, W. B., and Umansky, V. *Nature* **420**(12), 646–650 (2002).

[25] Durst, A. C., Sachdev, S., Read, N., and Girvin, S. M. *Physical Review Letters* **91**(8), 1–4 (2003).

[26] Dmitriev, I. A., Mirlin, A. D., Vavilov, M. G., Aleiner, I. L., and Polyakov, D. G. *Physical Review B* **71**(11), 1–11 March (2005).

[27] Zudov, M. A. *Physical Review B* **69**(4), 2–5 January (2004).

[28] Dmitriev, I. A., Mirlin, A. D., and Polyakov, D. G. *Physical Review Letters* **91**(22), 1–4 November (2003).

[29] Studenikin, S. A., Potemski, M., Sachrajda, A. S., Pfeiffer, L. N., Hilke, M., and West, K. W. *IEEE Transactions On Nanotechnology* **4**(1), 124–131 (2004).

[30] Tung, L.-C., Yang, C. L., Smirnov, D., Pfeiffer, L. N., West, K. W., Du, R. R., and Wang, Y.-J. *Solid State Communications* **149**(37-38), 1531–1534 (2009).

[31] Zudov, M. A., Du, R. R., Pfeiffer, L. N., and West, K. W. *Physical Review B* **73**(4), 41303 (2006).

[32] Dorozhkin, S. I., Smet, J. H., Klitzing, K. V., Pfeiffer, L. N., and West, K. W. *JETP Letters* **86**(8), 543–547 December (2007).

[33] Ando, T., Fowler, A. B., and Stern, F. *Reviews of Modern Physics* **54**(2), 437–672 (1982).

[34] Wang, X., Hilton, D. J., Reno, J. L., Mittleman, D. M., and Kono, J. *arXiv:1003.2795v1* , 1–7 (2010).

[35] Luo, J. K., Ohno, H., Matsuzaki, K., and Hasegawa, H. *Japanese Journal of Applied Physics* **27**(10), 1831–1840 (1988).

[36] Murav'ev, V. M., Kukushkin, I. V., Parakhonskii, A. L., Smet, J. H., and Klitzing, K. V. *Journal of Experimental and Theoretical Physics Letters* **83**(6), 246–249 May (2006).

[37] Mola, M., Hill, S., Goy, P., and Gross, M. *Review of Scientific Instruments* **71**(1), 186 (2000).

[38] Hill, S., Brooks, J., Qualls, J., Burgin, T., Fravel, B., Montgomery, L., Sarrao, J., and Fisk, Z. *Physica B: Condensed Matter* **246-247**(1-4), 110–116 May (1998).

[39] Wen, C. *IEEE Transactions on Microwave Theory and Techniques* **17**(12), 1087–1090 (1969).

[40] AppCAD. `http://www.hp.woodshot.com/`, (2002). Agilent Technologies.

[41] Chen, Y. P., Sambandamurthy, G., Engel, L. W., Tsui, D. C., Pfeiffer, L. N., and West, K. W. *International Journal of Modern Physics B* **21**, 1379–1385 (2007).

[42] Wiedmann, S., Gusev, G. M., Raichev, O. E., Bakarov, A. K., and Portal, J. C. *Physical Review B* **80**(35317) (2009).

[43] Hatke, A. T., Chiang, H.-S., Zudov, M. A., Pfeiffer, L. N., and West, K. W. *Physical Review Letters* **101**(246811), 1–4 (2008).

[44] Dmitriev, I. A., Mirlin, A. D., and Polyakov, D. G. *Physical Review Letters* **99**(20), 206805 (2007).

[45] Yoshioka, D. *J. Phys. Soc. Japan.* **53**(11), 3740–3743 (1984).

[46] Dresselhaus, G., Kip, A. F., and Kittel, C. *Physical Review* **98**(2), 368–384 (1955).

[47] El Amrani, A., Menous, I., Mahiou, L., Tadjine, R., Touati, A., and Lefgoum, A. *Renewable Energy* **33**(10), 2289–2293 (2008).

[48] Rossler, C., Feil, T., Mensch, P., Ihn, T., Ensslin, K., Schuh, D., and Wegscheider, W. *arXiv:1002.3450v1* , 1–10 (2010).

[49] Ye, P. D., Engel, L. W., Tsui, D. C., Simmons, J. A., Wendt, J. R., Vawter, G. A., and Reno, J. L. *Applied Physics Letters* **79**(14), 2193 (2001).

[50] Willett, R. L., Pfeiffer, L. N., and West, K. W. *Physical Review Letters* **93**(2), 2–5 July (2004).

Appendix A

Sample Preparation

A.1 Sample Fabrication Recipe

Polishing backside:

1. Use grinder – take off $50\,\mu$m, or enough to remove metallic material and leave a polished surface.

Mask Making:

1. Take exposed mask out of machine.
2. Develop: wash in MS-351:H20 (2:5 ratio) for 60 s.
3. Etch: CEP-200 for ~ 60 s or until Cr has been fully etched away, should be able to see through completely in exposed areas.
4. Clean: Positive photo resist stripper PRS-100 for $2-5$ min until photo resist is washed away

    (a) Wash with DI

Photolithography:

1. Clean Sample:

    (a) ACE/5 min

(b) Meth/5 min
(c) DI/5 min

2. Spin on S1813 positive photoresist:

(a) 6000 rpm / 50 s @ 1000 $^{\text{rpm}}/_{\text{s}}$

3. Soft Bake: 90 C / 50 s
4. Expose: 9.5 s
5. Develop: MF-321: 90 s $\rightarrow DI$

Contacts:

1. High Mobility 2DEG GaAs/AlGaAs (Developed by Yuan[6])

(a) Follow Photolithography section using contact mask (mask with windows open for contacts)
(b)

	Ge	Pd	Au
Thickness Å	430	300	870
Rate $^{\text{Å}}/_{\text{s}}$	1.5	1.5	2

(c) Anneal at 450 C for 12 min(20 min from switching on heater)
(d) In with 25 μm Au wire

2. High Mobility 2DHG

(a) In/Zn alloy (50:50) made from melting In and Zn shot with a soldering iron

(b) Anneal at 450 C for 12 min(20 min from switching on heater)

Etching:

1. Follow Photolithography section
2. Hard Bake: 100 C / 45 s
3. Using $H_3PO_4 : H_2O_2 : H_20$ (1:1:38) etchant, 1200 $\text{Å}/\text{min}$ for 3 min

Ultra Cleaning:

1. Used to completely remove any photoresist, to prevent the liftoff of a finished gate

   (a) ACE in sonicator @ +50 C/10 min
   (b) ACE/30 min
   (c) Meth/5 min
   (d) DI/5 min

2. In the event that sonication would be too violent to the sample:

   (a) Place sample in boiling ACE at 130 C for 15 min
   (b) Meth/5 min
   (c) DI/5 min

Gate:

1. Dielectric evaporation

   (a) Al_2O_3– E-beam evaporator

      i. 500 Å @ 2 $^{Å}/_{s}$

   (b) Si_3N_4– PECVD, Desired thickness $500 - 1000$ Å

      i. Fast – 500 $^{Å}/_{min}$

         A. 600 mTorr
         B. 50 W
         C. 325 C
         D. SiH_4 - 12 sccm
         E. NH_3 - 10 sccm
         F. N_2 - 200 sccm

      ii. Slow – 275 $^{Å}/_{min}$ (More uniform dielectric)

         A. 625 mTorr
         B. 30 W
         C. 350 C
         D. SiH_4 - 12 sccm
         E. NH_3 - 10 sccm
         F. N_2 - 200 sccm

      iii. RIE – To etch windows in the Si_3N_4 to reach the evaporated contacts, or the sample surface

         A. Etching Si_3N_4 – 2400 $^{Å}/_{min}$ – 70 s for 500 Åof Si_3N_4 deposited

B. ICP – 300 W
C. RIE – 100 W
D. Pressure – 100 mTorr
E. CF_4– 50 sccm
F. O_2– 6 sccm

2. Gate Evaporation – E-beam evaporator on top of dielectric

(a) *Al* gate (did not use due to superconducting at He3 temps and strong Cyclotron Resonance)

i. Turn off e-beam sweeping and ramp up power very slowly up to 4.4%
ii. 1000 Å @ 2 Å/s

(b) *AuPd* gate – to minimize CR due to alloy scattering lengths

i. 50:50 alloy by mass (melted in the e-beam evaporator)
ii. E-beam settings averaged from *Au* and *Pd*
iii. Evaporation

A. *Ti* (50 Å @ 0.5 Å/s)
B. *AuPd* (1000 Å @ 2 Å/s)

iv. Liftoff

A. ACE/5 min or until all metal has visibly removed
B. Meth/5 min
C. DI/5 min

Appendix B

Stycast with Graphite preparation

1. Mix Stycast 1260 or 2850FT in separate large mouth container, add a few grams of graphite, mix vigorously
2. Pump out air bubbles slowly
3. When bubbles stop rising to surface, bring to atmosphere and pour into mold
    (a) If large volume, place mold into water bath to prevent melting of the mold (if plastic)

Appendix C

Density Calculation

Density calculation Identify the filling factors

Use relation:

$$\nu_a \cdot B_a = \nu_1 \cdot B_1$$

Where

$$B_1 = \frac{h}{e} \cdot \tilde{n_s}$$

and

$$\frac{h}{e} = \frac{6.626 \times 10^{-34} \, \frac{\mathrm{m^2 kg}}{\mathrm{s}}}{1.6 \times 10^{-19} \, \mathrm{C}} = 4.136 \times 10^{-11} \, \frac{\mathrm{cm^2 kg}}{\mathrm{s \cdot C}}$$

so

$$\tilde{n_s} = \frac{\nu_a \cdot B_a}{\frac{h}{e}} \tag{C.1}$$

and

$$n_s = \tilde{n_s} \times 10^{11} \, \mathrm{cm^{-2}}$$

Appendix D

Probe Schematics

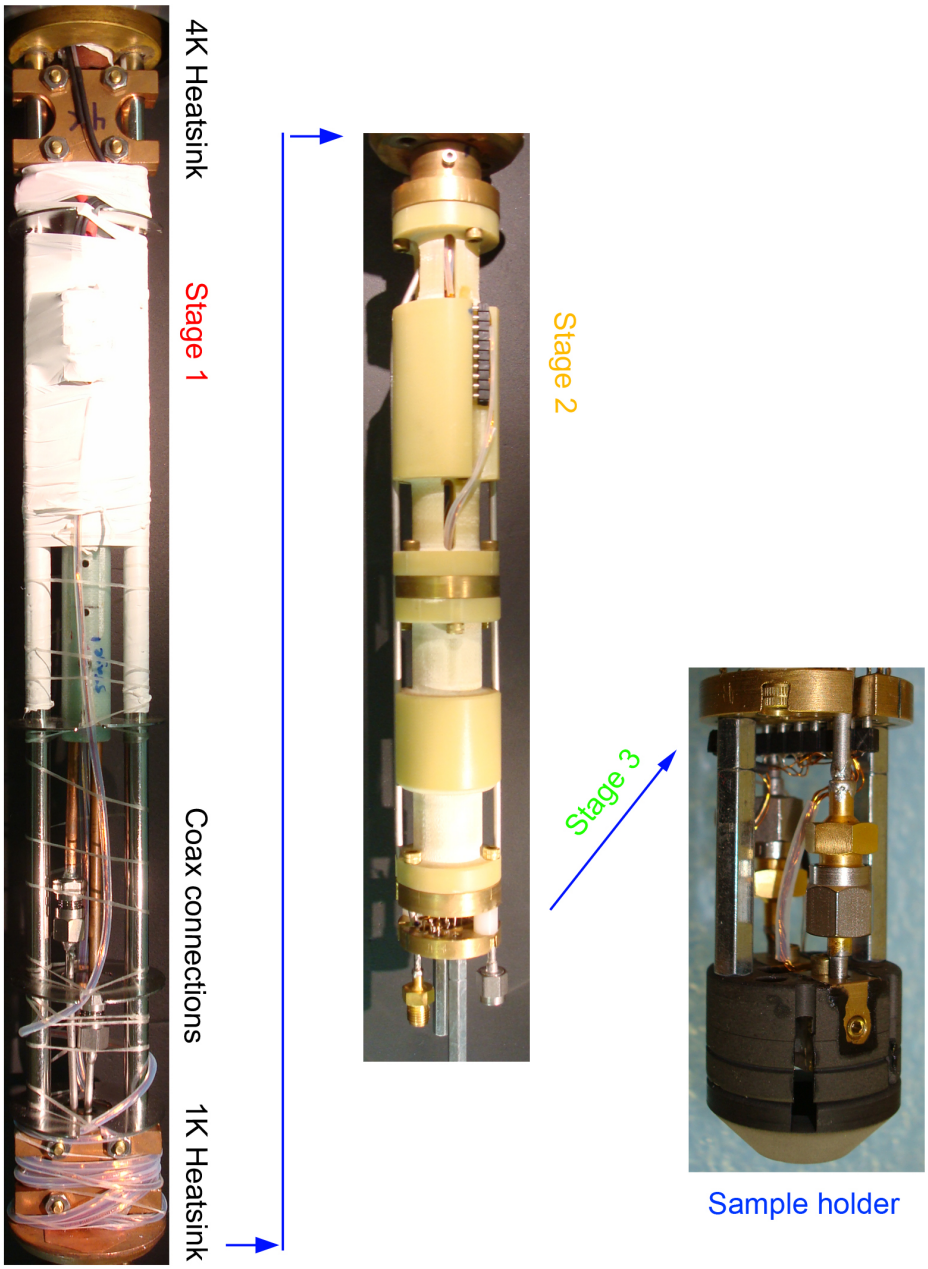

Figure D.1: Pictures of the probe stages: 4K, 1K, and the sample holder.

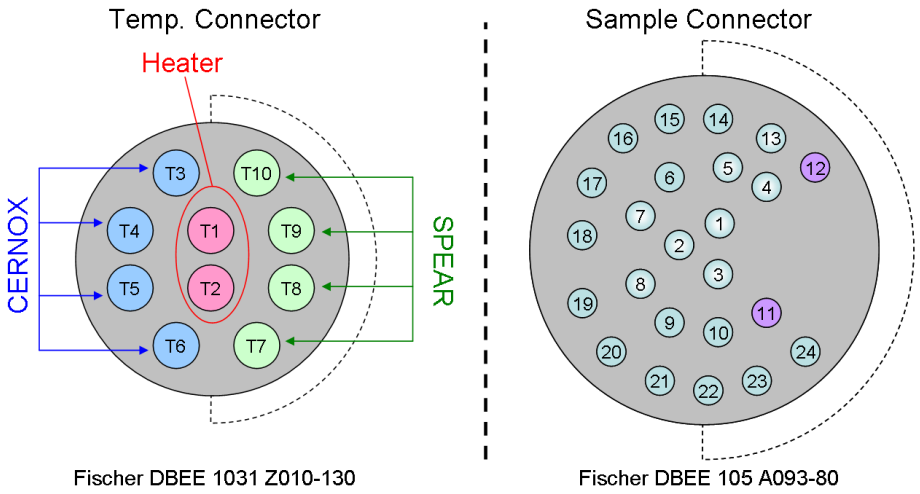

(a) Temperature and Sample hermetic connectors at the top of the probe, as seen from the inside of the probe.

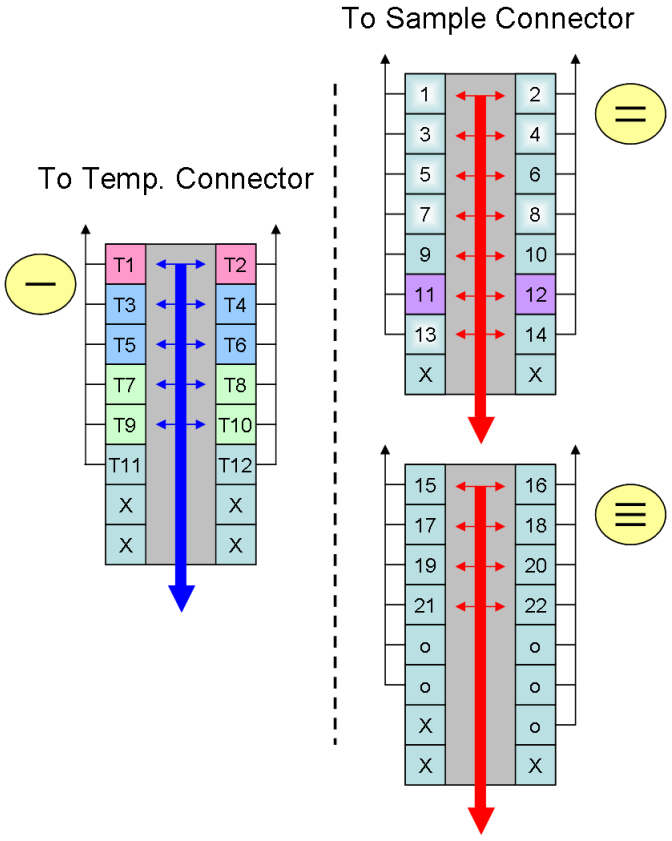

(b) Stage 1 electrical connections, just below the 4K stage.

Figure D.2: Upper levels of electrical connections for the probe.

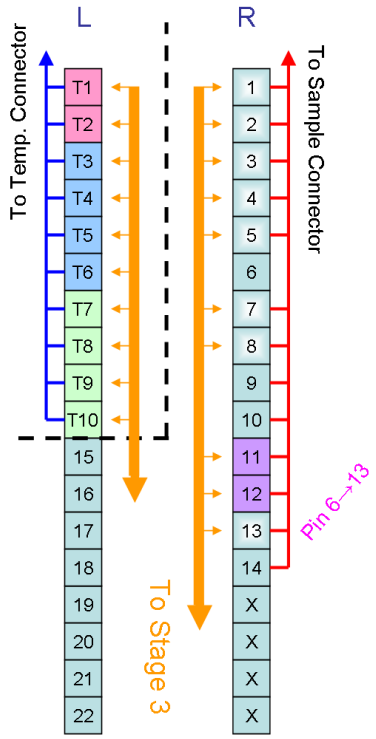

(a) Stage 2 of electrical connections, just below the 1K stage.

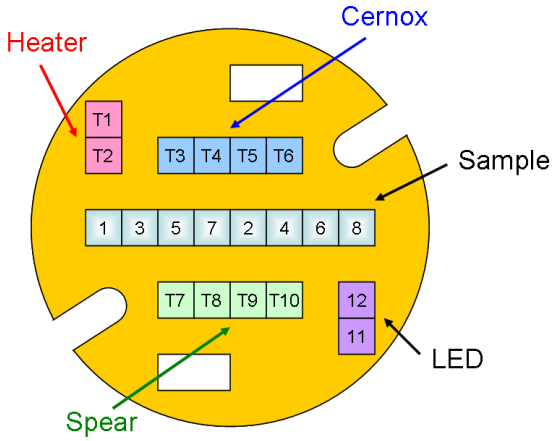

(b) Stage 3, final stage before sample holder, the grooves on the side are to accommodate the coax lines. Slots on top and below are for future electrical connections.

Figure D.3: Electrical diagram for Stage 2 and Stage 3

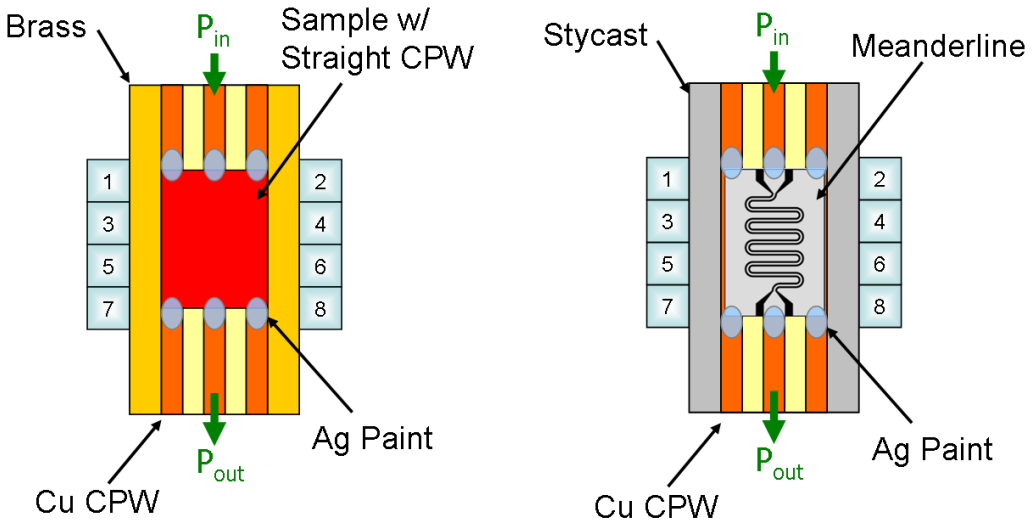

(a) Brass Block

(b) Stycast Block

Figure D.4: Block sample holders. a) Brass block straight CPW, with sample mounted directly in line with the *Cu* CPW. sample also has CPW gate evaporated on top of it. b) Stycast 1266 meanderline CPW, samples would be strapped on top and wired to the contacts.

D.1 Sample Holder/Block Schematic

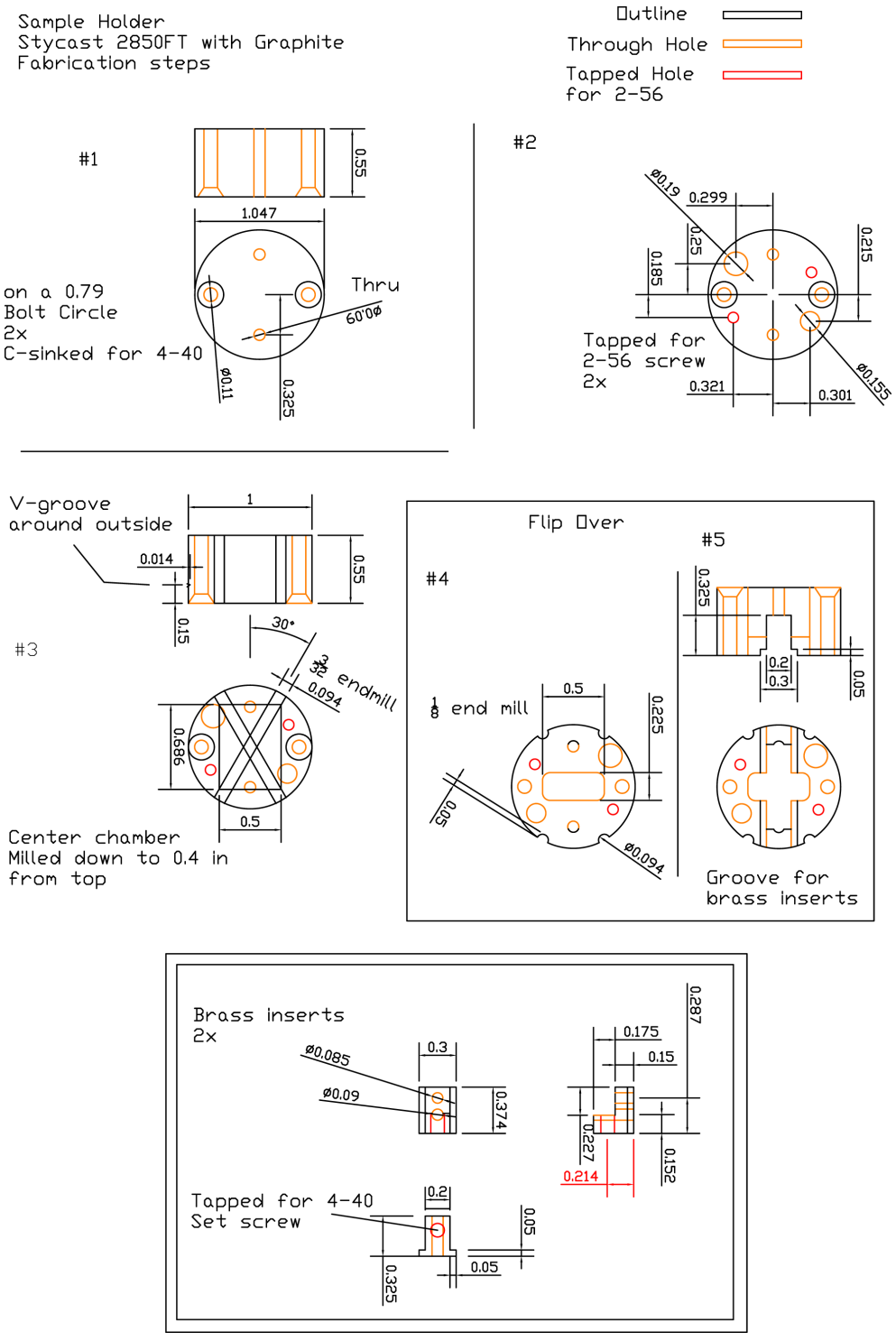

Figure D.5: Stycast 2850FT with graphite sample holder and insert brass inserts. Dimensions in inches.

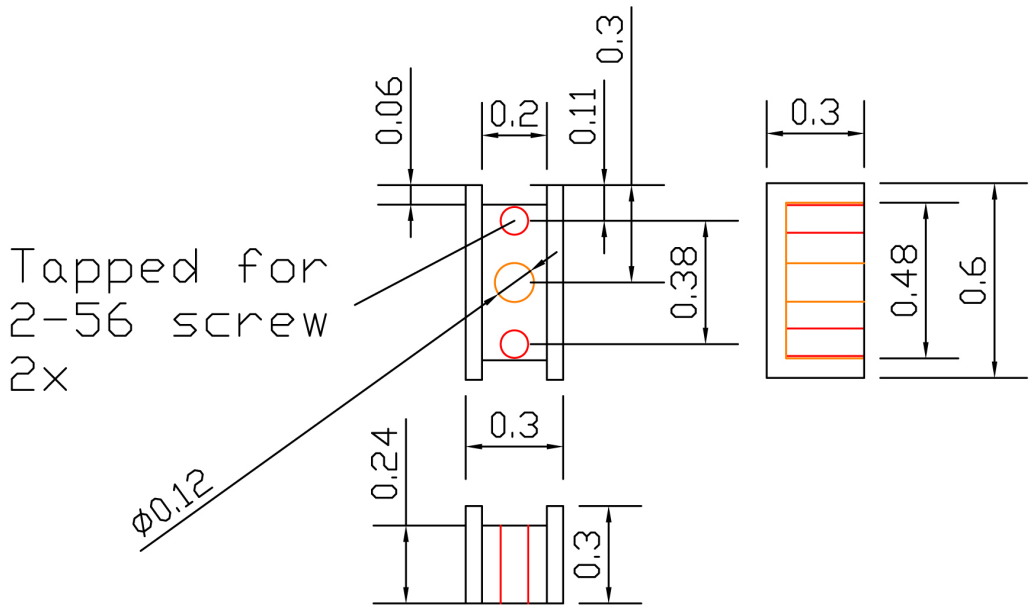

Figure D.6: Block diagram, screw holes/dimensions in inches. The Cu CPW is cut to fit and conductive epoxy is used to mount it into the groove. An endmill is then used to cut a channel perpendicular to the direction of the CPW which is deep enough for the sample/wafer to be mounted into.

D.2 Coaxial Cables

1. Semi-Rigid Coaxial Cable - Micro-coax

   (www.microcoax.com/)

   (a) Low loss cable, UT-120C-LL. From top to of the probe to beyond the 4K heatsink

      i. Inner/Outer conductor: Cu/Cu
      ii. Dielectric: LD PTFE
      iii. Diameter: 3.048 mm (0.120 in)
      iv. Insertion Loss: 1.75 $^{\mathrm{dB}}/_{\mathrm{m}}$ @ 20 GHz
      v. High thermal conduction

(b) Higher loss cable, UT-085B-SS. From the 1K heatsink to the sample.

i. Inner/Outer conductor: 304 Stainless Steel/SP $BeCu$
ii. Dielectric: PTFE
iii. Diameter: 2.197 mm (0.085 in)
iv. Insertion Loss: 6.94 $^{\mathrm{dB}}/_{\mathrm{m}}$ @ 20 GHz
v. Low thermal conduction, more flexible

2. Connectors and Adapters - East Coast Microwaves

(www.ecmstockroom.com/)

(a) Anritsu K Connectors

i. 2.9 mmMale/Female to 3.0 mm - K101M/F
ii. 2.9 mmMale to 2.197 mm - K101M-085

(b) SGMC Microwave 2.9 mm Connectors

i. 2.9 mm Female to 0.085 Semi-Rigid (200-35-10-850)

3. Hermetic Feedthroughs - Astrolab (www.astrolab.com)

(a) 2.9 mm Jack - 2.9 mm Jack Hermetic Adapter: 29485G-4